UNIVERSIDAD NACIONAL AUTÓNOMA DE MÉXICO

PROGRAMA DE MAESTRÍA Y DOCTORADO EN INGENIERÍA
ELÉCTRICA – INSTRUMENTACIÓN

ANALYSIS OF CHANNELED STOKES AND MUELLER MATRIX POLARIMETERS

TESIS
QUE PARA OPTAR POR EL GRADO DE:
MAESTRO EN INGENIERÍA

PRESENTA:
LUIS OSCAR GONZÁLEZ SIU

DIRECTOR DE TESIS:
DR. NEIL CHARLES BRUCE DAVIDSON
INSTITUTO DE CIENCIAS APLICADAS Y TECNOLOGÍA, UNAM

CIUDAD UNIVERSITARIA, CD. MX., MAYO 2021

JURADO ASIGNADO:

Presidente:	Dr. Rodríguez Herrera Oscar G.
Secretario:	Dr. Avendaño Alejo Maximino
Vocal:	Dr. Bruce Davidson Neil Charles
1 er. Suplente:	Dr. García Valenzuela Augusto
2 d o. Suplente:	Dr. Cuevas Cardona Salvador C.

Lugar o lugares donde se realizó la tesis: Instituto de Ciencias Aplicadas y Tecnología, UNAM.

TUTOR DE TESIS:

Dr. Bruce Davidson Neil Charles

FIRMA

Dedico este trabajo a mis padres y a mi hermana, por su apoyo incondicional en mi desarrollo personal y profesional.

Acknowledgements

I thank my advisor, Dr. Neil Bruce, for his support and encouragement during the realization of this research project. I also thank Dr. Oscar Rodríguez, Dr. Maximino Avendaño, Dr. Augusto García, and Dr. Salvador Cuevas for their comments and contributions to improve this thesis.

I acknowledge the *Instituto de Ciencias Aplicadas y Tecnología* and the *Programa de Maestría y Doctorado en Ingeniería de la Universidad Nacional Autónoma de México* for the opportunity and space granted to develop my research project.

I also acknowledge a grant provided under the *Programa Nacional de Posgrados de Calidad* (PNPC) by the *Consejo Nacional de Ciencia y Tecnología* (CONACYT), and the funding of the *Dirección General de Asuntos del Personal Académico* (DGAPA) for the projects IT100417 and IG100121 through the *Programa de Apoyo a Proyectos de Investigación e Innovación Tecnológica*.

Contents

List of Figures

List of Tables

Abstract

In this work the analysis of passive and active polarimeters with spectral channeling, referred to as Stokes and Mueller matrix channeled spectropolarimeters, respectively, is presented. The main advantage of the polarimeters reviewed is their independence on temporal resolution, as they can be used as snapshot polarimeters. The simulation of these polarimeters and some extraction methods for both Stokes vector and Mueller matrix inputs are also presented.

The Stokes Channeled Spectropolarimeter (SCS) setup is composed of two thick birefringent retarders followed by a horizontal linear polarizer. The Mueller matrix Channeled Spectropolarimeter (MMCS) setup is composed of a mirrored SCS as the polarization states generator (PSG) and a SCS as the polarization states analyzer (PSA).

The effects of the retarders thickness ratio and global retardance factor are studied to optimize the channeled spectropolarimeters (CS) setups. Because it is also true that, given these instruments are sensitive to various error sources, a calibration procedure is needed. However, this topic is out of the scope of this thesis. Instead, the sensitivity of the polarimeters to these error sources, including retardance and alignment error, as well as additive Gaussian noise, is discussed.

Introduction

Motivation

When we refer to the polarization of light, we refer to one of the basic properties of a light wave; that is, the polarization is defined to be the description of the vibration of the electric field [1]. Currently, man-made optical detectors do not have a strong enough polarization-dependent response to effectively capture polarization information [2]. For this reason many methods have been developed to determine the polarization of light from observables such as light intensity [3, 4, 5]. These methods comprise the field of polarimetry.

One of the difficulties of polarimetric measurements is the dependence on temporal resolution, but some methods can work around this. Channeled polarimeters with spatial or spectral channeling have independence from temporal resolution through snapshot polarimetry [2, 6].

Spectroscopic analysis of the state of polarization (SOP) of light plays a major role in polarimetric and ellipsometric studies of dispersive materials [7], as cited by Oka [8]. Spectropolarimetry has been widely applied in various application fields, such as remote sensing [9, 10], material characterization [11, 12], and synthesis of novel materials [13, 14], as cited by Ju [15].

Objectives

The main objective of this work is to simulate the extraction process of a source's Stokes vector using channeled spectropolarimetry methods.

The secondary objectives include the simulation of the extraction of the Mueller matrix of an optical component using channeled spectropolarimetry methods, and the study of the effects of multiple error sources (added independently).

Chapter 1

Theory of Polarization

In this chapter, we present some fundamental concepts about polarization, including a simplified deduction of the polarization ellipse, the concepts of Stokes vector and Mueller matrix, and some polarizing elements of interest for this work.

1.1 Polarization

When we refer to the polarization of light, we refer to one of the basic properties of a light wave; that is, the polarization is defined to be the description of the vibration of the electric field [1]. Light, understood as an electromagnetic wave, has no component of electric field in its direction of propagation. Therefore, the field **E** is, exclusively transversal. Furthermore, to completely define the wave, we have to determine the direction of **E** at each moment [16].

Linear polarization is then a vibration along one direction in three-dimensional space with the propagation along a second direction, where the curve traces the location of the tip of the electric field vector as the light propagates through space. Linear polarization is one extreme of a continuum of possible polarizations, called states, where circular polarization is the other extreme. In this case, the plot of the tip of the electric field vector results in a helix. Elliptical polarization is a general term that can be used to describe any state in the continuum from linear to circular [1].

At any instant of time, the locus of points described by the optical field as it propagates is an ellipse. This behaviour is spoken of as optical polarization and is described by Eq. (1.1). The polarization ellipse is inscribed within a rectangle whose sides are parallel to the coordinate axes and their lengths are $2E_{0x}$ and $2E_{0y}$, that is, twice the maximum amplitudes of the correspondent transverse components E_x and E_y when the propagation is in the z direction (see Fig. 1.1) [1]

$$\frac{E_x^2}{E_{0x}^2} + \frac{E_y^2}{E_{0y}^2} - 2\frac{E_x}{E_{0x}}\frac{E_y}{E_{0y}}cos\delta = sin^2\delta \tag{1.1}$$

where δ is the difference between the arbitrary phases δ_x and δ_x, of the transverse components E_x and E_y.

$$\delta = \delta_y - \delta_x \tag{1.2}$$

From Eq. (1.1) and Fig. 1.1, the angle of rotation ψ of the polarization ellipse is given by

$$tan2\psi = \frac{2E_{0x}E_{0y}cos\delta}{E_{0x}^2 - E_{0y}^2} \tag{1.3}$$

We note that, for nonzero values of E_{0x} and E_{0y}, ψ is equal to zero only for phases of $\delta = 90°$ or $270°$. Similarly, for nonzero values of δ, ψ is equal to zero only if E_{0x} or E_{0y} is equal to zero [1].

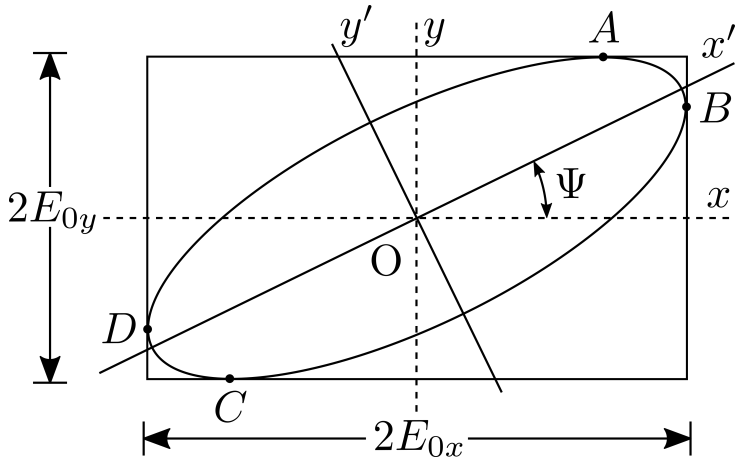

Figure 1.1: Elliptically polarized wave and the polarization ellipse.

Light is classified by its state of polarization (SOP) as:

- Natural light or randomly polarized. When there are two orthogonal components with equal magnitude, but with no correlation between their oscillations (frequency) or phase difference.
- Partially polarized light. When there are two orthogonal components of different magnitude, that is, light has a predominant state of polarization.
- Completely polarized light, which is described by the polarization ellipse (Eq. (1.1)). As mentioned before, polarized light has two specialized (degenerate) forms for certain values of E_{0x}, E_{0y} and δ.
    1. Linear polarized light
    2. Circular polarized light

1.2 The Stokes vector and the Mueller matrix

In 1852, Sir George Gabriel Stokes (1819–1903) discovered that the polarization behaviour could be represented in terms of observables. He found that any state of polarized light could be completely described by four measurable quantities now known as the Stokes polarization parameters. The first parameter expresses the total intensity of the optical field. The remaining three parameters describe the polarization state [1].

In order to represent Eq. (1.1) in terms of the observables of the optical field (Stokes parameters), we must take an average over the time of observation. The time average is represented by the symbol $\langle ... \rangle$, and so we write Eq. (1.1) as [1]

$$\frac{\langle E_x^2(t)\rangle}{E_{0x}^2} + \frac{\langle E_y^2(t)\rangle}{E_{0y}^2} - 2\frac{\langle E_x(t)\rangle}{E_{0x}}\frac{\langle E_y(t)\rangle}{E_{0y}} cos\delta = sin^2\delta \tag{1.4}$$

Solving the average values and substituting them into Eq. (1.4) yields

$$S_0 = E_{0x}^2 + E_{0y}^2 \tag{1.5}$$
$$S_1 = E_{0x}^2 - E_{0y}^2 \tag{1.6}$$
$$S_2 = 2E_{0x}E_{0y}cos\delta \tag{1.7}$$
$$S_3 = 2E_{0x}E_{0y}sin\delta \tag{1.8}$$

where the first Stokes parameter S_0 is the total intensity of the light. The parameter S_1 describes the amount of linear horizontal or vertical polarization, the parameter S_2 describes the amount of linear $+45^\circ$ or -45° polarization, and the parameter S_3 describes the amount of right or left circular polarization contained within the beam. We note that the four Stokes parameters are expressed in terms of intensities, and we again emphasize that the Stokes parameters are real quantities [1].

The Stokes parameters are arranged in a column vector known as the Stokes vector. This step, while simple, provides a formal method for treating numerous complicated problems involving polarized light using well established linear algebra techniques [1].

$$\underline{\mathbf{S}} = (S_0, S_1, S_2, S_3)^T \tag{1.9}$$

If we now have partially polarized light, one can show that for any state of polarized light the Stokes parameters always satisfy the relation

$$S_0^2 \geqslant S_1^2 + S_2^2 + S_3^2 \tag{1.10}$$

This is an equality when we have completely polarized light, and an inequality when we have partially polarized light or unpolarized light. Therefore, the Stokes vector is a mathematical tool for representing the state of polarization of a field [1].

When an optical beam interacts with matter, its polarization state is almost always changed, as expressed by Eq. (1.11). In fact, this appears to be the rule rather than the exception. The polarization state can be changed by (1) changing the amplitudes of the components of the light (diattenuation), (2) changing the relative phase between orthogonal components (retardance), (3) changing the direction of the orthogonal field components (rotation), or (4) transferring energy from polarized states to the unpolarized state (depolarization). These fundamental properties of a polarization element are encoded within the Mueller matrix $\underline{\underline{\mathbf{M}}}$, see Eq. (1.12); although, rotation essentially results in a coordinate transformation. The Mueller matrix is a very powerful mathematical tool for treating the interaction of light with matter [1].

$$\underline{\mathbf{S}}_{i+1} = \underline{\underline{\mathbf{M}}}\,\underline{\mathbf{S}}_i \tag{1.11}$$

$$\underline{\underline{\mathbf{M}}} = \begin{pmatrix} m_{00} & m_{01} & m_{02} & m_{03} \\ m_{10} & m_{11} & m_{12} & m_{13} \\ m_{20} & m_{21} & m_{22} & m_{23} \\ m_{30} & m_{31} & m_{32} & m_{33} \end{pmatrix} \tag{1.12}$$

An optical element that changes the orthogonal amplitudes unequally is called a polarizer or, more correctly, a diattenuator. Similarly, an optical device that introduces a phase shift between the orthogonal components is called a retarder; other names used for the same device are wave plate, compensator, or phase shifter. If the optical device rotates the orthogonal components of the beam through an angle θ as it propagates through the element, it is called a rotator. Finally, if energy in polarized states goes to unpolarized states, the element is a depolarizer [1].

1.3 Polarizing elements

A diattenuator (polarizer) is an optical element that attenuates the orthogonal components of an optical beam unequally; that is, a diattenuator is an anisotropic attenuator; the two orthogonal transmission axes are designated p_x and p_y. This element is commonly known as a polarizer; the more recent, accurate, and descriptive term is diattenuator. Because of its historical and embedded use, we will make concessions to convention, and make free use of the term polarizer. For this work, we considered rotated ideal linear horizontal polarizers ($p_x = 1$ and $p_y = 0$), Eq. (1.13) presents the corresponding Mueller matrix [1].

$$\underline{\underline{\mathbf{M}}}_P(2\theta) = \frac{1}{2}\begin{pmatrix} 1 & cos\,2\theta & sin\,2\theta & 0 \\ cos\,2\theta & cos^2\,2\theta & sin2\theta cos2\theta & 0 \\ sin\,2\theta & sin2\theta cos2\theta & sin^2\,2\theta & 0 \\ 0 & 0 & 0 & 0 \end{pmatrix} \tag{1.13}$$

where θ is the rotation angle of the polarizer with respect to the horizontal reference.

A retarder is a polarizing element that changes the phase of the optical beam. Strictly speaking, its correct name is phase shifter. However, historical usage has led to the alternative names retarder, wave plate, and compensator. Retarders introduce a phase shift of ϕ between the orthogonal components of the incident field. The Mueller matrix of a rotated retarder is given by [1]

$$\underline{\underline{\mathbf{M}}}_R(\phi, 2\theta) = \begin{pmatrix} 1 & 0 & 0 & 0 \\ 0 & cos^2 2\theta + cos\phi sin^2 2\theta & (1 - cos\phi) sin2\theta cos2\theta & -sin\phi sin2\theta \\ 0 & (1 - cos\phi) sin2\theta cos2\theta & sin^2 2\theta + cos\phi cos^2 2\theta & sin\phi cos2\theta \\ 0 & sin\phi sin2\theta & -sin\phi cos2\theta & cos\phi \end{pmatrix} \tag{1.14}$$

where θ is the rotation angle of the retarder with respect to the horizontal reference.

1.4 Channeled polarimetry

The science of measuring polarization is known as polarimetry. We can measure the Stokes parameters; that is, determine the polarization state of light, and we can measure the Mueller matrix, that is, the characteristics of polarizing elements. Both techniques can be partial or complete, if we can measure all the Stokes parameters or the entire Mueller matrix [1].

There are also "null" techniques where the observer's eye is the detection device and which rely on the determination of the absence of light. Nevertheless, we will focus on automated polarimetry techniques with the assumption that measurements are to be done using modern detectors, electronics, and computer automation available to today's experimental researcher [1].

Temporal misregistration, or intensity differences between time-sequential measurements not induced by polarization, can be a significant source of error in certain applications. Such misregistration can be caused by motion of the platform or scene, and is therefore a particular concern in the field of remote sensing [17], as cited by Goldstein [1].

If temporal scanning (e.g., a rotating retarder polarimeter) is used to measure the Stokes parameters of a changing scene, then motion-based misregistration can occur between the measurements. Consequently, both polarimetric and motion-based intensity differences will appear as a signal after data reduction. An example of a motion-induced artifact from a rotating retarder polarimeter can be a moving sailboat; creating the appearance of multiple targets [1].

One method that avoids temporal misregistration is referred to as channeled polarimetry (CP). CP techniques make use of polarization interference in order to amplitude modulate the Stokes parameters onto either spectral or spatial carrier frequencies. The use of interference can be beneficial in several respects when compared to a conventional polarimeter. For instance, in a conventional polarimeter, four intensity measurements must be taken (e.g., I_0, I_{90}, I_{135}, and I_R) for the calculation of a complete Stokes vector. Doing so requires these values be manipulated (added and subtracted from one another) within a computer during post processing. Conversely, CP enables the direct measurement of all four Stokes parameters simultaneously, by performing the addition and subtraction optically, through interference between four coherent beams [1]. That is, CP enables snapshot polarimetry [6].

This is feasible because interference maintains the phase of each component within the complex amplitude, before the detector measures the intensity. Consequently, the amplitude and phase of the Stokes parameters are encoded within the amplitude and phase of the carrier frequency, enabling the magnitude and sign (or handedness) of the Stokes parameters to be extracted [1].

Another benefit of CP is realized through spectral or spatial registration. In a conventional polarimeter, image registration between the intensity measurements must be accomplished to within 1/20th of a pixel to achieve an accurate Stokes parameter reconstruction [18], as cited by Goldstein [1]. Otherwise, false polarization signatures can occur in the spectrum or scene. Again, CP resolves these concerns by its use of interference. Since a given Stokes parameter is calculated interferometrically and measured directly, image registration between several intensity measurements is unnecessary. Furthermore, since each Stokes parameter is modulated on coincident carrier frequencies, spatial or spectral registration between all the Stokes parameters is inherent. This significantly reduces the complexity of the Stokes vector calculation over conventional polarimeters. However, these benefits come at a tradeoff, typically to the spatial and spectral resolution of the sensor [1].

The fundamental concept of CP can be considered an analog to conventional amplitude modulation (AM) [19], as cited by Goldstein [1]. In AM, a time-dependent signal is mixed with a high frequency carrier U given by

$$I(t) = A + D(t)\,cos(2\pi Ut + \phi) \tag{1.15}$$

It should be noted that such a cosinusoidally modulated spectrum is generally called a channelled spectrum and is frequently used in the field of frequency-domain interferometry [8]. Each of the these harmonic modulations will split the information in the corresponding Fourier domains, creating weighted copies of the Fourier transform of the data at the modulations carrier frequencies. These multiplexed copies are called channels [6].

Chapter 2

Channeled Spectropolarimetry

In this chapter, the fundamental concepts of channeled spectropolarimetry (CS) are introduced. The CS setup of interest is also described for a Stokes channeled spectropolarimeter (SCS) and a Mueller matrix channeled spectropolarimeter (MMCS), including the parameter extraction techniques.

2.1 SCS Setup

Channeled spectropolarimetry (CS) is often implemented with a spectrometer that uses some form of dispersion, such as a diffraction grating or prism [1]. Furthermore, the spectrometer must have sufficient wavenumber resolution $\Delta\sigma$ to acquire the fine structure of the channelled spectrum. This implies that smaller wavelength resolution $\Delta\lambda$ is needed for shorter wavelength λ [8].

The CS configuration of interest is capable of measuring the complete Stokes vector and was proposed by Oka and Kato [8], see Fig. 2.1. The CS consists of two thick birefringent retarders, R_1 and R_2, with fast axes orientations at 0° and 45°, respectively; following comes an analyzer, with its transmission axis defining the 0° reference, and the dispersive spectrometer. Equations (2.1), (2.2), and (2.3) show the Mueller matrices for the polarizer and the two retarders at 0° and 45°, respectively.

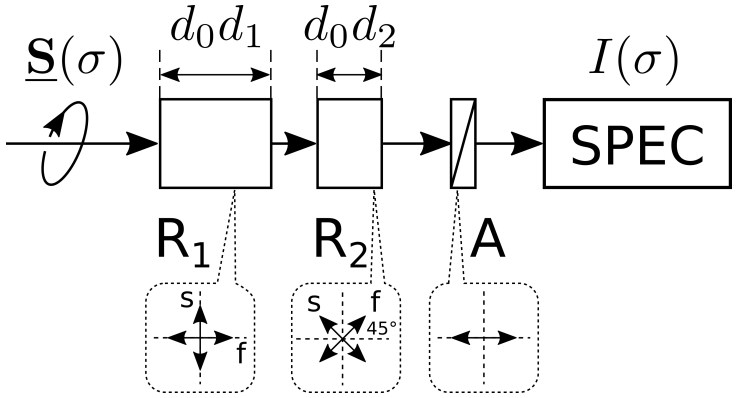

Figure 2.1: Stokes channeled spectropolarimeter setup.

The Mueller matrices of these components are

$$\underline{\underline{\mathbf{M}}}_P(2(0^\circ)) = \frac{1}{2}\begin{pmatrix} 1 & 1 & 0 & 0 \\ 1 & 1 & 0 & 0 \\ 0 & 0 & 0 & 0 \\ 0 & 0 & 0 & 0 \end{pmatrix} \tag{2.1}$$

$$\underline{\underline{\mathbf{M}}}_{R1}(\phi_1, 2(0^\circ)) = \begin{pmatrix} 1 & 0 & 0 & 0 \\ 0 & 1 & 0 & 0 \\ 0 & 0 & cos\phi_1 & sin\phi_1 \\ 0 & 0 & -sin\phi_1 & cos\phi_1 \end{pmatrix} \tag{2.2}$$

$$\underline{\underline{\mathbf{M}}}_{R2}(\phi_2, 2(45^\circ)) = \begin{pmatrix} 1 & 0 & 0 & 0 \\ 0 & cos\phi_2 & 0 & -sin\phi_2 \\ 0 & 0 & 1 & 0 \\ 0 & sin\phi_2 & 0 & cos\phi_2 \end{pmatrix} \tag{2.3}$$

The retardance ϕ_i of the birefringent plate is given by Eq. (2.7)

$$\phi_i = \frac{2\pi}{\lambda}\tau_i \tag{2.4}$$

$$= 2\pi\sigma\tau_i \tag{2.5}$$

$$\tau_i = d_0 d_i B \tag{2.6}$$

$$\phi_i = 2\pi\sigma d_0 d_i B \tag{2.7}$$

where $(2\pi\sigma\tau_i)$ signify that retardances are linear with wavenumber [2], d_0 and d_i are the global and local retardance factors, respectively of the i-th retarder. The product $d_0 d_i$ is the retarder's thickness. The concept of the present method is based primarily on the fact that the phase retardation of a thick birefringent plate changes appreciably with wave number σ. This implies that the birefringent plate can serve as a variable retarder when it is combined with a spectroscopic device [8]. Although, Eq. (2.7) is a function of σ, this dependence will not be written explicitly in the rest of this work to simplify the further developments.

From Fig. 2.1 and Eq. (2.1), (2.2), and (2.3), the matrix for the SCS is given by

$$\underline{\underline{\mathbf{W}}} = \underline{\underline{\mathbf{M}}}_P(0)\underline{\underline{\mathbf{M}}}_{R2}(\phi_2, \pi/2)\underline{\underline{\mathbf{M}}}_{R1}(\phi_1, 0) \tag{2.8}$$

Considering a light source of unknown SOP $\underline{\mathbf{S}}(\sigma)$ and a detector insensitive to polarization, the measured irradiance is given by

$$I(\sigma) = \begin{pmatrix} 1 & 0 & 0 & 0 \end{pmatrix} \underline{\underline{\mathbf{W}}}\, \underline{\mathbf{S}}(\sigma) \tag{2.9}$$

Substituting the corresponding matrices

$$I(\sigma) = \begin{pmatrix}1 & 0 & 0 & 0\end{pmatrix} \underline{\underline{\mathbf{M}}}_P(0)\underline{\underline{\mathbf{M}}}_{R2}(\phi_2, \pi/2)\underline{\underline{\mathbf{M}}}_{R1}(\phi_1, 0)\underline{\mathbf{S}}(\sigma) \tag{2.10}$$

$$\begin{aligned} I(\sigma) =& \frac{1}{2}\begin{pmatrix}1\\0\\0\\0\end{pmatrix}^T \begin{pmatrix}1 & 1 & 0 & 0\\1 & 1 & 0 & 0\\0 & 0 & 0 & 0\\0 & 0 & 0 & 0\end{pmatrix}\begin{pmatrix}1 & 0 & 0 & 0\\0 & cos\phi_2 & 0 & -sin\phi_2\\0 & 0 & 1 & 0\\0 & sin\phi_2 & 0 & cos\phi_2\end{pmatrix}\times \\ & \times \begin{pmatrix}1 & 0 & 0 & 0\\0 & 1 & 0 & 0\\0 & 0 & cos\phi_1 & sin\phi_1\\0 & 0 & -sin\phi_1 & cos\phi_1\end{pmatrix}\begin{pmatrix}S_0(\sigma)\\S_1(\sigma)\\S_2(\sigma)\\S_3(\sigma)\end{pmatrix} \end{aligned} \tag{2.11}$$

$$I(\sigma) = \frac{1}{2}\begin{pmatrix}1\\0\\0\\0\end{pmatrix}^T \begin{pmatrix}1 & cos\phi_2 & sin\phi_1 sin\phi_2 & -cos\phi_1 sin\phi_2\\1 & cos\phi_2 & sin\phi_1 sin\phi_2 & -cos\phi_1 sin\phi_2\\0 & 0 & 0 & 0\\0 & 0 & 0 & 0\end{pmatrix}\begin{pmatrix}S_0(\sigma)\\S_1(\sigma)\\S_2(\sigma)\\S_3(\sigma)\end{pmatrix} \tag{2.12}$$

This product defines the intensity profile $I(\sigma)$ as a sum of sines and cosines with arguments that are the combinations of different modulations from the system. The intensity spectrum recorded by the detector is given by

$$I(\sigma) = \frac{1}{2}S_0(\sigma) + \frac{1}{2}S_1(\sigma)cos\phi_2 + \frac{1}{2}S_2(\sigma)sin\phi_1 sin\phi_2 - \frac{1}{2}S_3(\sigma)cos\phi_1 sin\phi_2 \tag{2.13}$$

From Eq. (2.7) and (2.13), the effective carrier frequencies of the recorded spectrum are $U_i = d_0 d_i B$. Therefore, the carrier frequencies increase with both the thickness and the birefringence of the retarders [1]. Furthermore, we consider that the polarizer behaves the same independently of wavenumber and the retarders' behaviour depends on wavenumber.

From the trigonometric identities

$$cos(a \pm b) = cos(a)cos(b) \mp sin(a)sin(b) \tag{2.14}$$

$$sin(a \pm b) = sin(a)cos(b) \pm cos(a)sin(b) \tag{2.15}$$

we have

$$sin(a)sin(b) = \frac{1}{2}(-cos(a+b) + cos(a-b)) \tag{2.16}$$

$$cos(a)sin(b) = \frac{1}{2}(sin(a+b) - sin(a-b)) \tag{2.17}$$

Substituting in Eq. (2.13)

$$\begin{aligned} I(\sigma) =& \frac{1}{2}S_0(\sigma) + \frac{1}{2}S_1(\sigma)cos\phi_2 \\ &+ \frac{1}{4}S_2(\sigma)[-cos(\phi_1+\phi_2) + cos(\phi_1-\phi_2)] \\ &- \frac{1}{4}S_3(\sigma)[sin(\phi_1+\phi_2) - sin(\phi_1-\phi_2)] \end{aligned} \tag{2.18}$$

The inverse Fourier transform of $I(\sigma)$ gives the autocorrelation function $C(\tau)$ [8], see Eq. (2.22), which describes the modulation channels in the τ-domain (optical path difference, OPD-space) of the spectrum of the SOP we want to know. The Fourier transforms of the three modulations are

$$1(\sigma) \longleftrightarrow \delta(\tau) \tag{2.19}$$

$$cos(2\pi\sigma\tau_i) \longleftrightarrow \frac{1}{2}[\delta(\tau+\tau_i) + \delta(\tau-\tau_i)] \tag{2.20}$$

$$sin(2\pi\sigma\tau_i) \longleftrightarrow \frac{\jmath}{2}[\delta(\tau+\tau_i) - \delta(\tau-\tau_i)] \tag{2.21}$$

where δ, with no subscript, is the Dirac delta function, τ is the Fourier transform variable of σ [1, 2, 6].

$$C(\tau) = \mathcal{F}^{-1}\{I(\sigma)\} \tag{2.22}$$

$$\begin{aligned} =& \frac{1}{2}\mathcal{F}^{-1}\{S_0(\sigma)\} + \frac{1}{4}\mathcal{F}^{-1}\{S_1(\sigma)\} * [\delta(\tau+\tau_2) + \delta(\tau-\tau_2)] \\ &+ \frac{1}{8}\mathcal{F}^{-1}\{S_2(\sigma)\} * [-\delta(\tau+\tau_1+\tau_2) - \delta(\tau-\tau_1-\tau_2) \\ &\quad + \delta(\tau+\tau_1-\tau_2) + \delta(\tau-\tau_1+\tau_2)] \\ &- \jmath\frac{1}{8}\mathcal{F}^{-1}\{S_3(\sigma)\} * [\delta(\tau+\tau_1+\tau_2) - \delta(\tau-\tau_1-\tau_2) \\ &\quad - \delta(\tau+\tau_1-\tau_2) + \delta(\tau-\tau_1+\tau_2)] \end{aligned} \tag{2.23}$$

Each successive modulation in the σ-domain is equivalent to a convolution of those δ-functions in the τ-domain, which all have potentially different OPD τ_i [2]. This is observed in Eq. (2.23). Therefore, the channels, $H(\tau-\tau_i)$, can be isolated using a frequency filtering technique [15].

We observe that the autocorrelation function (Eq. (2.23)) considers six possible modulations (additional channels to the central channel C_0) centred in positions given by

$$\tau = 0, \pm\tau_2, \pm(\tau_1-\tau_2), \pm(\tau_1+\tau_2) \tag{2.24}$$

Although, we do not expect modulations at $\tau = \pm\tau_1$, we consider it as a reference. Therefore, the autocorrelation function has nine modulation channels in total for our approach to the SCS method.

From Eq. (2.7), retardance is a function of the retarder's thickness and the field's wavenumber that passes through the retarder. Nevertheless, as both retarders are made of the same material and are exposed to the same spectrum range, it is considered that the retardances are mainly dependent on the thicknesses (d_0d_1, d_0d_2). Therefore, we propose a classification of the SCS of interest based on the thickness' ratio ($d_1 : d_2$) for retarders R_1 y R_2 (see Table 2.1).

For certain thickness' ratios, the number of channels is decreased by means of crosstalk, that is, two or more channels overlap to some extent where they are not distinguishable. The level of reduction of channels is greater for the Mueller matrix polarimeter which uses four retarders, compared with the Stokes polarimeter.

When $\phi_1 \neq \phi_2$, we expect six different cases with up to nine channels ($N_C = 9$), see Table 2.1. It is also noticed that for $\phi_1 = 2\phi_2$ and $\phi_1 = \phi_2/2$, channel $H(\tau \mp (\tau_1 - \tau_2))$ is combined (crosstalk) with channel $H(\tau \mp \tau_2)$ and $H(\tau \pm \tau_1)$, respectively. For these cases, the number of channels (N_C) is reduced to seven.

Table 2.1: Thickness ratio ($d_1 : d_2$) classification of SCS

Case			Channel relative position				
	d_1	$(d_1 : d_2)$	τ_1	τ_2	$\tau_1 + \tau_2$	$\tau_1 - \tau_2$	N_C
1	$< d_2/2$	(1, 3)	1	3	4	-2	9
2	$= d_2/2$	(1, 2)	1	2	3	-1	7
3	$> d_2/2$	(1, 1.5)	2	3	4	-1	9
4	$> 2d_2$	(3, 1)	3	1	4	2	9
5	$= 2d_2$	(2, 1)	2	1	3	1	7
6	$< 2d_2$	(1.5, 1)	3	2	4	1	9

To extract the Stokes vector, three methods were considered: 1) Mueller analysis, 2) Channel Splitting as described by Oka and Kato [8], and 3) Analytical Channel Splitting as described by Alenin and Tyo [2, 6]. For the last two cases, we calculate the autocorrelation function and we try to recover the SOP.

2.1.1 Mueller analysis

Supposing we know the real Mueller matrix $\underline{\underline{\mathbf{W}}}$ of the SCS (Eq. (2.8)) along the wavenumber range, we can solve the Stokes vector $\underline{\mathbf{S}}(\sigma)$ with the irradiance measured by the spectrometer (Eq. (2.9)).

$$\begin{aligned}
\underline{\mathbf{I}} =& I(\sigma) && (2.25)\\
=& \begin{pmatrix}1 & 0 & 0 & 0\end{pmatrix} \underline{\underline{\mathbf{W}}}(\sigma)\, \underline{\mathbf{S}}(\sigma) && (2.26)\\
=& \begin{pmatrix}w_{00}(\sigma) & w_{01}(\sigma) & w_{02}(\sigma) & w_{03}(\sigma)\end{pmatrix} \underline{\mathbf{S}}(\sigma) && (2.27)\\
\underline{\mathbf{S}}(\sigma) =& \begin{pmatrix}w_{00}(\sigma) & w_{01}(\sigma) & w_{02}(\sigma) & w_{03}(\sigma)\end{pmatrix}^{-1} \underline{\mathbf{I}} && (2.28)
\end{aligned}$$

We have to solve this for each σ_n where $(n = 0, 1, 2, \ldots, N-1)$

$$\underline{\mathbf{S}}(\sigma_n) = \begin{pmatrix}w_{00}(\sigma_n) & w_{01}(\sigma_n) & w_{02}(\sigma_n) & w_{03}(\sigma_n)\end{pmatrix}^{-1} I(\sigma_n) \tag{2.29}$$

or

$$\underline{\mathbf{S}}(\sigma) = \underline{\underline{\mathbf{W}'}}^{+} \underline{\mathbf{I}} \tag{2.30}$$

where

$$\underline{\underline{\mathbf{W}'}} = \begin{pmatrix} w_{00}(\sigma_1) & w_{01}(\sigma_1) & w_{02}(\sigma_1) & w_{03}(\sigma_1) \\ w_{00}(\sigma_2) & w_{01}(\sigma_2) & w_{02}(\sigma_2) & w_{03}(\sigma_2) \\ \vdots & \vdots & \vdots & \vdots \\ w_{00}(\sigma_N) & w_{01}(\sigma_N) & w_{02}(\sigma_N) & w_{03}(\sigma_N) \end{pmatrix} \tag{2.31}$$

and $\underline{\underline{\mathbf{W}'}}^{+}$ is the pseudo-inverse, given by the Moore-Penrose generalized inverse

$$\underline{\underline{\mathbf{W}'}}^{+} = (\underline{\underline{\mathbf{W}'}}^{T} \underline{\underline{\mathbf{W}'}})^{-1} \underline{\underline{\mathbf{W}'}}^{T} \tag{2.32}$$

Nevertheless, this method considers $\underline{\mathbf{S}}(\sigma)$ to be invariant with wavenumber. Therefore it is only used as a control method.

2.1.2 Channel Splitting

From the autocorrelation function (Eq. (2.23)), each channel is isolated using a window filter and applying Fourier analysis we can solve the Stokes parameters [8]. The filters applied can be fitted to specific configurations or designed to benefit the filtering of certain channels of interest.

From Eq. (2.18), using the Euler identities

$$\begin{aligned} I(\sigma) =& \frac{1}{2}S_0(\sigma) + \frac{1}{4}S_1(\sigma)(e^{+\jmath\phi_2} + e^{-\jmath\phi_2}) \\ & - \frac{1}{8}S_2(\sigma)(e^{+\jmath(\phi_1+\phi_2)} + e^{-\jmath(\phi_1+\phi_2)}) + \frac{1}{8}S_2(\sigma)(e^{+\jmath(\phi_1-\phi_2)} + e^{-\jmath(\phi_1-\phi_2)}) \\ & - \jmath\frac{1}{8}S_3(\sigma)(e^{+\jmath(\phi_1+\phi_2)} - e^{-\jmath(\phi_1+\phi_2)}) + \jmath\frac{1}{8}S_3(\sigma)(e^{+\jmath(\phi_1-\phi_2)} - e^{-\jmath(\phi_1-\phi_2)}) \end{aligned} \tag{2.33}$$

We rewrite the autocorrelation function (Eq. (2.23)) as

$$\begin{aligned} C(\tau) =& \frac{1}{2}A_0(\tau) + \frac{1}{4}A_1(\tau-\tau_2) + \frac{1}{4}A_1^*(\tau+\tau_2) \\ & + \frac{1}{8}A_2(\tau-(\tau_1-\tau_2)) + \frac{1}{8}A_2^*(\tau+(\tau_1-\tau_2)) \\ & - \frac{1}{8}A_3(\tau-(\tau_1+\tau_2)) - \frac{1}{8}A_3^*(\tau+(\tau_1+\tau_2)) \end{aligned} \tag{2.34}$$

where

$$A_0(\tau) = \mathcal{F}^{-1}\{S_0(\sigma)\} \tag{2.35}$$

$$A_1(\tau-\tau_2) = \mathcal{F}^{-1}\{S_1(\sigma)e^{-\jmath\phi_2}\} \tag{2.36}$$

$$A_2(\tau-(\tau_1-\tau_2)) = \mathcal{F}^{-1}\{S_{23}(\sigma)e^{-\jmath(\phi_1-\phi_2)}\} \tag{2.37}$$

$$A_3(\tau-(\tau_1+\tau_2)) = \mathcal{F}^{-1}\{S_{23}(\sigma)e^{-\jmath(\phi_1+\phi_2)}\} \tag{2.38}$$

$$S_{23}(\sigma) = S_2(\sigma) - \jmath S_3(\sigma) \tag{2.39}$$

The Stokes parameters are obtained using Fourier analysis and the Channel Splitting method [2, 6, 8].

$$S_0(\sigma) = \mathcal{F}\{A_0(\tau)\} \tag{2.40}$$

$$S_1(\sigma) = \mathcal{F}\{A_1(\tau-\tau_2)\}e^{+\jmath\phi_2} \tag{2.41}$$

$$S_{23}(\sigma) = \mathcal{F}\{A_3(\tau-(\tau_1+\tau_2))\}e^{+\jmath(\phi_1+\phi_2)} \tag{2.42}$$

$$S_2(\sigma) = Re\{S_{23}\} \tag{2.43}$$

$$S_3(\sigma) = Im\{S_{23}\} \tag{2.44}$$

We ignore channel $A_2(\tau-(\tau_1-\tau_2))$ because of the crosstalk between channels $H(\tau-(\tau_1-\tau_2))$ and $H(\tau-\tau_2)$, when $\phi_1=2\phi_2$. For this case, a correction is needed. From Eq. (2.33)

$$\begin{aligned}I(\sigma)=&\frac{1}{2}S_0(\sigma)+\frac{1}{4}S_1(\sigma)(e^{+\jmath\phi_2}+e^{-\jmath\phi_2})\\&-\frac{1}{8}S_2(\sigma)(e^{+\jmath(\phi_1+\phi_2)}+e^{-\jmath(\phi_1+\phi_2)})+\frac{1}{8}S_2(\sigma)(e^{+\jmath(\phi_2)}+e^{-\jmath(\phi_2)})\\&-\jmath\frac{1}{8}S_3(\sigma)(e^{+\jmath(\phi_1+\phi_2)}-e^{-\jmath(\phi_1+\phi_2)})+\jmath\frac{1}{8}S_3(\sigma)(e^{+\jmath(\phi_2)}-e^{-\jmath(\phi_2)})\end{aligned}\tag{2.45}$$

$$\begin{aligned}=&\frac{1}{2}S_0(\sigma)+\frac{1}{4}\Big(S_1(\sigma)+\frac{1}{2}S_{23}(\sigma)\Big)e^{-\jmath\phi_2}+\frac{1}{4}\Big(S_1(\sigma)+\frac{1}{2}S_{23}^*(\sigma)\Big)e^{+\jmath\phi_2}\\&-\frac{1}{8}S_{23}(\sigma)e^{-\jmath(\phi_1+\phi_2)}-\frac{1}{8}S_{23}^*(\sigma)e^{+\jmath(\phi_1+\phi_2)}\end{aligned}\tag{2.46}$$

The autocorrelation function is given by

$$\begin{aligned}C(\tau)=&\frac{1}{2}\mathcal{F}^{-1}\{S_0(\sigma)\}\\&+\frac{1}{4}\mathcal{F}^{-1}\{\Big(S_1(\sigma)+\frac{1}{2}S_{23}(\sigma)\Big)e^{-\jmath\phi_2}\}+\frac{1}{4}\mathcal{F}^{-1}\{\Big(S_1(\sigma)+\frac{1}{2}S_{23}^*(\sigma)\Big)e^{+\jmath\phi_2}\}\\&-\frac{1}{8}\mathcal{F}^{-1}\{S_{23}(\sigma)e^{-\jmath(\phi_1+\phi_2)}\}-\frac{1}{8}\mathcal{F}^{-1}\{S_{23}^*(\sigma)e^{+\jmath(\phi_1+\phi_2)}\}\end{aligned}\tag{2.47}$$

The Stokes parameters S_0, S_2, and S_3 are still solved using Eq. (2.40), (2.43), and (2.44). But the channels with information of S_1 and S_2 have crosstalk, as stated by Eq. (2.48).

$$A_1(\tau-\tau_2)=\mathcal{F}^{-1}\{\Big(S_1(\sigma)+\frac{1}{2}S_{23}(\sigma)\Big)e^{-\jmath\phi_2}\}\tag{2.48}$$

$$S_1(\sigma)=\mathcal{F}\{A_1(\tau-\tau_2)\}e^{+\jmath\phi_2}-\frac{1}{2}S_{23}(\sigma)\tag{2.49}$$

2.1.3 Analytical Channel Splitting

In order to have an analytical form for the channel splitting method, a construct is needed to recreate the modulations in the Fourier domain. This is obtained through a Frequency Phase Matrix (FPM), which determines the functional form of the modulation and makes Fourier transforms a matter of looking up the correct row of a precalculated matrix (see Table 2.2) [2, 6].

Table 2.2: Frequency Phase Matrix (FPM) for $M = 1, 2, 3, 4$ sinusoidal modulations. Each FPM has an omitted weight of 2^{-M}.

	$\delta(\tau+\tau_1+\tau_2+\tau_3+\tau_4)$	$\delta(\tau-\tau_1+\tau_2+\tau_3+\tau_4)$	$\delta(\tau+\tau_1-\tau_2+\tau_3+\tau_4)$	$\delta(\tau-\tau_1-\tau_2+\tau_3+\tau_4)$	$\delta(\tau+\tau_1+\tau_2-\tau_3+\tau_4)$	$\delta(\tau-\tau_1+\tau_2-\tau_3+\tau_4)$	$\delta(\tau+\tau_1-\tau_2-\tau_3+\tau_4)$	$\delta(\tau-\tau_1-\tau_2-\tau_3+\tau_4)$	$\delta(\tau+\tau_1+\tau_2+\tau_3-\tau_4)$	$\delta(\tau-\tau_1+\tau_2+\tau_3-\tau_4)$	$\delta(\tau+\tau_1-\tau_2+\tau_3-\tau_4)$	$\delta(\tau-\tau_1-\tau_2+\tau_3-\tau_4)$	$\delta(\tau+\tau_1+\tau_2-\tau_3-\tau_4)$	$\delta(\tau-\tau_1+\tau_2-\tau_3-\tau_4)$	$\delta(\tau+\tau_1-\tau_2-\tau_3-\tau_4)$	$\delta(\tau-\tau_1-\tau_2-\tau_3-\tau_4)$	
cccc	+1	+1	+1	+1	+1	+1	+1	+1	+1	+1	+1	+1	+1	+1	+1	+1	b_{0000}
sccc	$+\jmath$	$-\jmath$	$+\jmath$	$-\jmath$	$+\jmath$	$-\jmath$	$+\jmath$	$-\jmath$	$+\jmath$	$-\jmath$	$+\jmath$	$-\jmath$	$+\jmath$	$-\jmath$	$+\jmath$	$-\jmath$	b_{1000}
cscc	$+\jmath$	$+\jmath$	$-\jmath$	$-\jmath$	$+\jmath$	$+\jmath$	$-\jmath$	$-\jmath$	$+\jmath$	$+\jmath$	$-\jmath$	$-\jmath$	$+\jmath$	$+\jmath$	$-\jmath$	$-\jmath$	b_{0100}
sscc	−1	+1	+1	−1	−1	+1	+1	−1	−1	+1	+1	−1	−1	+1	+1	−1	b_{1100}
ccsc	$+\jmath$	$+\jmath$	$+\jmath$	$+\jmath$	$-\jmath$	$-\jmath$	$-\jmath$	$-\jmath$	$+\jmath$	$+\jmath$	$+\jmath$	$+\jmath$	$-\jmath$	$-\jmath$	$-\jmath$	$-\jmath$	b_{0010}
scsc	−1	+1	−1	+1	+1	−1	+1	−1	−1	+1	−1	+1	+1	−1	+1	−1	b_{1010}
cssc	−1	−1	+1	+1	+1	+1	−1	−1	−1	−1	+1	+1	+1	+1	−1	−1	b_{0110}
ssssc	$-\jmath$	$+\jmath$	$+\jmath$	$-\jmath$	$+\jmath$	$-\jmath$	$-\jmath$	$+\jmath$	$-\jmath$	$+\jmath$	$+\jmath$	$-\jmath$	$+\jmath$	$-\jmath$	$-\jmath$	$+\jmath$	b_{1110}
cccs	$+\jmath$	$+\jmath$	$+\jmath$	$+\jmath$	$+\jmath$	$+\jmath$	$+\jmath$	$+\jmath$	$-\jmath$	$-\jmath$	$-\jmath$	$-\jmath$	$-\jmath$	$-\jmath$	$-\jmath$	$-\jmath$	b_{0001}
sccs	−1	+1	−1	+1	−1	+1	−1	+1	+1	−1	+1	−1	+1	−1	+1	−1	b_{1001}
cscs	−1	−1	+1	+1	−1	−1	+1	+1	+1	+1	−1	−1	+1	+1	−1	−1	b_{0101}
sscs	$-\jmath$	$+\jmath$	$+\jmath$	$-\jmath$	$-\jmath$	$+\jmath$	$+\jmath$	$-\jmath$	$+\jmath$	$-\jmath$	$-\jmath$	$+\jmath$	$+\jmath$	$-\jmath$	$-\jmath$	$+\jmath$	b_{1101}
ccss	−1	−1	−1	−1	+1	+1	+1	+1	+1	+1	+1	+1	−1	−1	−1	−1	b_{0011}
scss	$-\jmath$	$+\jmath$	$-\jmath$	$+\jmath$	$+\jmath$	$-\jmath$	$+\jmath$	$-\jmath$	$+\jmath$	$-\jmath$	$+\jmath$	$-\jmath$	$-\jmath$	$+\jmath$	$-\jmath$	$+\jmath$	b_{1011}
csss	$-\jmath$	$-\jmath$	$+\jmath$	$+\jmath$	$+\jmath$	$+\jmath$	$-\jmath$	$-\jmath$	$+\jmath$	$+\jmath$	$-\jmath$	$-\jmath$	$-\jmath$	$-\jmath$	$+\jmath$	$+\jmath$	b_{0111}
ssss	+1	−1	−1	+1	−1	+1	+1	−1	−1	+1	+1	−1	+1	−1	−1	+1	b_{1111}

Using the FPM, $\underline{\mathbf{b}}$-vectors are defined as a representation of the modulations of each Stokes parameter (or Mueller matrix element). For example, the modulation $cos\phi_2$ of $S_1(\sigma)$ (see Eq. (2.13)) is defined as $\underline{\mathbf{b}}_{S1} = 1/2(1, 1)$ (see Table 2.2). By concatenating the appropriate $\underline{\mathbf{b}}$-vectors, we obtain a map for each Stokes vector (or Mueller matrix) element's splitting, called the $\underline{\underline{\mathbf{Q}}}$-matrix [2], which maps an input Stokes vector (or vectorized Mueller matrix) into a channel vector $\underline{\mathbf{C}}$ [6],

$$\underline{\mathbf{C}} = \underline{\underline{\mathbf{Q}}}\,\mathcal{F}^{-1}\{\underline{\mathbf{S}}(\sigma)\} \tag{2.50}$$

where $\underline{\mathbf{C}}$ is a matrix formed by concatenating the filtered channels of the autocorrelation function $C(\tau)$.

From the setup given by Oka and Kato [8], (see Fig. 2.1), all θ's are forced to be in steps of 45°, which collapses $cos(2\theta)$ and $sin(2\theta)$ to either ± 1 or 0. As a result, retardance is the only potential source of modulation [2].

From the autocorrelation function for an ideal SCS (Eq. (2.23)), we propose a template (see Table 2.3) for the $\underline{\underline{\mathbf{Q}}}$-matrix based on the local retardance factors, the elements of the thickness vector $\underline{\mathbf{d}} = (d_1, d_2)$ elements. We construct the $\underline{\underline{\mathbf{Q}}}$-matrix by rearranging the rows of the template following the relative positions of the channels, given by the local retardance factors comparison (see Table 2.1).

Table 2.3: SCS Q-matrix template

Index	OPD	S_0	S_1	S_2	S_3
4	$+\tau_1 - \tau_2$			$+1/8$	$-\jmath 1/8$
3	$+\tau_1 + \tau_2$			$-1/8$	$+\jmath 1/8$
2	$+\tau_2$		$+1/4$		
1	$+\tau_1$		0		
0	0	$+1/2$			
-1	$-\tau_1$		0		
-2	$-\tau_2$		$+1/4$		
-3	$-\tau_1 - \tau_2$			$-1/8$	$-\jmath 1/8$
-4	$-\tau_1 + \tau_2$			$+1/8$	$+\jmath 1/8$

The $\underline{\underline{\mathbf{Q}}}$-matrix has a cardinality $[N_C \times M]$ where N_C is the number of channels or modulations, given by the birefringent plates thicknesses (d_i) and Eq. (2.51), and $M = 4$ for the number of Stokes parameters (or $M = 16$ for the Mueller matrix elements) [2, 6].

$$N_C = 1 + 2\sum_i d_i \tag{2.51}$$

Nevertheless, the Eq. (2.51) of N_C given by Alenin and Tyo [2, 6] considers empty channels for some $\underline{\mathbf{d}}$-vectors and requires it to be an integer vector. To reduce the SCS $\underline{\underline{\mathbf{Q}}}$-matrix size, we consider N_C to be the number of different modulations obtained from Eq. (2.18) and shown in Table 2.1. This also helps us to avoid the analysis of empty channels or without information of interest.

What we need to extract the input Stokes vector is an inverse map, a matrix that tells which channels have to be combined in order to extract the Stokes vector [2]. That inverse map corresponds to the pseudo-inverse $\underline{\underline{\mathbf{Q}}}^{+}$, given by the Moore-Penrose generalized inverse (Eq. (2.32)).

$$\underline{\mathbf{S}}(\sigma) = \underline{\underline{\mathbf{Q}}}^{+}\mathcal{F}\{\underline{\mathbf{C}}\} \tag{2.52}$$

It is important to note that a phase shift must be corrected when applying the Fourier transform to the filtered channels, as in the channel splitting method. For this matter, we analyse each possible channel and multiply it by a phase cancellation term corresponding to the retardance ϕ_i to each channel $C_i(\tau)$. This approach is mostly helpful for cases with crosstalk between channels (e.g., $\tau_1 - \tau_2 = \tau_2$).

2.2 MMCS Setup

The MMCS consists of a polarization states generator (PSG) and a polarization states analyzer (PSA), with the sample placed in between, followed by a spectrometer. The MMCS setup studied is given by Eq. (2.53), whose PSA is the same studied for the SCS in Section 2.1 and the PSG is a mirror image of the PSA (see Fig. 2.2). It is observed that where the SCS generally works with 7 encoding channels, the MMCS works with up to 49 channels, so that spectrometer resolution requirements are more stringent [20].

$$\begin{aligned}\underline{\underline{\mathbf{W}}} =&\underline{\underline{\mathbf{M}}}_{P2}(0)\underline{\underline{\mathbf{M}}}_{R4}(\phi_4,\pi/2)\underline{\underline{\mathbf{M}}}_{R3}(\phi_3,0)\underline{\underline{\mathbf{M}}}\times\\ &\times\underline{\underline{\mathbf{M}}}_{R2}(\phi_2,0)\underline{\underline{\mathbf{M}}}_{R1}(\phi_1,\pi/2)\underline{\underline{\mathbf{M}}}_{P1}(0)\end{aligned} \tag{2.53}$$

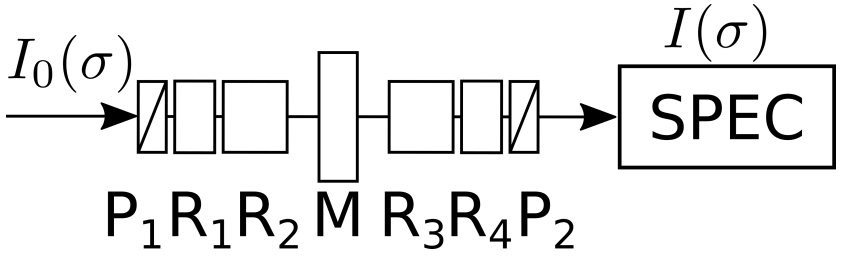

Figure 2.2: Mueller matrix channeled spectropolarimeter setup.

For this setup, an unpolarized light source with intensity $I_0(\sigma)$ and a detector unsensitive to polarization is considered. The irradiance measured by the detector is given by

$$I(\sigma) = \begin{pmatrix}1 & 0 & 0 & 0\end{pmatrix}\underline{\underline{\mathbf{W}}}\begin{pmatrix}I_0 & 0 & 0 & 0\end{pmatrix}^T \tag{2.54}$$

Substituting the system matrix and developing the equation.

$$\begin{aligned}I(\sigma) = &\begin{pmatrix}1 & 0 & 0 & 0\end{pmatrix}\underline{\underline{\mathbf{M}}}_{P2}(0)\underline{\underline{\mathbf{M}}}_{R4}(\phi_4,\pi/2)\underline{\underline{\mathbf{M}}}_{R3}(\phi_3,0)\underline{\underline{\mathbf{M}}}\times\\ &\times\underline{\underline{\mathbf{M}}}_{R2}(\phi_2,0)\underline{\underline{\mathbf{M}}}_{R1}(\phi_1,\pi/2)\underline{\underline{\mathbf{M}}}_{P1}(0)\begin{pmatrix}I_0 & 0 & 0 & 0\end{pmatrix}^T\end{aligned} \tag{2.55}$$

$$
\begin{aligned}
I(\sigma) =& \frac{1}{4} I_0 \begin{pmatrix} 1 \\ 0 \\ 0 \\ 0 \end{pmatrix}^T \begin{pmatrix} 1 & cos\phi_4 & sin\phi_3 sin\phi_4 & -cos\phi_3 sin\phi_4 \\ 1 & cos\phi_4 & sin\phi_3 sin\phi_4 & -cos\phi_3 sin\phi_4 \\ 0 & 0 & 0 & 0 \\ 0 & 0 & 0 & 0 \end{pmatrix} \times \\
& \times \begin{pmatrix} m_{00} & m_{01} & m_{02} & m_{03} \\ m_{10} & m_{11} & m_{12} & m_{13} \\ m_{20} & m_{21} & m_{22} & m_{23} \\ m_{30} & m_{31} & m_{32} & m_{33} \end{pmatrix} \times \\
& \times \begin{pmatrix} 1 & 1 & 0 & 0 \\ cos\phi_1 & cos\phi_1 & 0 & 0 \\ sin\phi_1 sin\phi_2 & sin\phi_1 sin\phi_2 & 0 & 0 \\ sin\phi_1 cos\phi_2 & sin\phi_1 cos\phi_2 & 0 & 0 \end{pmatrix} \begin{pmatrix} 1 \\ 0 \\ 0 \\ 0 \end{pmatrix} \qquad (2.56)
\end{aligned}
$$

$$
I(\sigma) = \frac{1}{4} I_0(\sigma) X(\sigma) \qquad (2.57)
$$

where

$$
X(\sigma) = \begin{pmatrix} 1 & cos\phi_4 & sin\phi_3 sin\phi_4 & -cos\phi_3 sin\phi_4 \end{pmatrix} \underline{\underline{\mathbf{M}}} \begin{pmatrix} 1 \\ cos\phi_1 \\ sin\phi_1 sin\phi_2 \\ sin\phi_1 cos\phi_2 \end{pmatrix} \qquad (2.58)
$$

Therefore, the expected modulations of the MMCS are given by

$$
\begin{aligned}
X(\sigma) = & + m_{00} & & + m_{01} cos\phi_1 \\
& + m_{02} sin\phi_1 sin\phi_2 & & + m_{03} sin\phi_1 cos\phi_2 \\
& + m_{10} cos\phi_4 & & + m_{11} cos\phi_1 cos\phi_4 \\
& + m_{12} sin\phi_1 sin\phi_2 cos\phi_4 & & + m_{13} sin\phi_1 cos\phi_2 cos\phi_4 \\
& + m_{20} sin\phi_3 sin\phi_4 & & + m_{21} cos\phi_1 sin\phi_3 sin\phi_4 \\
& + m_{22} sin\phi_1 sin\phi_2 sin\phi_3 sin\phi_4 & & + m_{23} sin\phi_1 cos\phi_2 sin\phi_3 sin\phi_4 \\
& - m_{30} cos\phi_3 sin\phi_4 & & - m_{31} cos\phi_1 cos\phi_3 sin\phi_4 \\
& - m_{32} sin\phi_1 sin\phi_2 cos\phi_3 sin\phi_4 & & - m_{33} sin\phi_1 cos\phi_2 cos\phi_3 sin\phi_4 \qquad (2.59)
\end{aligned}
$$

For the MMCS, we studied two methods: 1) the Measurement matrix method [21] and 2) the Analytical Channel Splitting method proposed by Alenin and Tyo [2, 6]. A Channel splitting method, similar to the one reviewed in Section 2.1.2, was developed by Hagen, Oka, and Dereniak [22] for a specific MMCS configuration, but is out of the scope of this thesis.

2.2.1 Measurement matrix

A similar procedure to the Mueller analysis of the SCS is followed. For this method, a series of analyzing polarization states (vectors) and generating vectors are predetermined

$$\underline{\mathbf{A}}_n = \begin{pmatrix} a_0 & a_1 & a_2 & a_3 \end{pmatrix}_n^T \tag{2.60}$$

$$\underline{\mathbf{G}}_n = \begin{pmatrix} g_0 & g_1 & g_2 & g_3 \end{pmatrix}_n^T \tag{2.61}$$

so the irradiance measured is given by

$$I(\sigma_n) = \underline{\mathbf{A}}_n^T \, \underline{\underline{\mathbf{M}}} \, \underline{\mathbf{G}}_n \tag{2.62}$$

which can be shown is equivalent to

$$I(\sigma_n) = \underline{\mathbf{D}}_n'^T \, \underline{\mathbf{M}}' \tag{2.63}$$

where $\underline{\mathbf{D}}_n'$ is the dyad product $\underline{\underline{\mathbf{D}}}_n = \underline{\mathbf{A}}_n \underline{\mathbf{G}}_n^T$ reshaped into a vector

$$\underline{\mathbf{D}}_n' = \underline{\mathbf{A}}_n \otimes \underline{\mathbf{G}}_n \tag{2.64}$$

$$= \begin{pmatrix} a_0 g_0 & \dots & a_0 g_3 & \dots & a_3 g_0 & \dots & a_3 g_3 \end{pmatrix}_n^T \tag{2.65}$$

and $\underline{\mathbf{M}}'$ is the Mueller matrix reshaped into a Mueller vector [6],

$$\underline{\mathbf{M}}' = (m_{00}\, m_{01}\, m_{02}\, m_{03}\, m_{10}\, m_{11}\, m_{12}\, m_{13}\, m_{20}\, m_{21}\, m_{22}\, m_{23}\, m_{30}\, m_{31}\, m_{32}\, m_{33})^T \tag{2.66}$$

Developing and rearranging Eq. (2.63) yields

$$\underline{\mathbf{I}} = \underline{\underline{\mathbf{W}}}' \, \underline{\mathbf{M}}' \tag{2.67}$$

where

$$\underline{\underline{\mathbf{W}}}' = \begin{pmatrix} \underline{\mathbf{D}}_0' & \underline{\mathbf{D}}_1' & \dots & \underline{\mathbf{D}}_{N-1}' \end{pmatrix}^T \tag{2.68}$$

Therefore, $\underline{\underline{\mathbf{W}}}'$ is a matrix containing the states of analysis-generation defined by the combination of the PSA and PSG of the MMCS [2, 6].

The extraction of the Mueller matrix elements is achieved by inverting the process:

$$\underline{\mathbf{M}}' = \underline{\underline{\mathbf{W}}}'^{+} \underline{\mathbf{I}} \tag{2.69}$$

where $\underline{\underline{\mathbf{W}}}'^{+}$ is the pseudo-inverse of $\underline{\underline{\mathbf{W}}}'$, given by the Moore-Penrose generalized inverse (Eq. (2.32)). However, this method considers the $\underline{\underline{\mathbf{M}}}$-matrix invariant with wavenumber, therefore, it is used only as a reference.

2.2.2 Analytical Channel Splitting

This method corresponds to the Generalized Channeled Polarimetry methodology [6] and follows the same process described in Section 2.1.3. We propose a template (see Table 2.4) for the $\underline{\underline{\mathbf{Q}}}$-matrix of the MMCS with four retarders. It is important to mention that for the MMCS analysis the number of channels N_C is given by Eq. (2.51).

$$\underline{\mathbf{C}} = \underline{\underline{\mathbf{Q}}} \mathcal{F}^{-1}\{\underline{\mathbf{M}}'\} \tag{2.70}$$

$$\underline{\mathbf{M}}' = \underline{\underline{\mathbf{Q}}}^{+} \mathcal{F}\{\underline{\mathbf{C}}\} \tag{2.71}$$

Summarizing, the Measurement matrix method is used as a reference. This research is focused on the Generalized Channeled Polarimetry methodology proposed by Alenin and Tyo [2, 6].

Table 2.4: MMCS Q-matrix template.

Index	OPD	m_{00}	m_{01}	m_{02}	m_{03}	m_{10}	m_{11}	m_{12}	m_{13}	m_{20}	m_{21}	m_{22}	m_{23}	m_{30}	m_{31}	m_{32}	m_{33}	Factor
24	$+\tau_1-\tau_2-\tau_3-\tau_4$											-1	$+\jmath$			$-\jmath$	-1	1/16
23	$+\tau_1-\tau_2-\tau_3+\tau_4$											$+1$	$-\jmath$			$+\jmath$	$+1$	1/16
22	$+\tau_1-\tau_2+\tau_3-\tau_4$											$+1$	$-\jmath$			$-\jmath$	-1	1/16
21	$+\tau_1-\tau_2+\tau_3+\tau_4$											-1	$+\jmath$			$+\jmath$	$+1$	1/16
20	$+\tau_1+\tau_2-\tau_3-\tau_4$											$+1$	$+\jmath$			$+\jmath$	-1	1/16
19	$+\tau_1+\tau_2-\tau_3+\tau_4$											-1	$-\jmath$			$-\jmath$	$+1$	1/16
18	$+\tau_1+\tau_2+\tau_3-\tau_4$											-1	$-\jmath$			$+\jmath$	-1	1/16
17	$+\tau_1+\tau_2+\tau_3+\tau_4$											$+1$	$+\jmath$			$-\jmath$	$+1$	1/16
16	$+\tau_1-\tau_3-\tau_4$										-1				$-\jmath$			1/8
15	$+\tau_1-\tau_3+\tau_4$										$+1$				$+\jmath$			1/8
14	$+\tau_1+\tau_3-\tau_4$										$+1$				$-\jmath$			1/8
13	$+\tau_1+\tau_3+\tau_4$										-1				$+\jmath$			1/8
12	$+\tau_1-\tau_2-\tau_4$							$+1$	$-\jmath$									1/8
11	$+\tau_1-\tau_2+\tau_4$							$+1$	$-\jmath$									1/8
10	$+\tau_1+\tau_2-\tau_4$							-1	$-\jmath$									1/8
9	$+\tau_1+\tau_2+\tau_4$							-1	$-\jmath$									1/8
8	$+\tau_3-\tau_4$									$+1$				$-\jmath$				1/4
7	$+\tau_3+\tau_4$									-1				$+\jmath$				1/4
6	$+\tau_1-\tau_4$						$+1$											1/4
5	$+\tau_1+\tau_4$						$+1$											1/4
4	$+\tau_1-\tau_2$			$+1$	$-\jmath$													1/4
3	$+\tau_1+\tau_2$			-1	$-\jmath$													1/4
2	$+\tau_4$					$+1$												1/2

Continuation of Table 2.4

Index	OPD	m_{00}	m_{01}	m_{02}	m_{03}	m_{10}	m_{11}	m_{12}	m_{13}	m_{20}	m_{21}	m_{22}	m_{23}	m_{30}	m_{31}	m_{32}	m_{33}	Factor
1	$+\tau_1$		$+1$															1/2
0	0	$+1$																1
-1	$-\tau_1$		$+1$															1/2
-2	$-\tau_4$					$+1$												1/2
-3	$-\tau_1-\tau_2$			-1	$+\jmath$													1/4
-4	$-\tau_1+\tau_2$			$+1$	$+\jmath$													1/4
-5	$-\tau_1-\tau_4$						$+1$											1/4
-6	$-\tau_1+\tau_4$						$+1$											1/4
-7	$-\tau_3-\tau_4$									-1				$-\jmath$				1/4
-8	$-\tau_3+\tau_4$									$+1$				$+\jmath$				1/4
-9	$-\tau_1-\tau_2-\tau_4$							-1	$+\jmath$									1/8
-10	$-\tau_1-\tau_2+\tau_4$							-1	$+\jmath$									1/8
-11	$-\tau_1+\tau_2-\tau_4$							$+1$	$+\jmath$									1/8
-12	$-\tau_1+\tau_2+\tau_4$							$+1$	$+\jmath$									1/8
-13	$-\tau_1-\tau_3-\tau_4$										-1				$-\jmath$			1/8
-14	$-\tau_1-\tau_3+\tau_4$										$+1$				$+\jmath$			1/8
-15	$-\tau_1+\tau_3-\tau_4$										$+1$				$-\jmath$			1/8
-16	$-\tau_1+\tau_3+\tau_4$										-1				$+\jmath$			1/8
-17	$-\tau_1-\tau_2-\tau_3-\tau_4$											$+1$	$-\jmath$			$+\jmath$	$+1$	1/16
-18	$-\tau_1-\tau_2-\tau_3+\tau_4$											-1	$+\jmath$			$-\jmath$	-1	1/16
-19	$-\tau_1-\tau_2+\tau_3-\tau_4$											-1	$+\jmath$			$+\jmath$	$+1$	1/16
-20	$-\tau_1-\tau_2+\tau_3+\tau_4$											$+1$	$-\jmath$			$-\jmath$	-1	1/16
-21	$-\tau_1+\tau_2-\tau_3-\tau_4$											-1	$-\jmath$			$-\jmath$	$+1$	1/16
-22	$-\tau_1+\tau_2-\tau_3+\tau_4$											$+1$	$+\jmath$			$+\jmath$	-1	1/16

Continuation of Table 2.4

Index	OPD	m_{00}	m_{01}	m_{02}	m_{03}	m_{10}	m_{11}	m_{12}	m_{13}	m_{20}	m_{21}	m_{22}	m_{23}	m_{30}	m_{31}	m_{32}	m_{33}	Factor
-23	$-\tau_1+\tau_2+\tau_3-\tau_4$											$+1$	$+\jmath$			$-\jmath$	$+1$	1/16
-24	$-\tau_1+\tau_2+\tau_3+\tau_4$											-1	$-\jmath$			$+\jmath$	-1	1/16

Chapter 3

Simulations, results, and discussion of CS systems

In this chapter, the methodology for the simulation of the SCS and the MMCS is described, as well as the sources of error that might be encountered. The results of some simulated configurations are reported as well, along a discussion on the effects of the sources of error on SCS and MMCS systems.

3.1 Methodology for the CS simulation

The general methodology for both the SCS and the MMCS simulations is as follows:

1. Select a sample (either a Stokes vector or a Mueller matrix).
2. Define the CS configuration, including the spectral range $[\sigma_{min}, \sigma_{max}]$, the spectral resolution $\Delta\sigma$, the number of pixels N in the irradiance curve, the nominal global retardance factor, the nominal local retardance factors (thickness' ratio), and the sources of error
   - Retardance errors (Δd_i)
   - Alignment errors (ϵ_i)
   - Gaussian noise amplitude
3. Run the methods reviewed to simulate the irradiance to be measured.
4. Run the inverse methods to extract the samples (the Stokes vector or the Mueller matrix) from the irradiance measured, for this purpose consider the irradiance obtained with Eq. (2.9) for the SCS and Eq. (2.54) for the MMCS.

3.1.1 Experiment setup

For the SCS we have two thick birefringent plates followed by a linear polarizer. The transmission axis of the linear polarizer is horizontal and is the system's reference (0°). The retarders are then aligned with the polarizer at 0° ($\underline{\underline{\mathbf{M}}}_{R1}$) and at 45° ($\underline{\underline{\mathbf{M}}}_{R2}$), see Fig. 2.1. For the MMCS, the system is mirrored as discussed in Section 2.2, see Fig. 2.2. For the spectrometer, a σ-wavenumber range from $1.4954 \times 10^4[cm^{-1}]$ to $1.8408 \times 10^4[cm^{-1}]$ ($\lambda \sim 543 - 668[nm]$), with a sampling number N of 1024 and 2048 for the SCS and MMCS, respectively, and a corresponding wavenumber resolution

of $(\sigma_{max} - \sigma_{min})/N$ were considered. The high-order retarders are assumed to be made of quartz, and the birefringence was calculated using a model proposed by Ghosh [23].

3.2 Reconstruction artifacts

Reconstruction artifacts, associated with the Fast Fourier Transform (FFT) method applied, appear when extracting the Stokes vector or the Mueller matrix due to a lack of periodicity in the irradiance measured, which contradicts the FFT supposition of a periodic function.

Therefore, before computing the FFT, to prevent discontinuities in the periodic continuation, apodization has to be applied to the raw data [15, 24, 25]. Apodization refers to multiplication by a window function which falls to zero at the edges of the system's spectral range [24]. In this work, a Hann window was applied [26],

$$\omega = \frac{1}{2}\Big(1 - cos\frac{2\pi n}{N}\Big),\ n = 0, 1, 2, ..., N-1 \tag{3.1}$$

where N is the number of pixels of the spectrum. However this step may aggravate the discrepancies at the edges of the spectrum, where the division is nearly by zero [24].

For some SCS simulations, we were able to solve the parameter S_0 with high precision without applying the Hann window. Because of this, two parallel processes were considered: 1) apply the FFT just to recover S_0 and 2) apply the Hann window and the FFT to solve the parameters S_1, S_2, and S_3. Nevertheless, for other cases it was observed that S_0 also had reconstruction artifacts, with increased error in the centre band. For this reason, we decided to apply the Hann window for all the Stokes parameters, and consequently to all Mueller matrix elements.

Other methods have been proposed, e.g. Lee proposed an iterative method to reduce the secondary frequencies by which N measurements are performed to analyse the Stokes vectors in N frequencies of interest [27]. It is worth mentioning that, at first, these reconstruction artifacts were attributed to the non-linearity of birefringence $B(\sigma)$, because this behaviour was less pronounced for smaller wavenumber ranges. Nevertheless, it was later proved this was not the case. We simulated the birefringence as the linear function $B(\sigma) = m\sigma + b$ and the error persisted.

3.3 Sources of error

Several sources of error can interfere in channeled polarimetry systems:

- Reconstruction artifacts due to crosstalk

  Crosstalk between adjacent channels occurs when the spectral or spatial features of the scene have high frequency content. Since the modulated Stokes parameters are not band-limited, this high frequency content is distributed across the Fourier domain, and consequently aliases into the neighbouring channels. These aliasing effects appear as false polarimetric signatures after reconstruction [1].

- Temperature variations

  When a uniaxial crystal experiences a temperature change, the crystal will expand or contract based on its coefficient of thermal expansion (CTE). Consequently, the thickness of the retarder can increase or decrease depending on the environmental conditions [28].

- Dichroism

  Another error source for CS comes from dichroism. In a crystal, differing amounts of absorption between the ordinary and extraordinary axes can result in diattenuation [29, 30].

- Dispersion

  Birefringence dispersion in the crystal is an additional source of error in CS, because the higher order nonlinear dispersion terms produce a small continuum of carrier frequencies (i.e., a chirped carrier frequency) [24].

The sources of error considered in this work are:

- Retardance error

  Owing to the manufacture tolerance, the thickness of high-order retarders may deviate from theoretical values, causing the retardations to change [15]. Therefore, a fabrication error Δd_i was considered. It was assumed that the plates have completely flat and parallel faces.

- Alignment error

  The assembly process of an instrument is not perfect; therefore, the alignment errors (ϵ_i) of high-order retarders are unavoidable [15].

- Gaussian noise

  The measured Mueller matrices are a mixture of pure (nondepolarizing) states, depolarization, and certainly noise (optical and electronic) [1, 31]. In this work, a Gaussian white noise source was considered. That is, a signal-independent additive zero-mean Gaussian distribution with variance σ^2 modelled for sensor noise, assuming that the fluctuations are statistically independent from one intensity measurement to the other [32]. Another main noise source mentioned in the literature is signal-dependent Poisson shot noise [31, 32, 33]. Although this type of noise was not considered in this work.

3.4 Evaluation metrics

To evaluate the performance of the SCS and MMCS setups of interest, we consider three figures of merit: (1) the root mean square error (RMS) of the extracted elements against their corresponding inputs, given by

$$RMS_a = \sqrt{\frac{1}{N}\sum_{i=1}^{N} a_i^2} \tag{3.2}$$

(2) the condition number (CN) of the $\underline{\underline{\mathbf{W}}}$-Mueller matrix and the $\underline{\underline{\mathbf{Q}}}$-matrix of the nominal setup, and 3) the equally weighted variance (EWV) [34] for the same matrices given by

$$EWV(\underline{\underline{\mathbf{A}}}) = Tr[(\underline{\underline{\mathbf{A}}}^{+})^T \underline{\underline{\mathbf{A}}}^{+}] \tag{3.3}$$

where $\underline{\underline{\mathbf{A}}}^{+}$ is the pseudo-inverse of $\underline{\underline{\mathbf{A}}}$, given by the Moore-Penrose generalized inverse (Eq. (2.32)).

These evaluation metrics are used to evaluate the noise immunity of the CS setups, considering that the goal of noise immunity is to minimize noise variance on the measured Stokes vector and to equalize noise variances on the last three Stokes parameters (S_1, S_2, S_3) with the least measurement channels [31]. For this work, an extracted parameter is considered immune to an error source when RMS-values are below 0.01.

3.5 SCS simulation, results and discussion

It was observed that channels get closer to each other for a greater number of pixels N. For the SCS simulations reported, a diffractive spectrometer with 1024 pixels and a Tungsten Halogen light source [35] were considered. The sample selected for the results reported is a completely polarized light source with equal energy energy in each of the Stokes parameters S_1, S_2, S_3 : $S = (1, 0.577, 0.577, 0.577)^T$.

3.5.1 Thickness ratio

Different Stokes vectors were tested to understand the performance of the SCS using the six configurations based on the thickness ratio $d_1 : d_2$ configurations reviewed in Chapter 2 (see Table 2.1), considering a global retardance factor $d_0 = 13[mm]$ for the thick birefringent retarders.

As expected, the configuration ($d_1 : d_2 = (2, 1)$) presents crosstalk, as shown in Fig. 3.1. This affects heavily the figures EWV and CN, compared to the other five configurations (see Fig. 3.2). Nevertheless, the Stokes vector extraction was similarly acceptable for all six configurations, as shown in Fig. 3.3. It seems the EWV and the CN are not representative of the SCS performance, based on the thickness ratio.

From Fig. 3.1, it is observed that the configurations $(3, 1)$, $(1, 3)$, and $(1, 2)$ provide a better distribution of the channels. The configuration $(2, 1)$ also provides a good distribution of channels, but presents crosstalk. For further tests, we decided to focus on the configuration $(3, 1)$ ($d_1 > 2d_2$), which was also used by Oka and Kato [8]. By changing the ratio $d_1 : d_2$ it is observed that (1) for $d_1 > d_2$ the channels at $\pm\tau_2$ remain stationary relative to d_2 and the channels $\pm(\tau_1 - \tau_2)$ and $\pm(\tau_1 + \tau_2)$ depart from the center as d_1 increases, maintaining a separation of $2\tau_2$, and (2) for $d_1 < d_2$ all channels ($\pm\tau_2$, $\pm(\tau_1 - \tau_2)$, and $\pm(\tau_1 + \tau_2)$) move in direct proportion to d_2 and with a separation of τ_1. Although, it should be mentioned that, for the second case, the channels $\pm(\tau_1 - \tau_2)$ are inverted along the center channel.

Another figure of merit used in this work is the RMS of the extracted Stokes parameters using the Channel Splitting and the Analytical Channel Splitting methods, see Fig. 3.4. The RMS provides a better picture of the performance of the SCS for different thickness ratios. To avoid the discrepancies at the edges, a consequence of apodization, of the Stokes parameters curves, the RMS was calculated for a reduced wavenumber range

from $1.5 \times 10^4[cm^{-1}]$ to $1.83 \times 10^4[cm^{-1}]$. It is worth mentioning that, even though it presents crosstalk, the configuration $(2, 1)$ had the lowest RMS-scores for S_2 and S_3. This is attributed to channels being tightly packed and uniformly spaced, resulting in the effective separation of the expected channels.

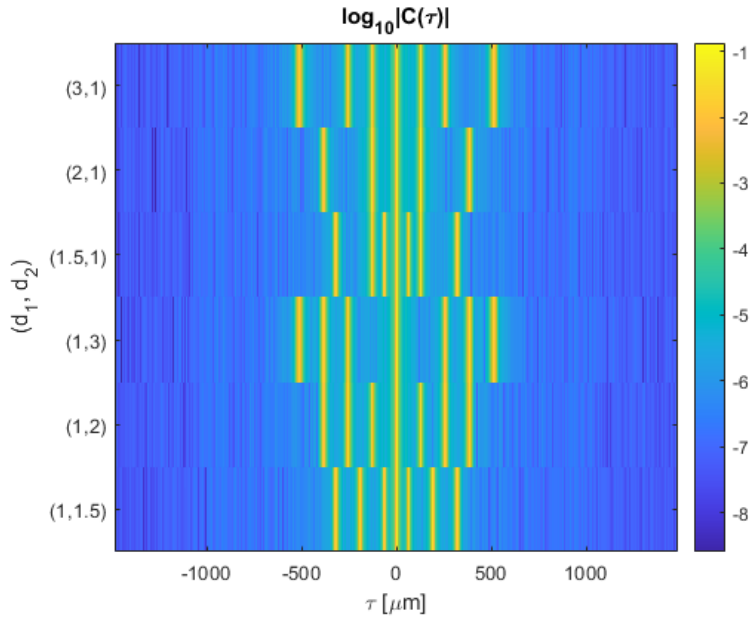

Figure 3.1: Autocorrelation function $|C(\tau)|$ for the SCS with different thickness ratios and a global retardance factor $d_0 = 13[mm]$.

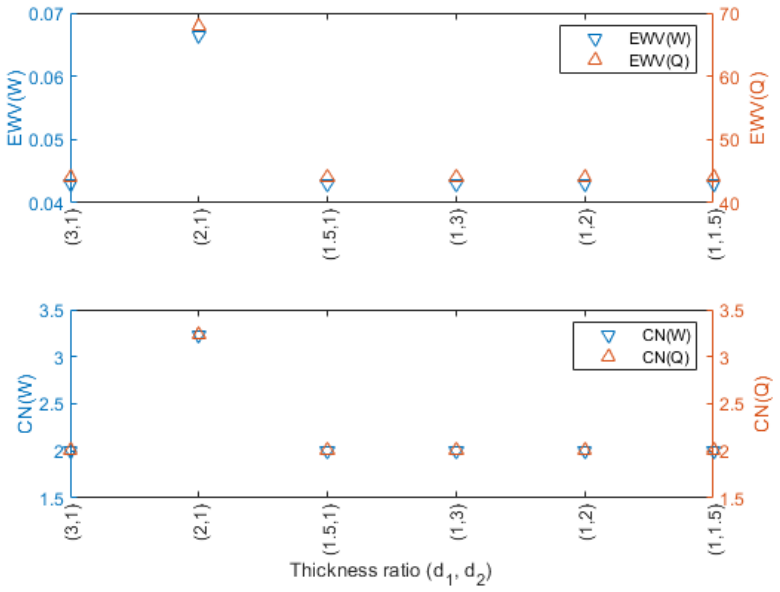

Figure 3.2: EWV and CN against the thickness ratio of the SCS.

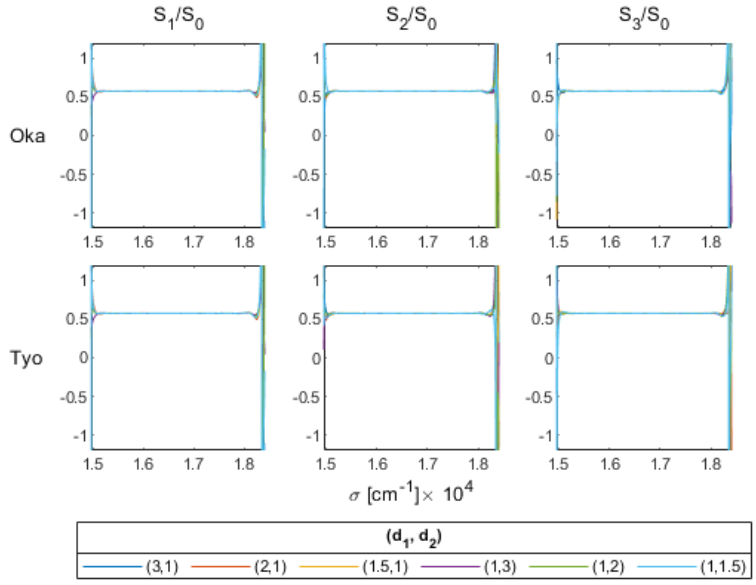

Figure 3.3: Normalized Stokes parameters for the Channel Splitting and the Analytical Channel Splitting methods (labeled as Oka and Tyo, respectively).

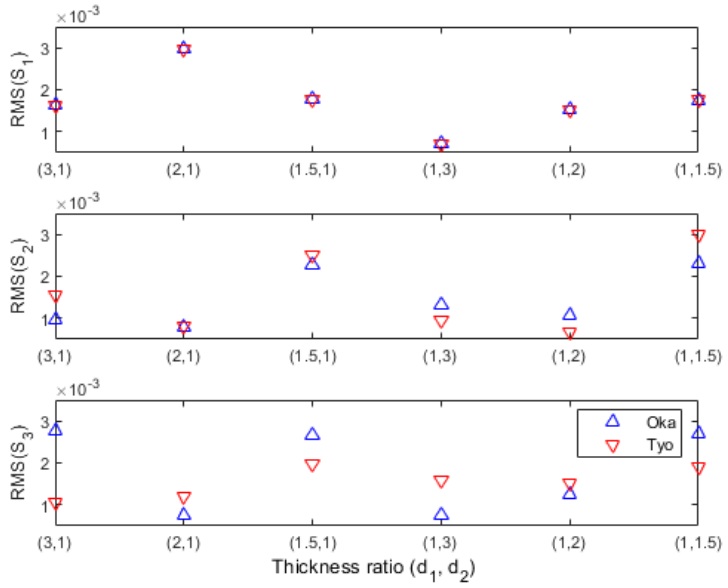

Figure 3.4: $RMS(S_i)$ against the thickness ratio of the SCS, for $i = 1, 2, 3$. The Channel Splitting and the Analytical Channel Splitting methods are labeled as Oka and Tyo, respectively.

3.5.2 Global retardance factor

To study the global retardance factor d_0, values from 5 to 20$[mm]$ were considered. In Fig. 3.5 and 3.6 are shown the $EWV(W)$ and $CN(W)$ plots, respectively, against the global retardance factor d_0. It is observed that the lowest values were obtained for $d_0 = 14, 15[mm]$. However it is important to note that the input Stokes vector was acceptably extracted for all the d_0-values considered, as shown in Fig. 3.7.

In Fig. 3.8 are shown the RMS plots for the Stokes parameters S_1, S_2, and S_3, respectively, for the Channel Splitting and the Analytical Channel Splitting methods (labeled as Oka and Tyo, respectively). In general terms, it is also observed that the SCS performance improved as the global retardance factor increased. This is expected, as the separation between channels is directly proportional to d_0 (see Fig. 3.9), which allows a better filtering process (using the same window, in this work a window of 20 pixels in the τ-domain was considered). The performance for small values of d_0 could be improved by analysing the window width parameter for each d_0-value. Sabatke *et al.* [24] suggest a τ bandwidth equal to the OPD of the thinner retarder (Bd), but this was not tested in this work. It is considered that $d_0 = 17[mm]$ offered the best performance overall, comparing the RMS plots for the three Stokes parameters. In other tests, where a light source with constant intensity was considered, the lowest $RMS(S_i)$ scores were obtained with $d_0 = 17[mm]$.

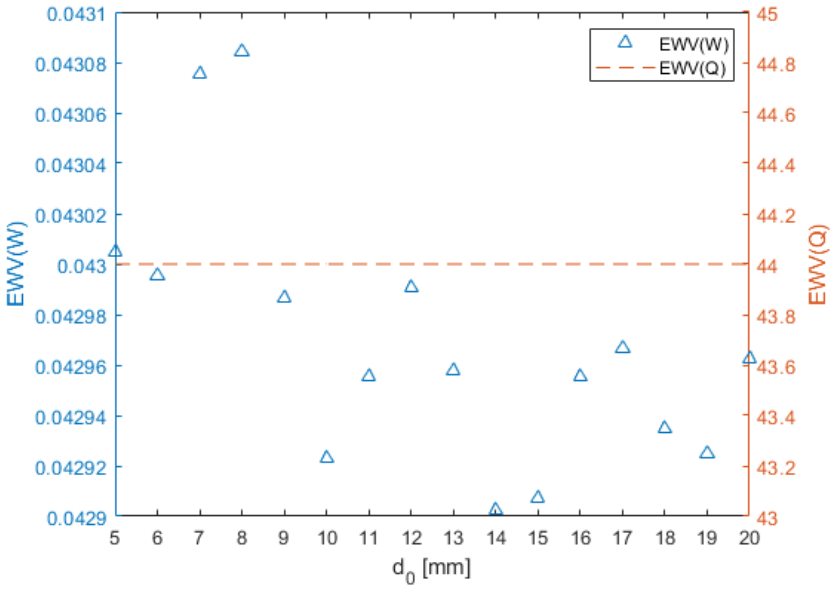

Figure 3.5: EWV against the global retardance factor d_0.

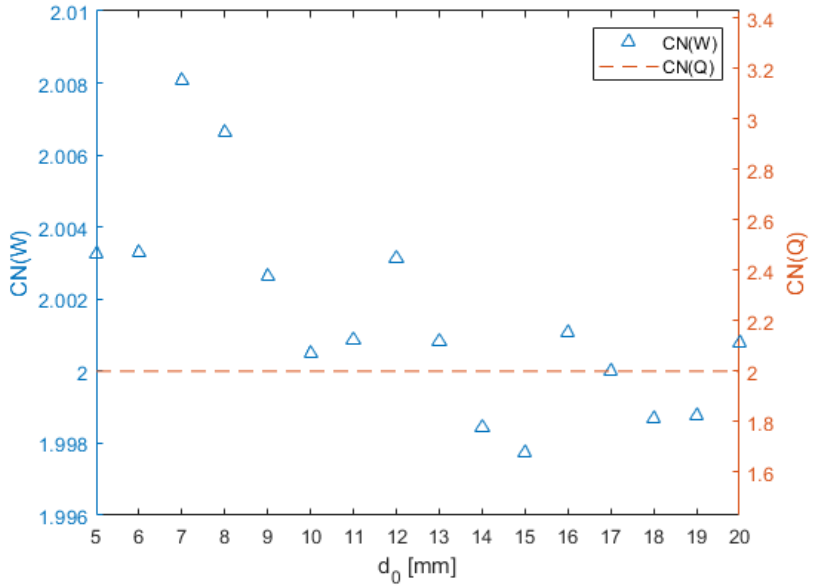

Figure 3.6: CN against the global retardance factor d_0.

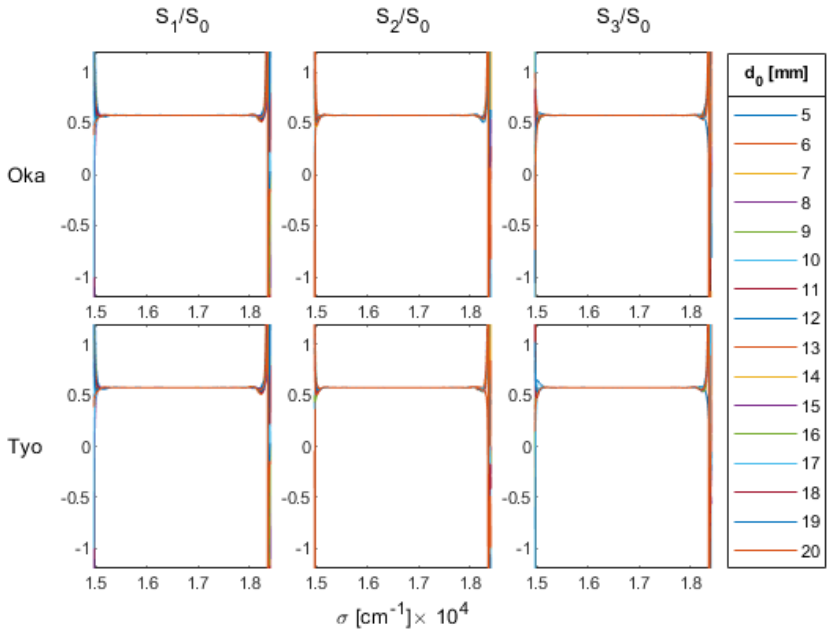

Figure 3.7: Normalized Stokes parameters for different global retardance factors d_0. The Channel Splitting and the Analytical Channel Splitting methods are labeled as Oka and Tyo, respectively.

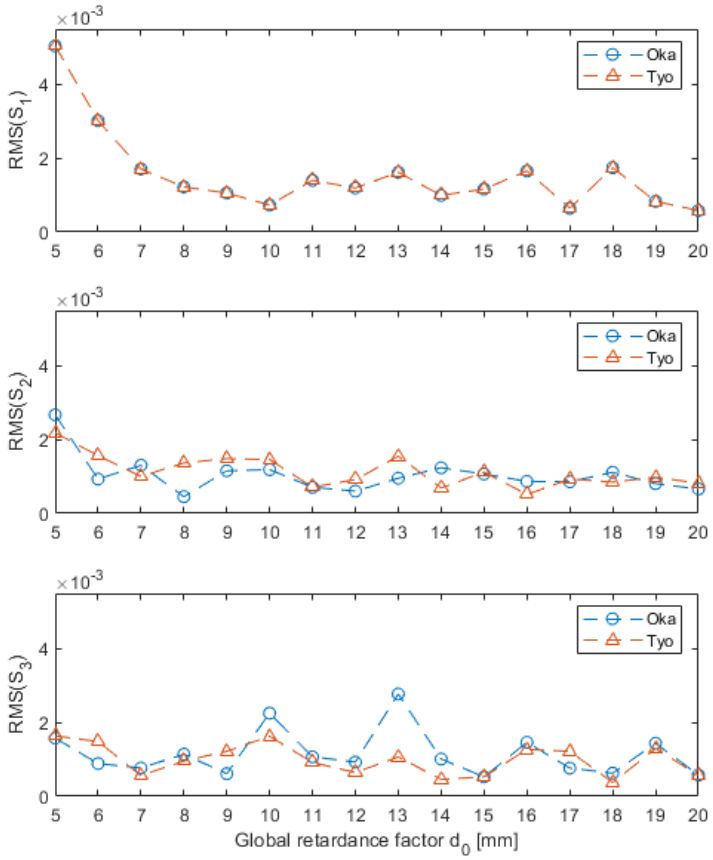

Figure 3.8: $RMS(S_i)$ against the global retardance factor of the SCS, for $i = 1, 2, 3$. The Channel Splitting and the Analytical Channel Splitting methods are labeled as Oka and Tyo, respectively.

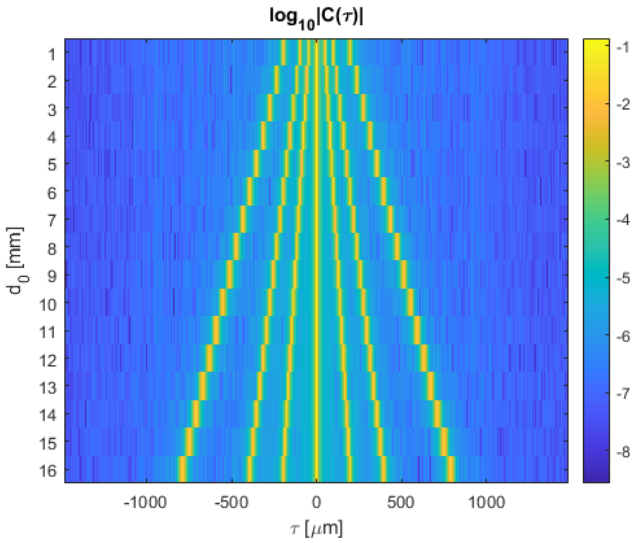

Figure 3.9: Autocorrelation function $|C(\tau)|$ of the SCS output for different global retardance factors d_0.

3.5.3 Retardance error

For the retarders a fabrication tolerance of $\pm 5[\mu m]$ was considered. This value was taken from manufacturers tolerances offered for custom thick birefringent quartz plates. Three global retardance factors were considered: (1) $13[mm]$, value reported in a literature example [8], (2) $14[mm]$, the value with the lowest $EWV(\underline{\underline{\mathbf{W}}})$, see Fig. 3.5, and (3) $17[mm]$, the global retardance factor which was considered to offer the best performance overall, see Fig. 3.8. The thickness ratio considered from this test forward was $(3, 1)$. The errors in retardance are perceived as the lateral displacement of the channels in the τ-domain, because the OPD is directly proportional to the retardance values.

In Fig. 3.10, 3.11, and 3.12 are shown the normalized Stokes parameters S_1/S_0, S_2/S_0, and S_3/S_0, respectively, for the Channel Splitting and the Analytical Channel Splitting methods (labeled as Oka and Tyo, respectively) when the retardance error occurs in the first retarder. It is observed that S_1 is immune to the retardance error, whereas, on the contrary, S_2 and S_3 are very sensitive to this error source. The $RMS(S_i)$ plots are shown in Fig. 3.13.

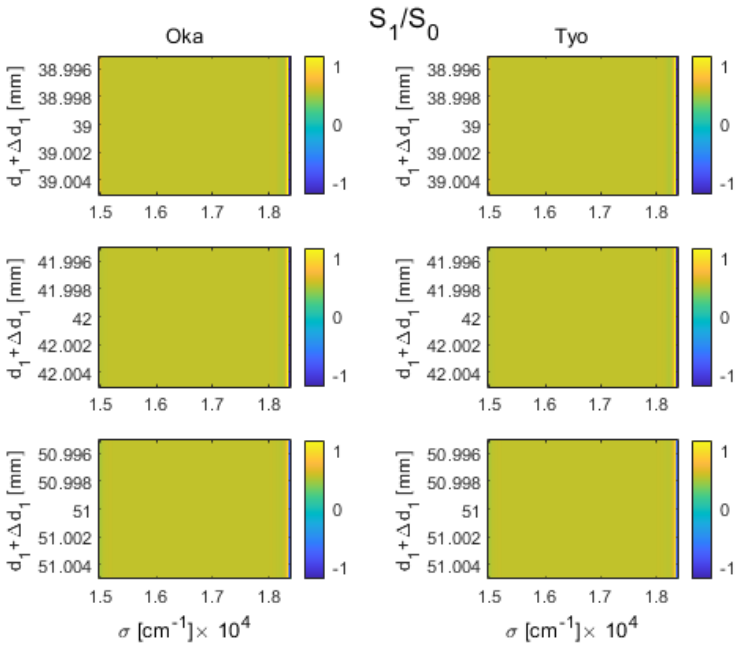

Figure 3.10: Normalized Stokes parameter S_1/S_0 against thickness error Δd_1. The Channel Splitting and the Analytical Channel Splitting methods are labeled as Oka and Tyo, respectively.

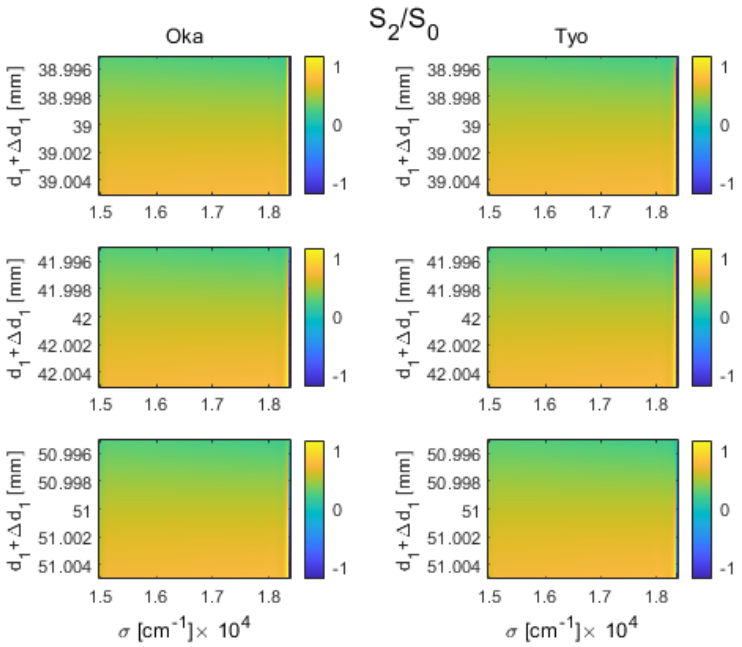

Figure 3.11: Normalized Stokes parameter S_2/S_0 against thickness error Δd_1. The Channel Splitting and the Analytical Channel Splitting methods are labeled as Oka and Tyo, respectively.

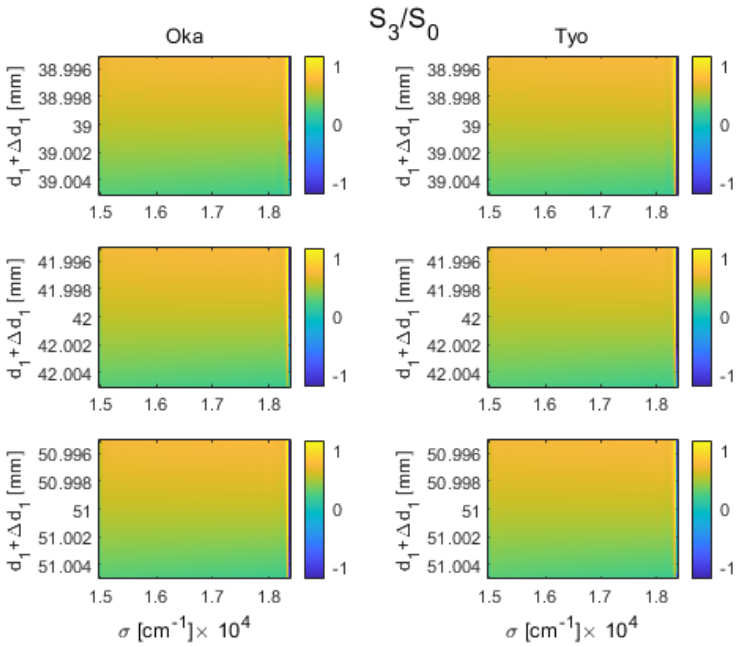

Figure 3.12: Normalized Stokes parameter S_3/S_0 against thickness error Δd_1. The Channel Splitting and the Analytical Channel Splitting methods are labeled as Oka and Tyo, respectively.

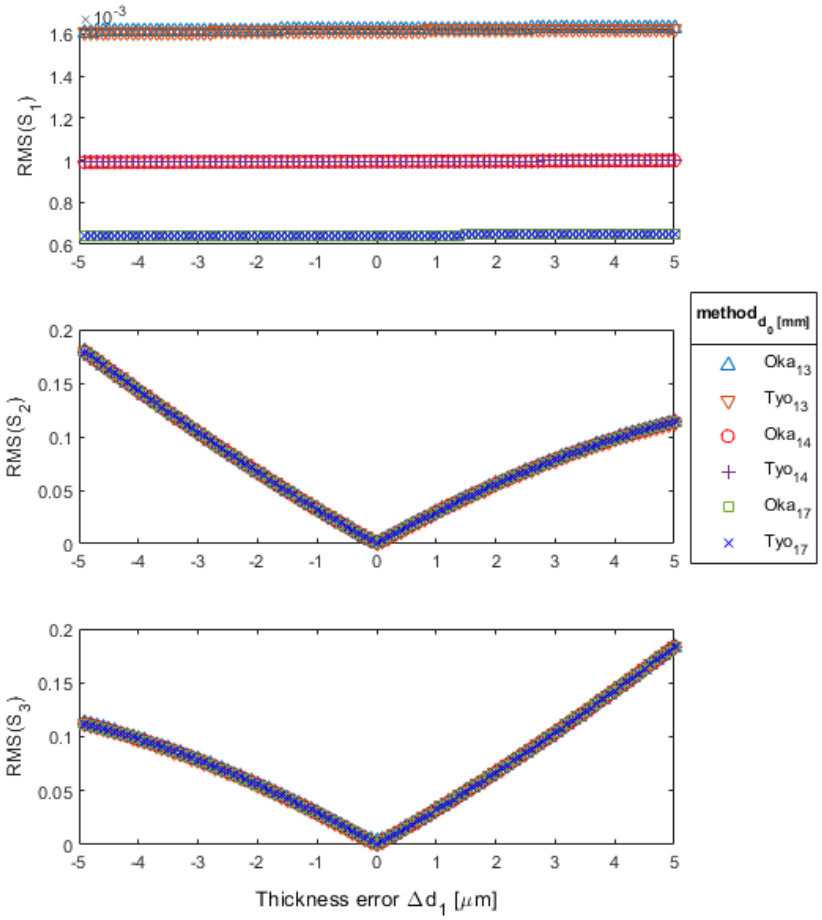

Figure 3.13: $RMS(S_i)$ against thickness error Δd_1, for $i = 1, 2, 3$. The Channel Splitting and the Analytical Channel Splitting methods are labeled as Oka and Tyo, respectively.

In Fig. 3.14, 3.15, and 3.16 are shown the normalized Stokes parameters S_1/S_0, S_2/S_0, and S_3/S_0, respectively, when the retardance error occurs in the second retarder. It is observed that S_1 is acceptably extracted, but it is not immune. For S_2 and S_3, the Analytical Channel Splitting method achieved a good performance, near to immunity, whereas the Channel Splitting method is highly sensitive to the error source. The $RMS(S_i)$ plots are shown in Fig. 3.17.

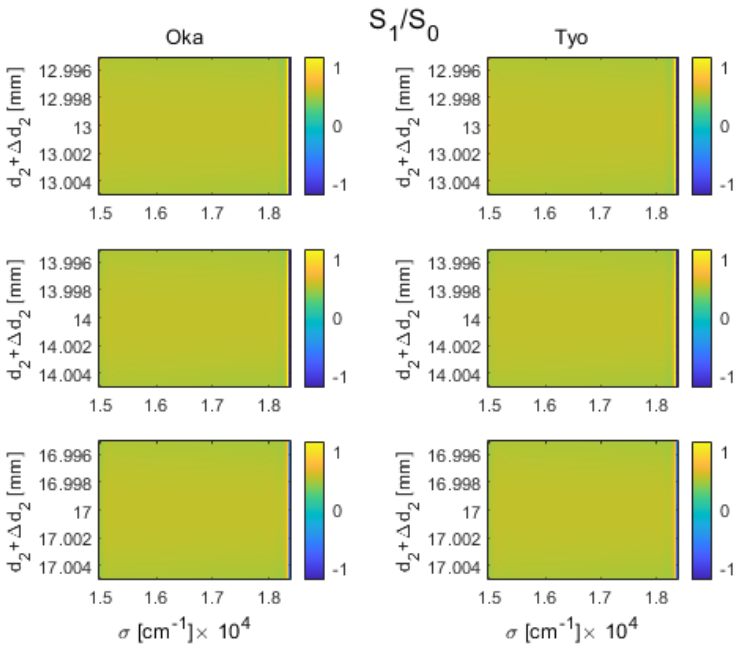

Figure 3.14: Normalized Stokes parameter S_1/S_0 against thickness error Δd_2. The Channel Splitting and the Analytical Channel Splitting methods are labeled as Oka and Tyo, respectively.

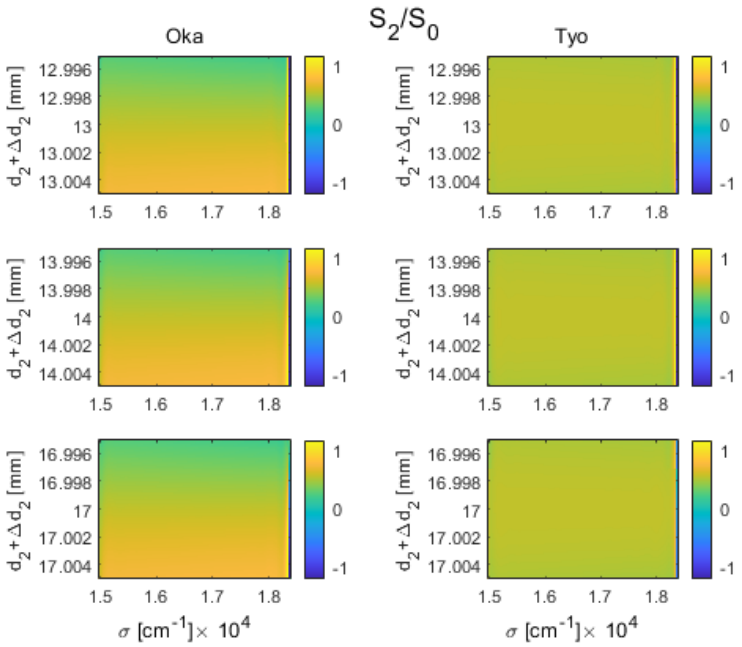

Figure 3.15: Normalized Stokes parameter S_2/S_0 against thickness error Δd_2. The Channel Splitting and the Analytical Channel Splitting methods are labeled as Oka and Tyo, respectively.

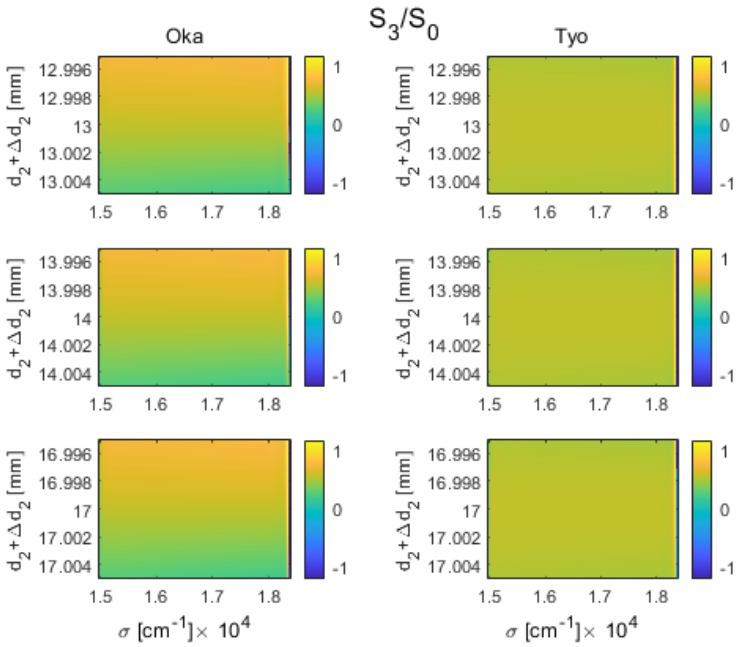

Figure 3.16: Normalized Stokes parameter S_3/S_0 against thickness error Δd_2. The Channel Splitting and the Analytical Channel Splitting methods are labeled as Oka and Tyo, respectively.

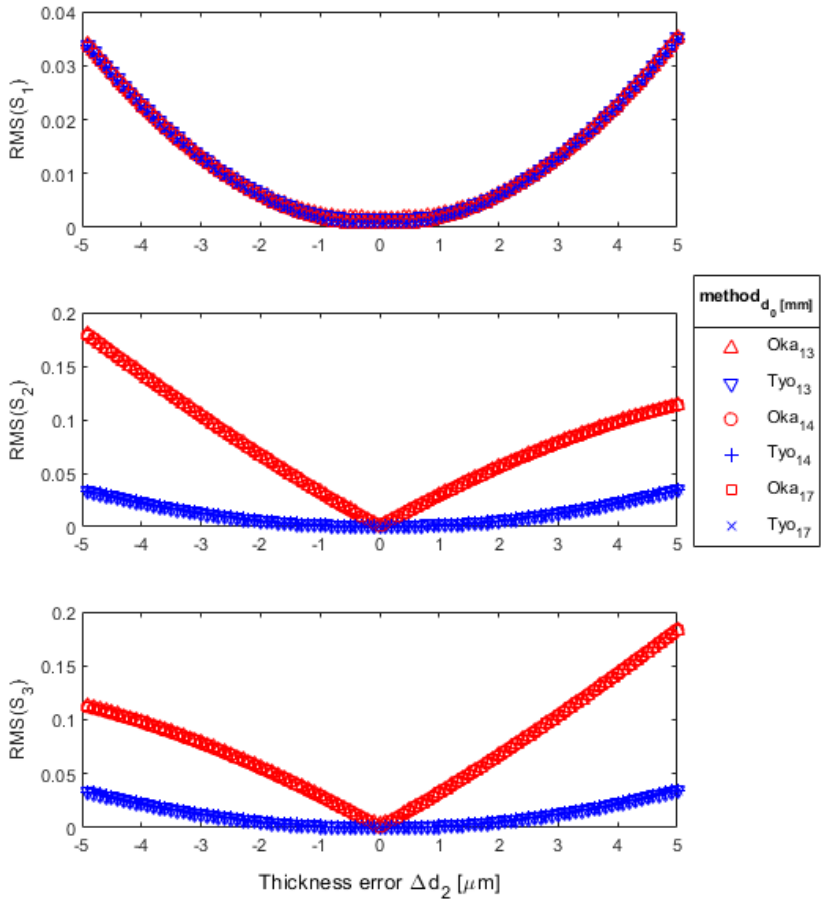

Figure 3.17: $RMS(S_i)$ against thickness error Δd_2, for $i = 1, 2, 3$. The Channel Splitting and the Analytical Channel Splitting methods are labeled as Oka and Tyo, respectively.

3.5.4 Alignment error

A tolerance of ± 5 degrees was considered for the retarders alignment. In Fig. 3.18, 3.19, and 3.20 are shown the normalized Stokes parameters S_1/S_0, S_2/S_0, and S_3/S_0, respectively, when the alignment error occurs in the first retarder. S_1 is very sensitive to the alignment error. For S_2, the Channel Splitting method offers acceptable results, but not immunity to the error source, whereas the Analytical Channel Splitting method is very sensitive to it. S_3 is very sensitive when applying the Channel Splitting method, but it is immune when the Analytical Channel Splitting method is applied. The $RMS(S_i)$ plots are shown in Fig. 3.21.

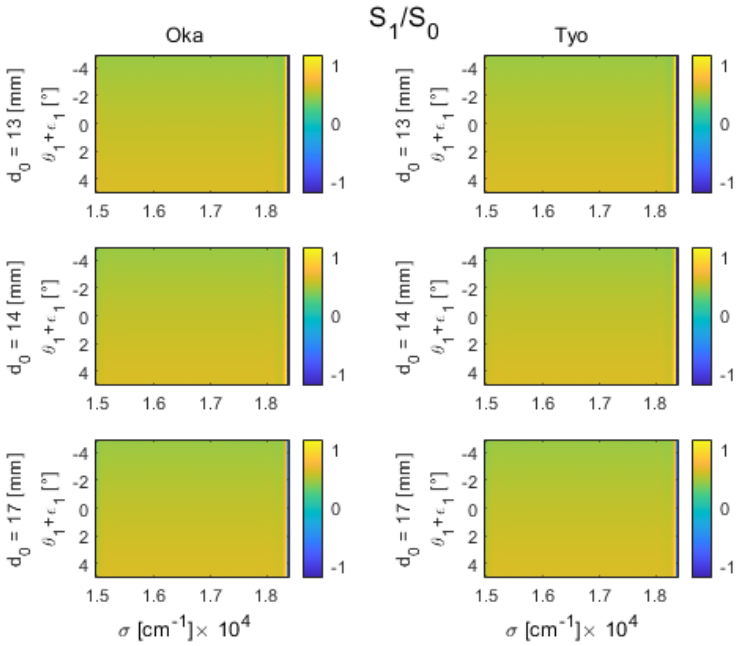

Figure 3.18: Normalized Stokes parameter S_1/S_0 against alignment error ϵ_1. The Channel Splitting and the Analytical Channel Splitting methods are labeled as Oka and Tyo, respectively.

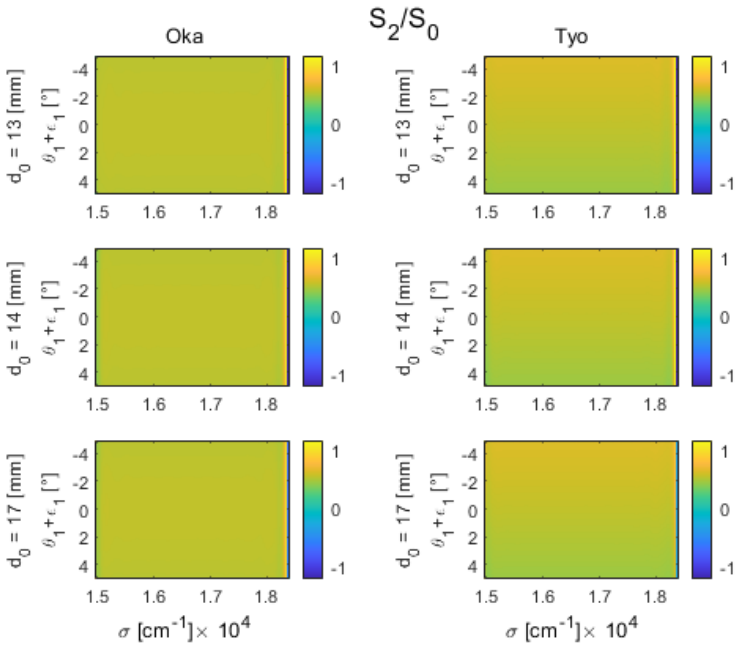

Figure 3.19: Normalized Stokes parameter S_2/S_0 against alignment error ϵ_1. The Channel Splitting and the Analytical Channel Splitting methods are labeled as Oka and Tyo, respectively.

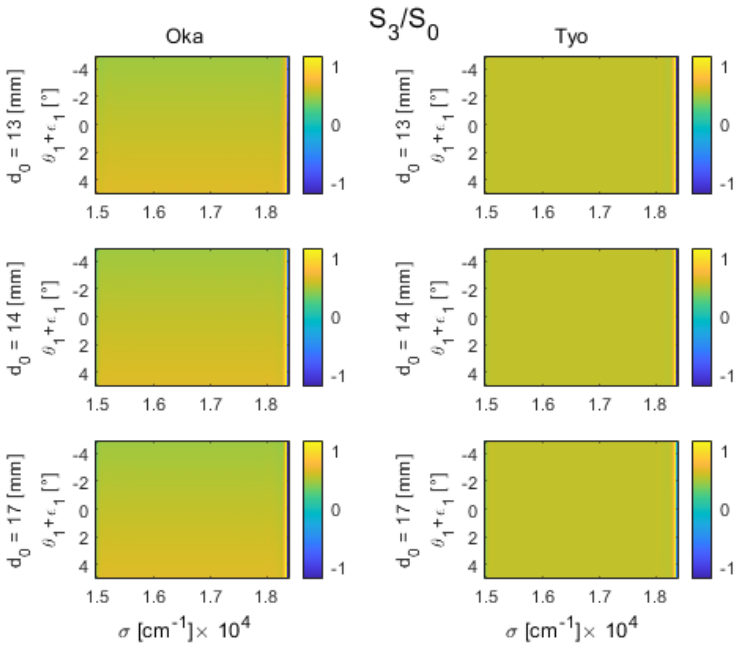

Figure 3.20: Normalized Stokes parameter S_3/S_0 against alignment error ϵ_1. The Channel Splitting and the Analytical Channel Splitting methods are labeled as Oka and Tyo, respectively.

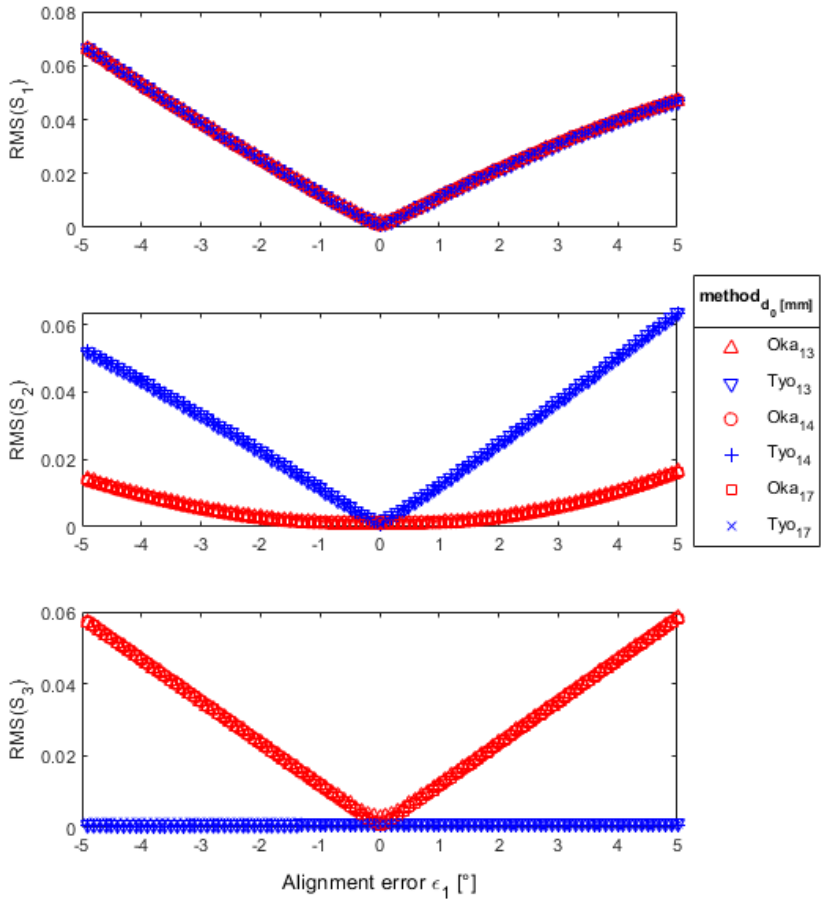

Figure 3.21: $RMS(S_i)$ against alignment error ϵ_1, for $i = 1, 2, 3$. The Channel Splitting and the Analytical Channel Splitting methods are labeled as Oka and Tyo, respectively.

In Fig. 3.22, 3.23, and 3.24 are shown the normalized Stokes parameters S_1/S_0, S_2/S_0, and S_3/S_0, respectively, when the alignment error occurs in the second retarder. It is observed that S_1 is immune to the error source. When the Analytical Channel Splitting method is used, S_2 and S_3 are immune as well. The $RMS(S_i)$ plots are shown in Fig. 3.25.

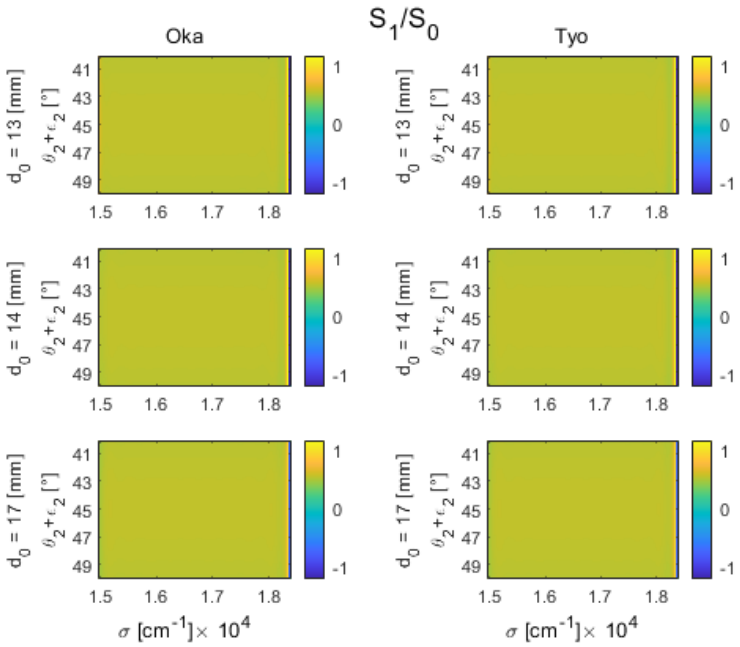

Figure 3.22: Normalized Stokes parameter S_1/S_0 against alignment error ϵ_2. The Channel Splitting and the Analytical Channel Splitting methods are labeled as Oka and Tyo, respectively.

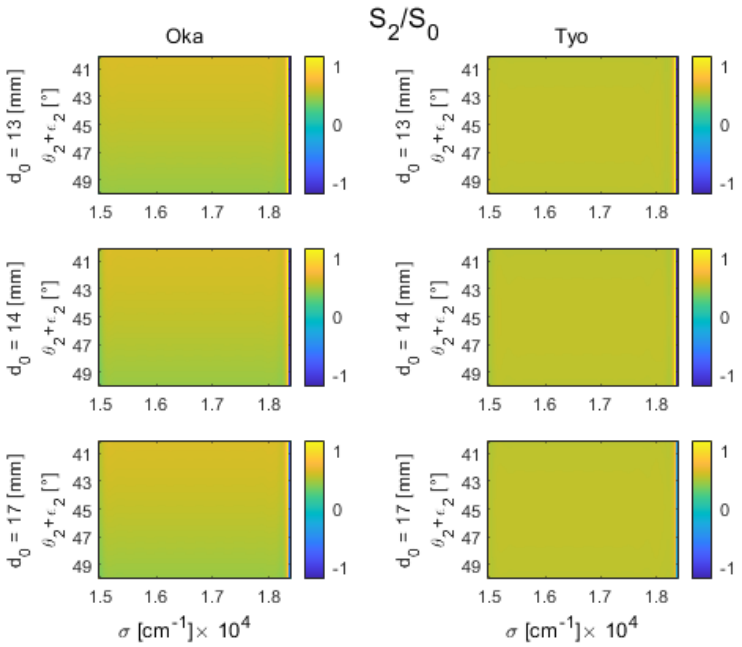

Figure 3.23: Normalized Stokes parameter S_2/S_0 against alignment error ϵ_2. The Channel Splitting and the Analytical Channel Splitting methods are labeled as Oka and Tyo, respectively.

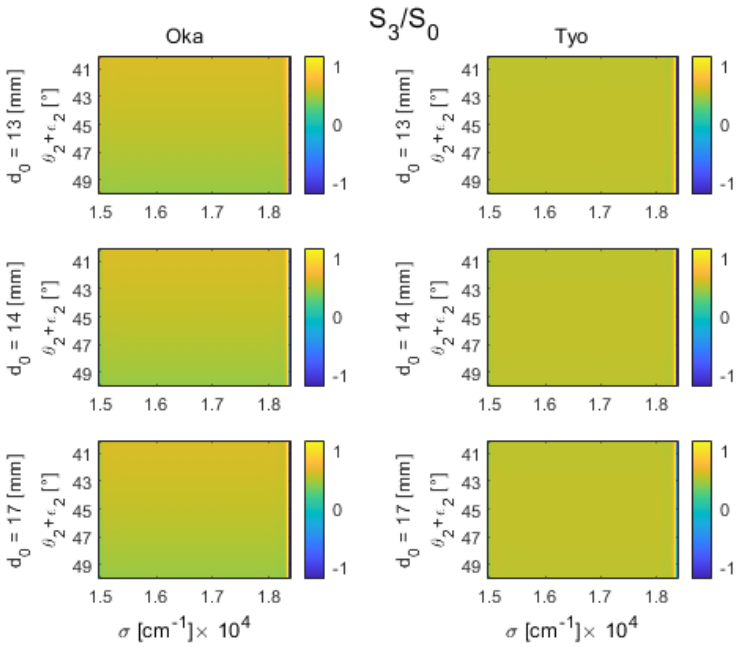

Figure 3.24: Normalized Stokes parameter S_3/S_0 against alignment error ϵ_2. The Channel Splitting and the Analytical Channel Splitting methods are labeled as Oka and Tyo, respectively.

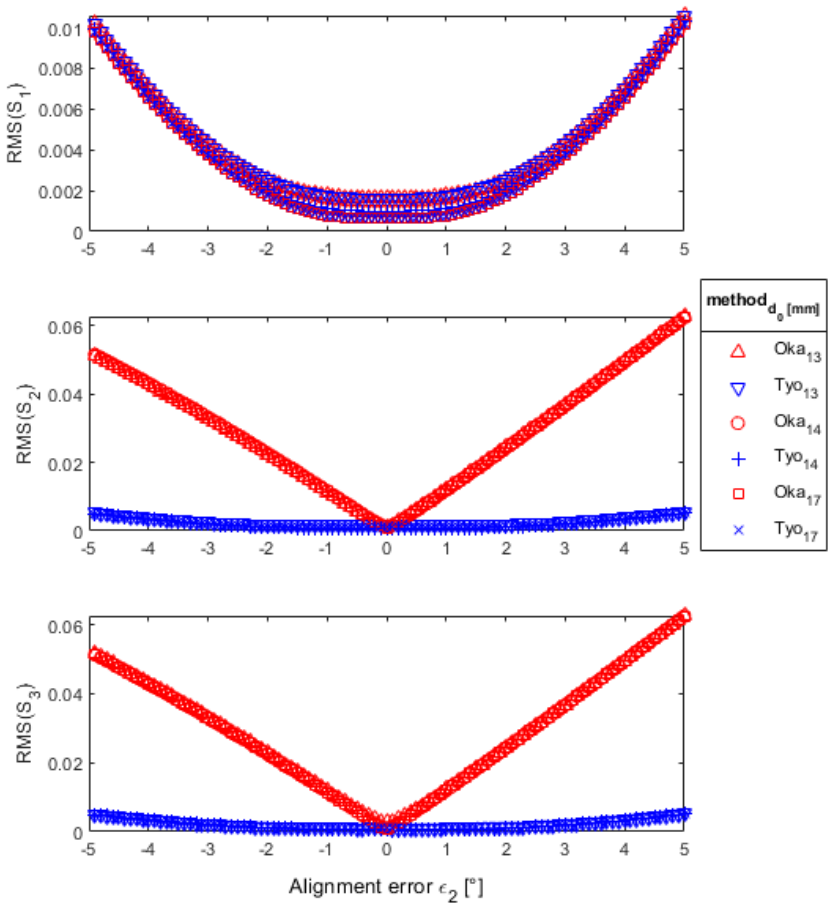

Figure 3.25: $RMS(S_i)$ against alignment error ϵ_2, for $i = 1, 2, 3$. The Channel Splitting and the Analytical Channel Splitting methods are labeled as Oka and Tyo, respectively.

3.5.5 Gaussian noise

A random Gaussian noise distribution was added to the spectrum leaving the SCS before entering the spectrometer. The amplitudes considered ranged from $1E-6[a.u]$ to $1E1[a.u]$, including a reference without noise. In Fig. 3.26, 3.27, and 3.28 are shown the normalized Stokes parameters S_1/S_0, S_2/S_0, and S_3/S_0, respectively. It is observed that a signal-to-noise ratio (SNR) of $10:1$ is acceptable, but immunity is achieved for SNR greater or equal to $100:1$, see the $RMS(S_i)$ plots in Fig. 3.29. This SNR requirement is achievable with commercially available spectrometers.

In Fig. 3.30 are shown the effects of the Gaussian noise on the autocorrelation function $|C(\tau)|$, and in Fig. 3.31 are shown the detected peaks and valleys, which are crucial for the channels detection algorithm.

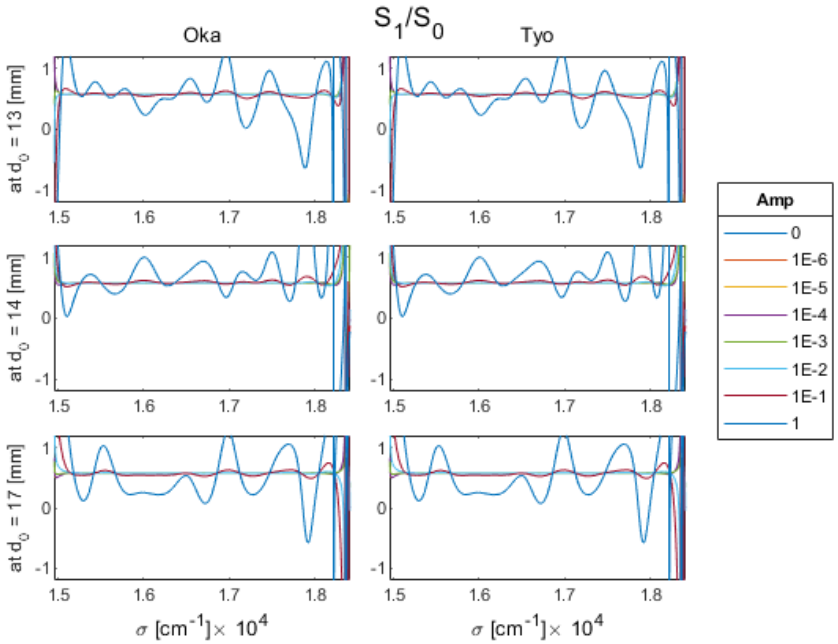

Figure 3.26: Normalized Stokes parameter S_1/S_0 against the Gaussian noise distribution amplitude. The Channel Splitting and the Analytical Channel Splitting methods are labeled as Oka and Tyo, respectively.

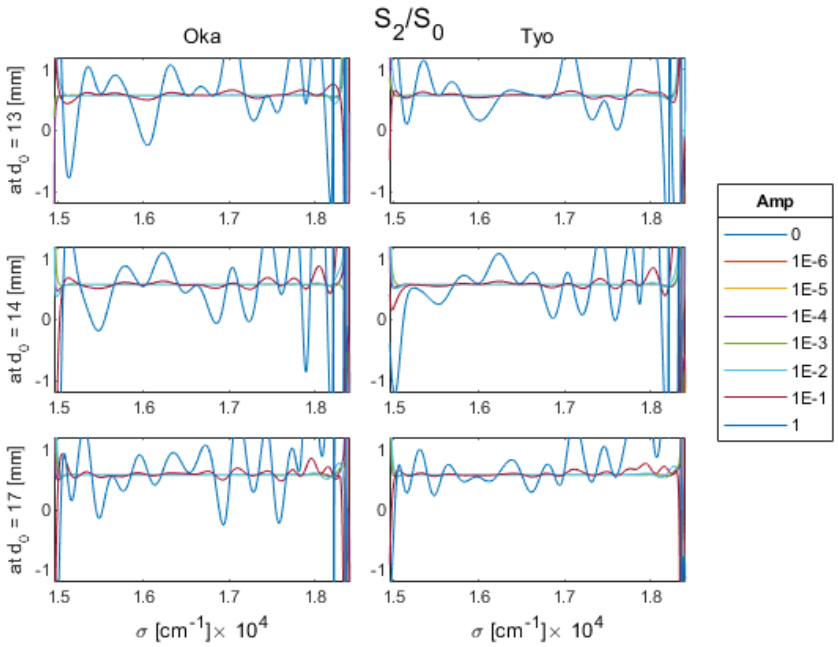

Figure 3.27: Normalized Stokes parameter S_2/S_0 against the Gaussian noise distribution amplitude. The Channel Splitting and the Analytical Channel Splitting methods are labeled as Oka and Tyo, respectively.

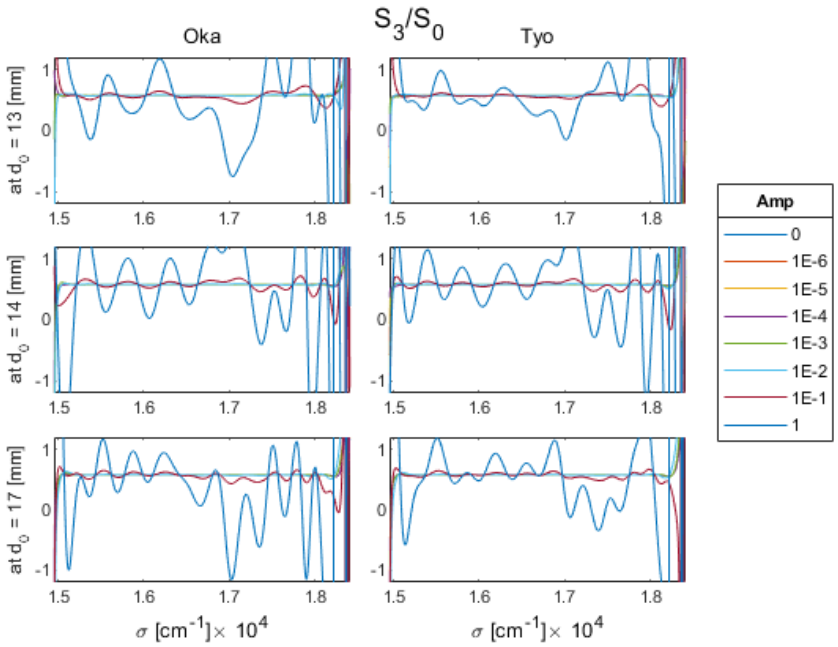

Figure 3.28: Normalized Stokes parameter S_3/S_0 against the Gaussian noise distribution amplitude. The Channel Splitting and the Analytical Channel Splitting methods are labeled as Oka and Tyo, respectively.

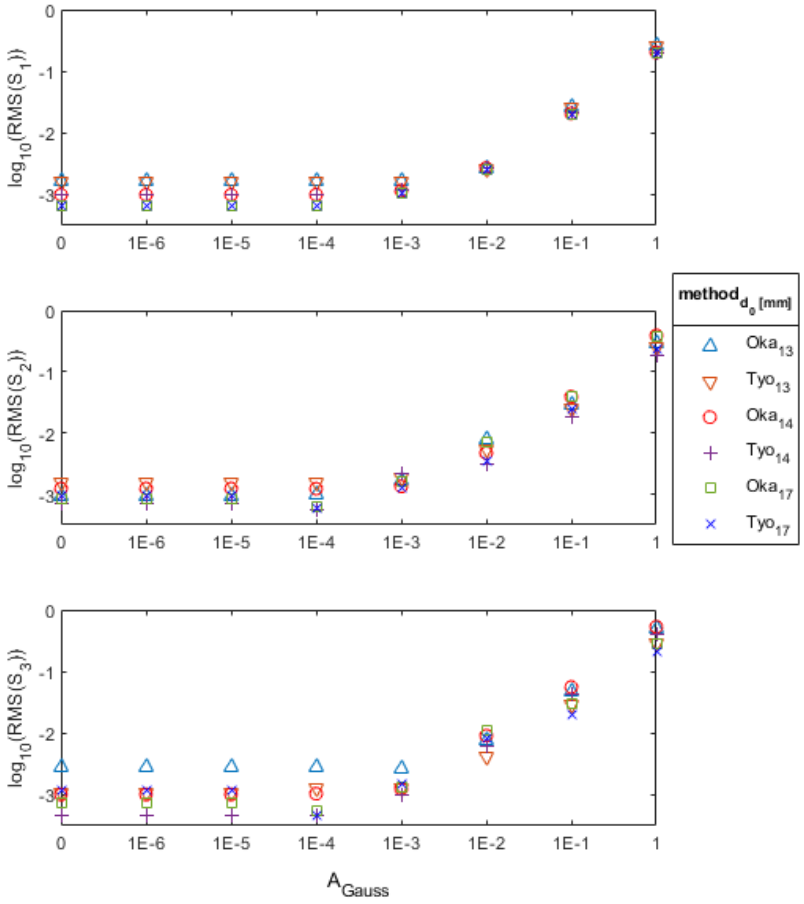

Figure 3.29: $log_{10}(RMS(S_i))$ against the Gaussian noise distribution amplitude, for $i = 1, 2, 3$. The Channel Splitting and the Analytical Channel Splitting methods are labeled as Oka and Tyo, respectively.

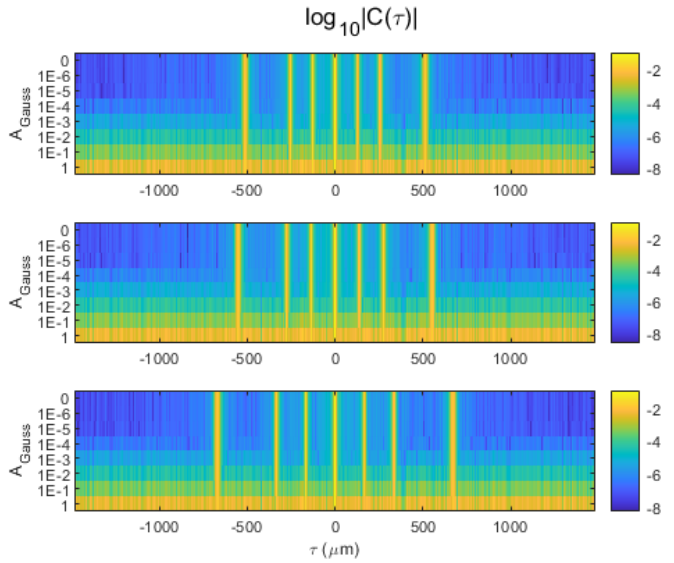

Figure 3.30: Autocorrelation function $|C(\tau)|$ against the Gaussian noise distribution amplitude.

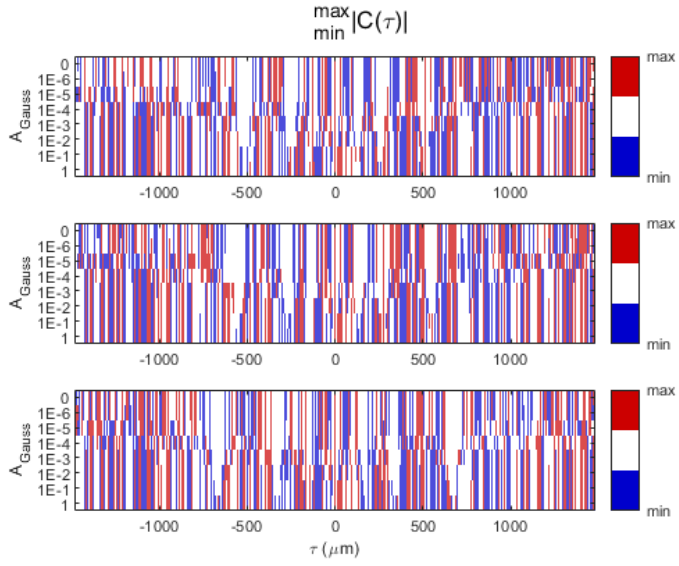

Figure 3.31: Autocorrelation function $\frac{max}{min}|C(\tau)|$ against the Gaussian noise distribution amplitude.

Notes on the analysis of two or more simultaneous error sources

The SCS was also simulated under the influence of two sources of error: thickness error Δd_1 and additive Gaussian noise. The values considered are the same as reported in the previous sections. In Fig. 3.32, 3.33, and 3.34 are shown the normalized Stokes parameters S_1/S_0, S_2/S_0, and S_3/S_0, respectively. The Gaussian noise amplitude is represented in eight main rows and the thickness error in 100 subrows per main row.

In Fig. 3.32, it is observed that S_1 is immune to thickness error Δd_1 and most of the Gaussian noise amplitudes, except for $A_{Gauss} \gtrsim 1E-1$. The parameters S_2 and S_3 are highly sensitive to Δd_1, and to the Gaussian noise amplitude $A_{Gauss} \gtrsim 1E-1$. This is better observed in the RMS plots in Fig. 3.35, 3.36, and 3.37. This agrees with the results from the previous sections.

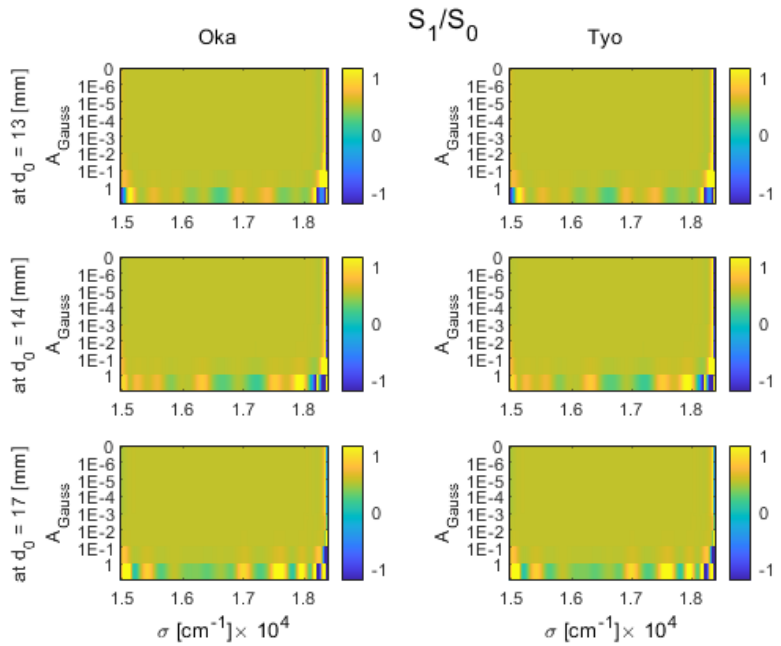

Figure 3.32: Normalized Stokes parameter S_1/S_0 against the Gaussian noise distribution amplitude (8 main rows) and the thickness error Δd_1 (100 subrows per main row). The Channel Splitting and the Analytical Channel Splitting methods are labeled as Oka and Tyo, respectively.

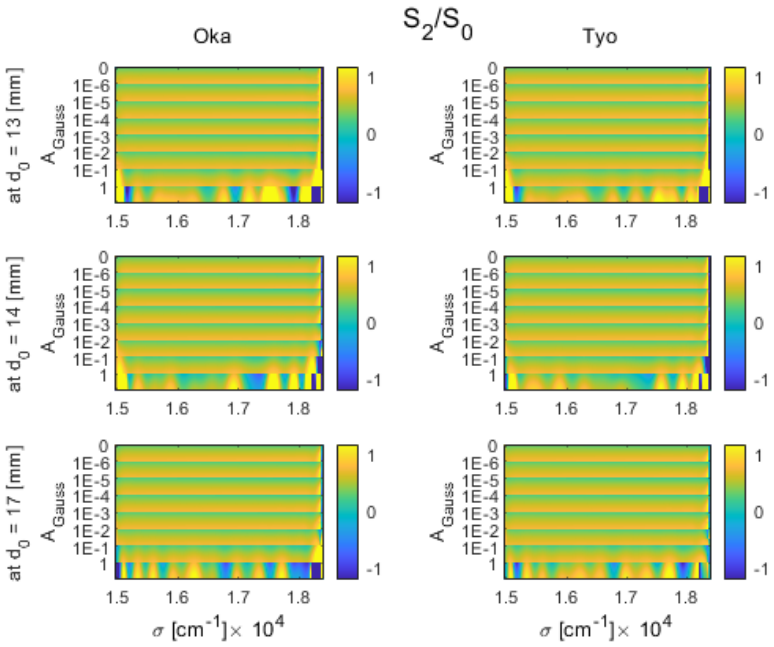

Figure 3.33: Normalized Stokes parameter S_2/S_0 against the Gaussian noise distribution amplitude (8 main rows) and the thickness error Δd_1 (100 sub-rows per main row). The Channel Splitting and the Analytical Channel Splitting methods are labeled as Oka and Tyo, respectively.

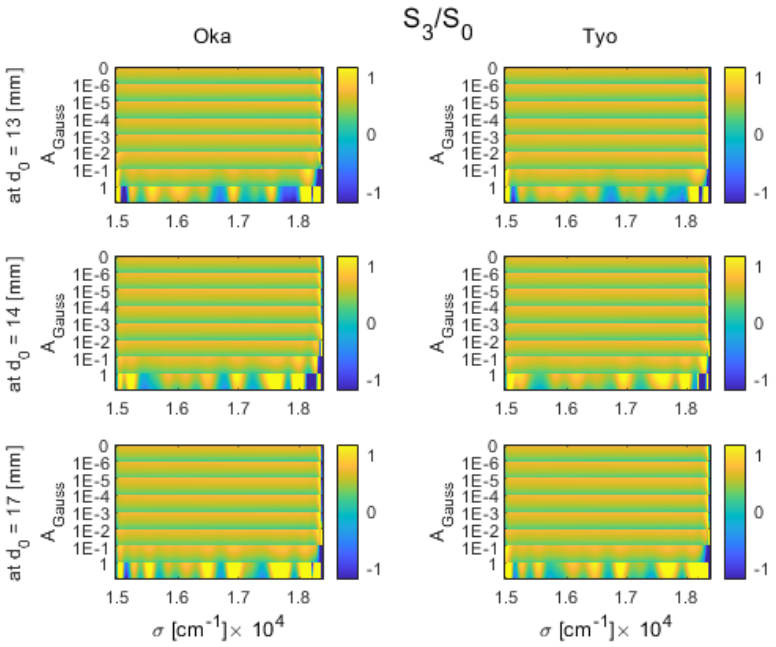

Figure 3.34: Normalized Stokes parameter S_3/S_0 against the Gaussian noise distribution amplitude (8 main rows) and the thickness error Δd_1 (100 sub-rows per main row). The Channel Splitting and the Analytical Channel Splitting methods are labeled as Oka and Tyo, respectively.

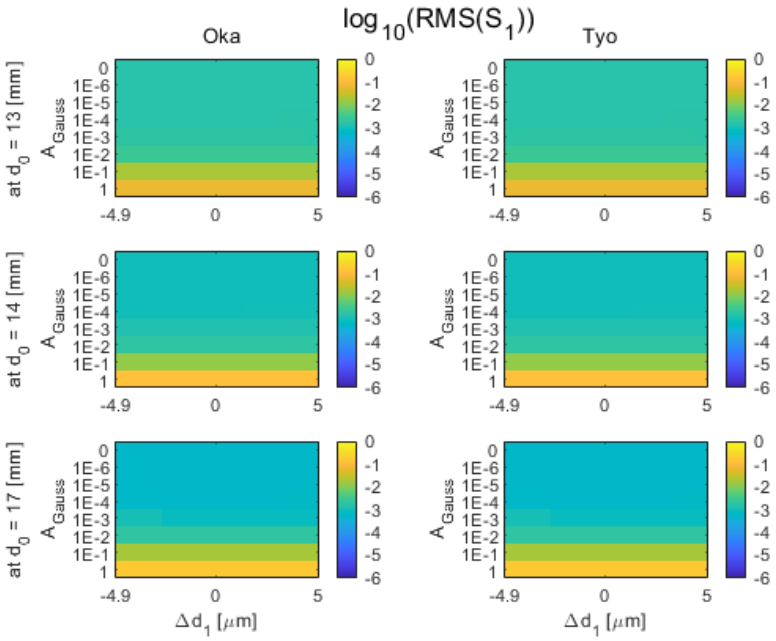

Figure 3.35: $log_{10}(RMS(S_1))$ against the Gaussian noise distribution amplitude (8 main rows) and the thickness error Δd_1 (100 subrows per main row). The Channel Splitting and the Analytical Channel Splitting methods are labeled as Oka and Tyo, respectively.

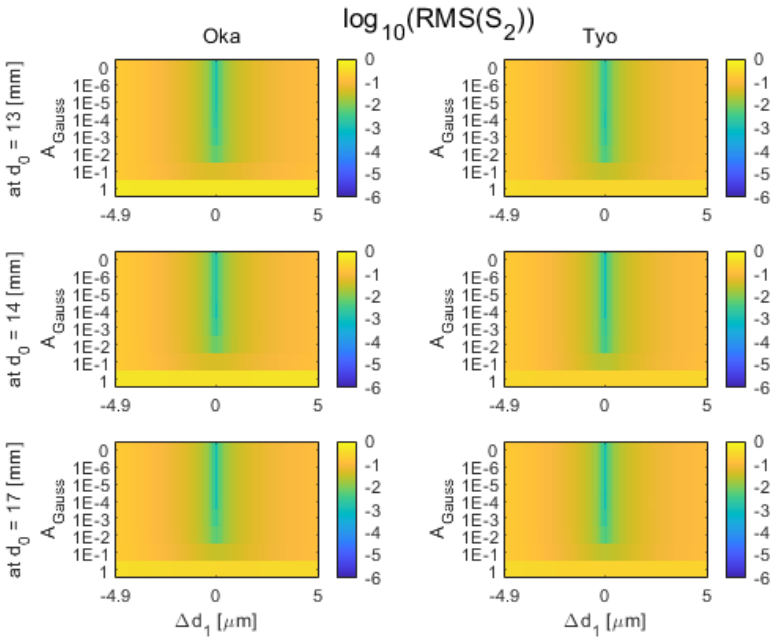

Figure 3.36: $log_{10}(RMS(S_2))$ against the Gaussian noise distribution amplitude (8 main rows) and the thickness error Δd_1 (100 subrows per main row). The Channel Splitting and the Analytical Channel Splitting methods are labeled as Oka and Tyo, respectively.

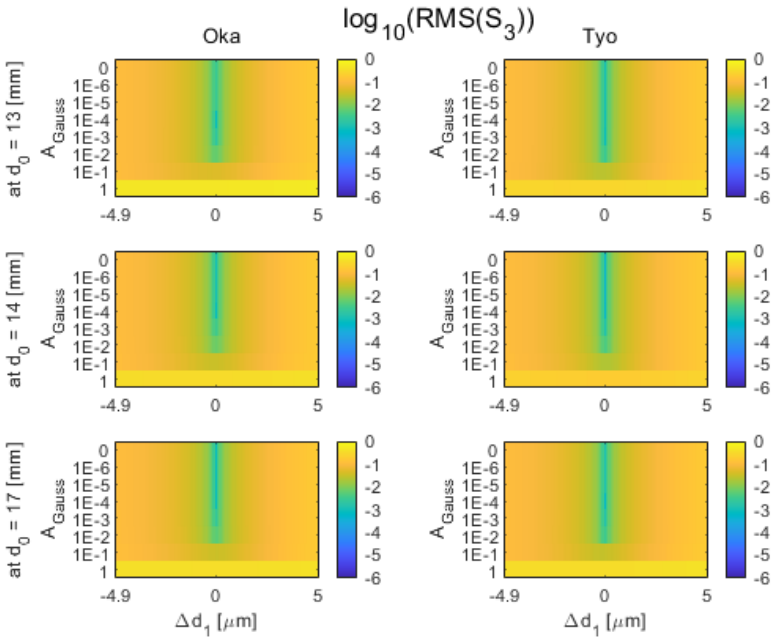

Figure 3.37: $log_{10}(RMS(S_3))$ against the Gaussian noise distribution amplitude (8 main rows) and the thickness error Δd_1 (100 subrows per main row). The Channel Splitting and the Analytical Channel Splitting methods are labeled as Oka and Tyo, respectively.

3.6 MMCS simulation, results and discussion

For the MMCS simulations reported, a value of $N = 2048$ pixels was considered to achieve a good distribution of channels in the τ-domain. In the simulation, the system was illuminated with a Tungsten Halogen light source [35]. The sample selected for the results reported is air (considered invariant with wavelength).

3.6.1 Thickness ratio

Six thickness ratios were considered: (1,2,3,5), (1,2,4,8), (1,2,5,10), (1,4,2,9), (2,1,4,11), and (2,1,5,12), with a global retardance factor $d_0 = 10[mm]$. In Fig. 3.38 is shown the autocorrelation function $|C(\tau)|$. It is observed that the channels occupy a wider bandwidth, compared to the SCS configurations.

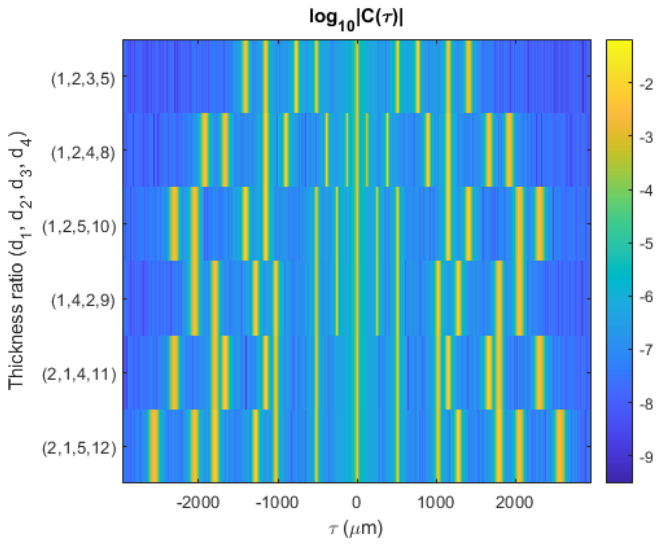

Figure 3.38: Autocorrelation function $|C(\tau)|$ for the MMCS with different thickness ratios and a global retardance factor $d_0 = 10[mm]$.

In Fig. 3.39 are shown the EWV and CN plots for the thickness ratios of interest. The configurations $(1, 4, 2, 9)$, $(2, 1, 4, 11)$, and $(2, 1, 5, 12)$ have the lowest EWV and CN values. In Fig. 3.40 are shown the normalized Mueller matrix elements (m_{ij}/m_{00}) for air and the RMS-values for the extracted Mueller matrix M and its elements m_{ij} are shown in Table. 3.1.

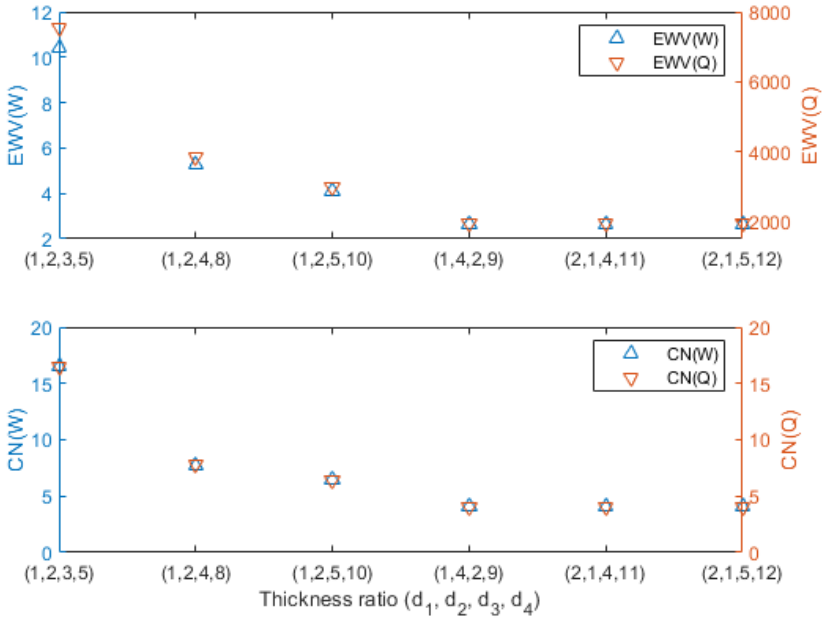

Figure 3.39: EWV and CN of the W- and Q-matrix for the MMCS configurations $(1, 2, 3, 5)$, $(1, 2, 4, 8)$, $(1, 2, 5, 10)$, $(1, 4, 2, 9)$, $(2, 1, 4, 11)$, and $(2, 1, 5, 12)$.

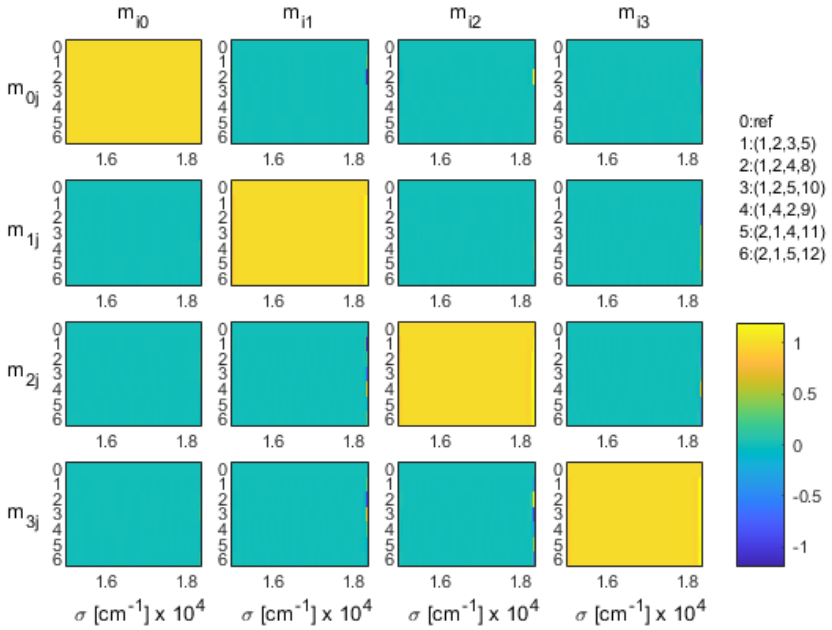

Figure 3.40: Normalized Mueller matrix elements (m_{ij}/m_{00}) of the sample (air) for the MMCS configurations $(1, 2, 3, 5)$, $(1, 2, 4, 8)$, $(1, 2, 5, 10)$, $(1, 4, 2, 9)$, $(2, 1, 4, 11)$, and $(2, 1, 5, 12)$.

Table 3.1: RMS of extracted Mueller matrix $\mathbf{M}$ and its elements m_{ij} (air sample) using different thickness ratio configurations.

	Configuration (thickness ratio)					
	$(1,2,3,5)$	$(1,2,4,8)$	$(1,2,5,10)$	$(1,4,2,9)$	$(2,1,4,11)$	$(2,1,5,12)$
$\mathbf{M}$	3.63E-03	4.46E-03	3.03E-03	3.05E-03	3.02E-03	2.96E-03
m_{00}	7.45E-03	7.47E-03	7.45E-03	7.45E-03	7.45E-03	7.45E-03
m_{01}	1.45E-03	2.30E-03	2.01E-04	1.22E-04	4.32E-05	5.38E-05
m_{02}	3.65E-04	4.42E-03	2.10E-04	1.62E-04	1.18E-04	3.32E-04
m_{03}	1.38E-03	4.84E-03	1.98E-04	2.05E-04	4.37E-04	4.28E-04
m_{10}	1.56E-04	2.87E-04	4.49E-04	2.53E-04	3.05E-05	2.70E-05
m_{11}	1.23E-03	3.09E-03	1.22E-03	1.29E-03	4.73E-03	3.05E-03
m_{12}	9.37E-05	1.16E-04	3.66E-05	9.13E-04	1.85E-03	2.27E-04
m_{13}	3.48E-03	3.65E-03	3.34E-03	2.90E-03	3.59E-03	3.64E-04
m_{20}	8.39E-05	3.48E-04	3.30E-04	1.14E-04	1.17E-04	2.89E-04
m_{21}	5.76E-03	5.08E-03	2.32E-03	3.61E-03	1.99E-03	2.60E-04
m_{22}	8.65E-03	7.85E-03	3.24E-03	5.34E-03	2.95E-03	1.76E-03
m_{23}	2.54E-03	1.95E-03	2.23E-03	3.91E-03	2.97E-03	6.33E-03
m_{30}	5.17E-05	8.45E-05	1.35E-04	3.62E-04	1.02E-04	4.28E-04
m_{31}	2.57E-03	4.82E-03	4.48E-03	3.12E-03	3.44E-03	2.61E-04
m_{32}	2.50E-03	8.42E-03	5.92E-03	3.08E-03	3.02E-03	4.35E-03
m_{33}	3.15E-03	2.50E-03	1.54E-03	2.49E-03	2.99E-03	3.53E-03

3.6.2 Global retardance factor

The MMCS configuration $(1, 2, 5, 10)$ was used from this test forward, as it has been studied before [2, 22]. Inspired by the dual-rotating-retarder Mueller matrix polarimeter [3], Hagen *et al.* chose a $5:1$ ratio of thickness for the pair of analysing retarders to the generating pair to give a compact result. Furthermore, Hagen *et al.* selected a $2:1$ ratio of thicknesses for the retarders within each pair giving a set of thicknesses designated as a $(1, 2, 5, 10)$ configuration [22].

In Fig. 3.41 are shown the normalized Mueller matrix elements (m_{ij}/m_{00}) using a global retardance factor $d_0 = 1 - 10[mm]$. It is observed that many artifacts arise when $d_0 < 5[mm]$. Because of this, the global retardance factor range was increased to $d_0 = 5 - 14[mm]$. The extracted Mueller matrix for this range is shown in Fig. 3.42.

From the RMS-values (see Table 3.2), it is observed that the MMCS performance generally improves when the global retardance factor is increased. Although, the availability in the market of bigger thick birefringent retarders must be considered. The lowest $EWV(\underline{\underline{\mathbf{W}}})$ is obtained with $d_0 = 14[mm]$ and the lowest $CN(\underline{\underline{\mathbf{W}}})$, with $d_0 = 8[mm]$ (see Fig. 3.43).

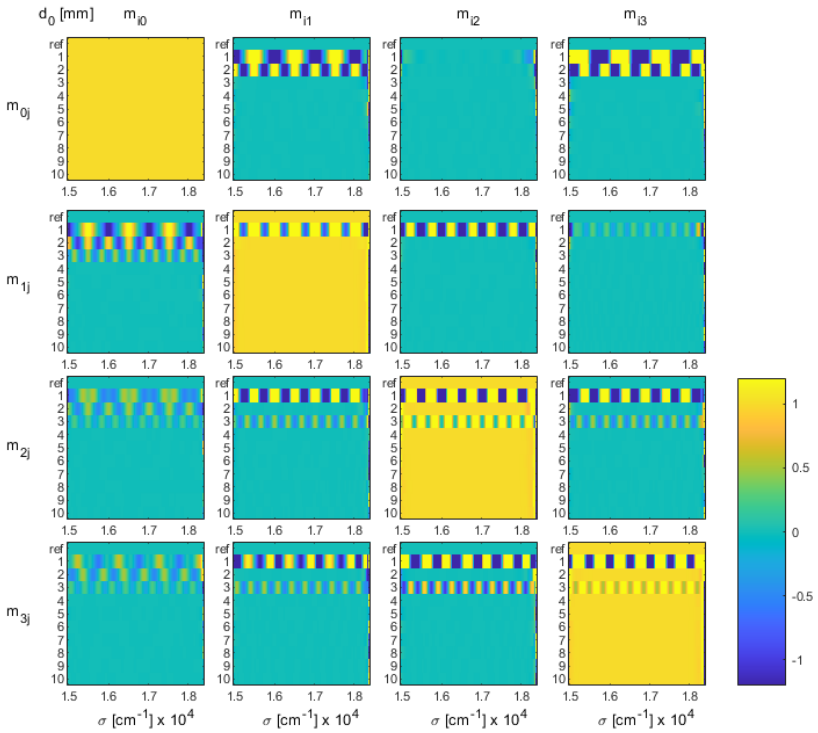

Figure 3.41: Normalized Mueller matrix elements (m_{ij}/m_{00}) of the sample (air) with a configuration $(1, 2, 5, 10)$ and $d_0 = 1 - 10[mm]$.

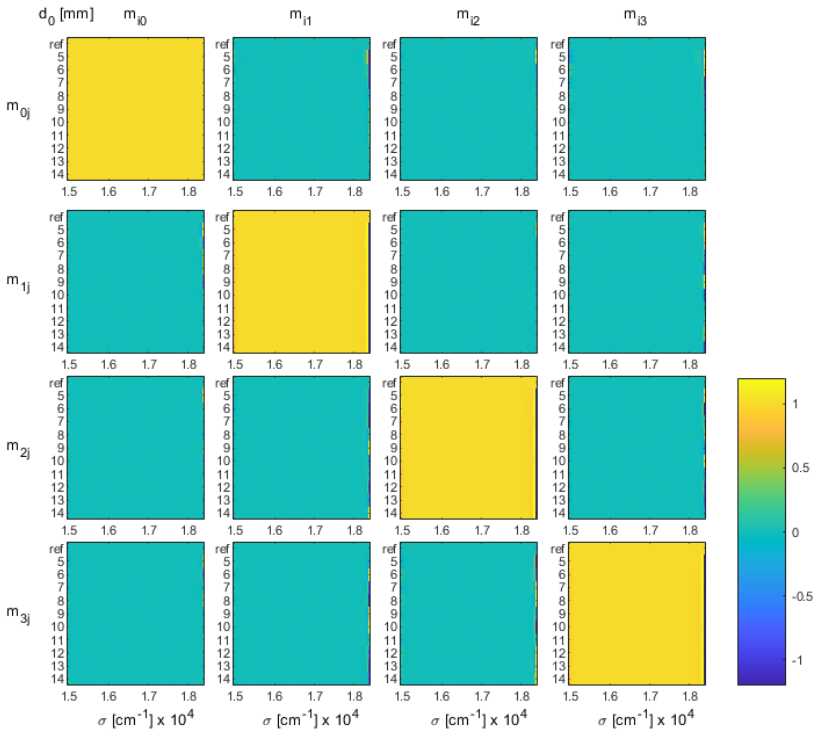

Figure 3.42: Normalized Mueller matrix elements (m_{ij}/m_{00}) of the sample (air) with a configuration $(1, 2, 5, 10)$ and $d_0 = 5 - 14[mm]$.

Table 3.2: RMS of extracted Mueller matrix $\mathbf{M}$ and its elements m_{ij} (air sample) for different global retardance factors.

	Global retardance factor $d_0[mm]$									
	5	6	7	8	9	10	11	12	13	14
M	6.11E-03	4.44E-03	3.73E-03	3.53E-03	3.12E-03	3.14E-03	2.47E-03	2.79E-03	3.03E-03	2.78E-03
m_{00}	7.42E-03	7.38E-03	7.40E-03	7.42E-03	7.43E-03	7.45E-03	7.45E-03	7.45E-03	7.45E-03	7.46E-03
m_{01}	1.61E-02	4.57E-03	2.30E-03	2.76E-03	1.77E-03	5.20E-04	9.88E-04	2.61E-04	2.01E-04	3.77E-04
m_{02}	2.53E-03	2.83E-03	3.21E-04	1.66E-03	1.78E-04	6.65E-04	1.60E-04	2.32E-04	2.10E-04	2.05E-04
m_{03}	1.15E-02	2.70E-03	3.91E-03	1.07E-03	5.58E-04	4.39E-04	1.17E-03	1.84E-04	1.98E-04	1.61E-04
m_{10}	5.39E-03	5.22E-03	1.37E-03	7.55E-04	6.06E-04	7.34E-04	3.63E-04	1.87E-04	4.49E-04	1.24E-04
m_{11}	1.83E-03	8.29E-03	2.32E-03	1.19E-03	2.22E-03	4.00E-03	2.29E-03	3.88E-03	1.22E-03	1.70E-03
m_{12}	1.23E-03	1.73E-04	3.16E-04	8.90E-05	9.86E-05	1.59E-04	5.24E-05	8.53E-05	3.66E-05	3.91E-05
m_{13}	4.44E-03	1.45E-03	3.67E-03	3.09E-03	1.74E-03	1.79E-03	6.91E-04	2.33E-03	3.34E-03	2.97E-03
m_{20}	1.46E-03	5.23E-04	1.15E-03	9.41E-04	3.79E-04	7.54E-04	5.10E-04	2.72E-04	3.30E-04	6.50E-05
m_{21}	3.44E-03	1.33E-03	2.90E-03	3.81E-03	1.84E-03	2.68E-03	1.99E-03	3.05E-03	2.32E-03	3.57E-03
m_{22}	6.05E-03	2.60E-03	5.11E-03	5.56E-03	5.75E-03	5.45E-03	1.77E-03	3.65E-03	3.24E-03	5.21E-03
m_{23}	2.47E-03	2.15E-03	2.18E-03	1.30E-03	3.14E-03	3.00E-03	2.67E-03	1.44E-03	2.23E-03	1.88E-03
m_{30}	1.68E-03	1.13E-03	1.89E-03	7.69E-04	4.78E-04	1.94E-04	4.27E-04	3.99E-04	1.35E-04	6.46E-05
m_{31}	1.49E-03	2.63E-03	4.47E-03	3.87E-03	2.60E-03	2.13E-03	7.32E-04	2.99E-03	4.48E-03	2.03E-03
m_{32}	3.11E-03	9.39E-03	6.81E-03	7.32E-03	4.27E-03	4.51E-03	2.28E-03	3.40E-03	5.92E-03	1.85E-03
m_{33}	4.34E-03	4.10E-03	3.89E-03	1.95E-03	4.10E-03	3.19E-03	3.69E-03	1.75E-03	1.54E-03	2.34E-03

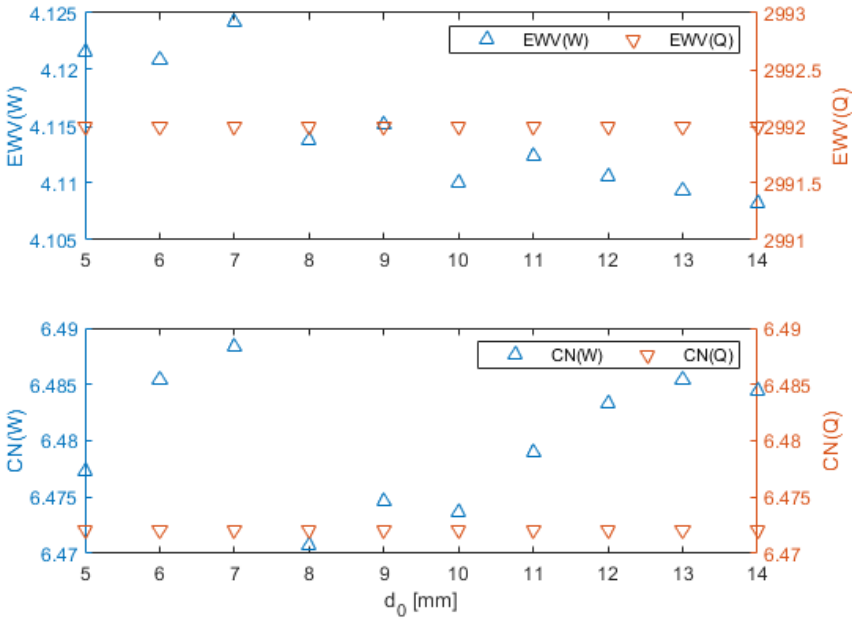

Figure 3.43: EWV and CN of the W- and Q-matrix against the global retardance factor d_0.

3.6.3 Retardance error

The same fabrication tolerance of $\pm 5[\mu m]$ was considered. In Fig. 3.44 is shown the extracted Mueller matrix, considering the thickness error Δd_1 of the first retarder. The elements $m_{11}, m_{13}, m_{22}, m_{31}, m_{32}, m_{33}$ are sensitive to this error; m_{01} is considered not-immune, but acceptably extracted; and the rest of the elements are immune.

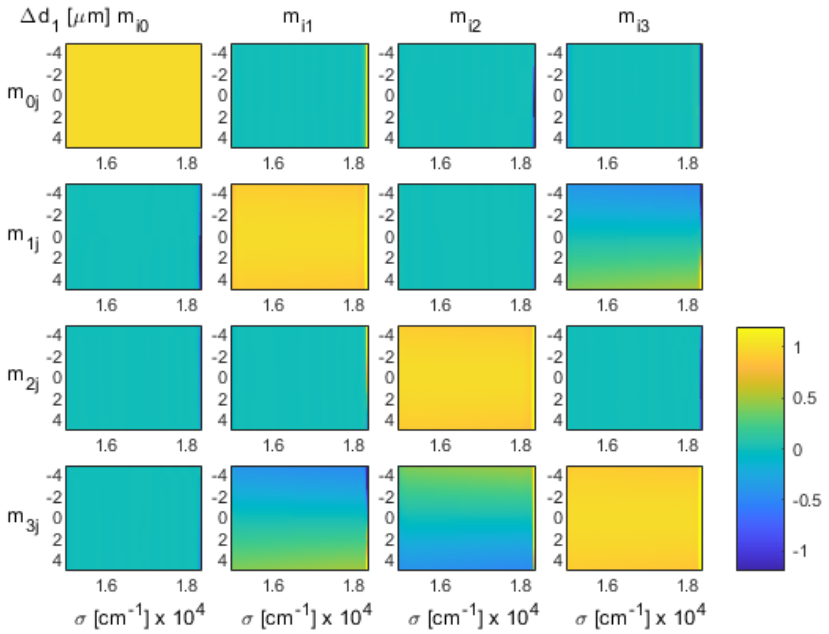

Figure 3.44: Normalized Mueller matrix elements (m_{ij}/m_{00}) of the sample (air) with a configuration $(1, 2, 5, 10)$ against thickness error Δd_1.

In Fig. 3.45 is shown the extracted Mueller matrix, considering the thickness error Δd_2 of the second retarder. The elements $m_{22}, m_{23}, m_{32}, m_{33}$ are sensitive to Δd_2; m_{01}, m_{03} are not-immune, but acceptably extracted; and the rest of the elements are immune.

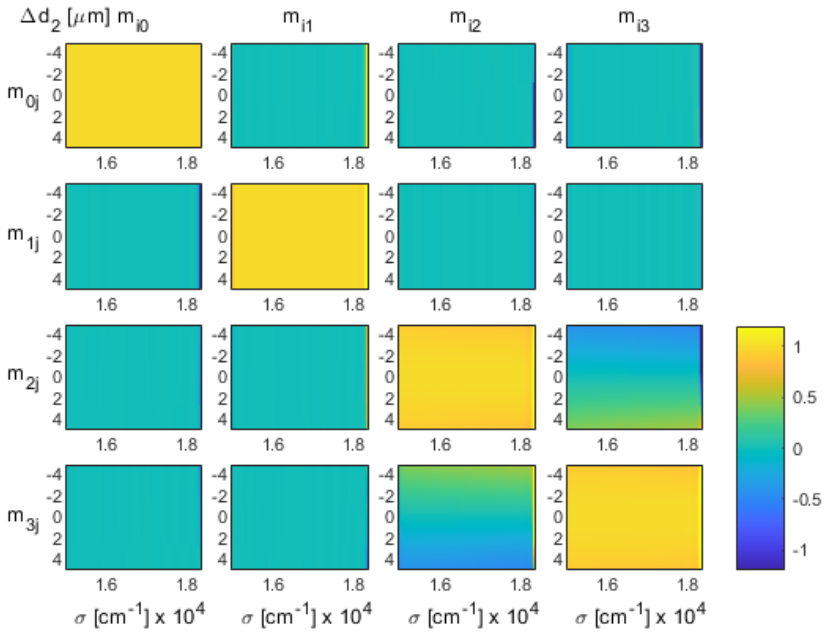

Figure 3.45: Normalized Mueller matrix elements (m_{ij}/m_{00}) of the sample (air) with a configuration $(1, 2, 5, 10)$ against thickness error Δd_2.

In Fig. 3.46 is shown the extracted Mueller matrix, considering the thickness error Δd_3 of the third retarder. Most of the matrix elements are immune to the fabrication error in the third retarder. The elements $m_{22}, m_{23}, m_{32}, m_{33}$ are sensitive to this error; m_{01}, m_{03} are not-immune, but acceptably extracted.

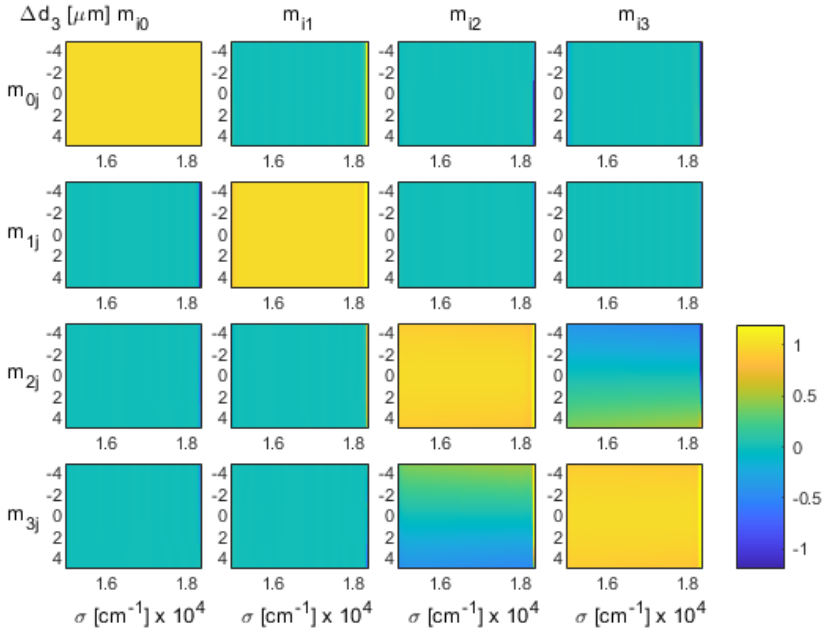

Figure 3.46: Normalized Mueller matrix elements (m_{ij}/m_{00}) of the sample (air) with a configuration $(1, 2, 5, 10)$ against thickness error Δd_3.

In Fig. 3.47 is shown the extracted Mueller matrix, considering the thickness error Δd_4 from the fourth retarder. Most of the matrix elements are immune to Δd_4. The elements m_{11}, m_{22}, m_{33} are sensitive to the error source; m_{01}, m_{03}, m_{33} are not-immune, but acceptably extracted.

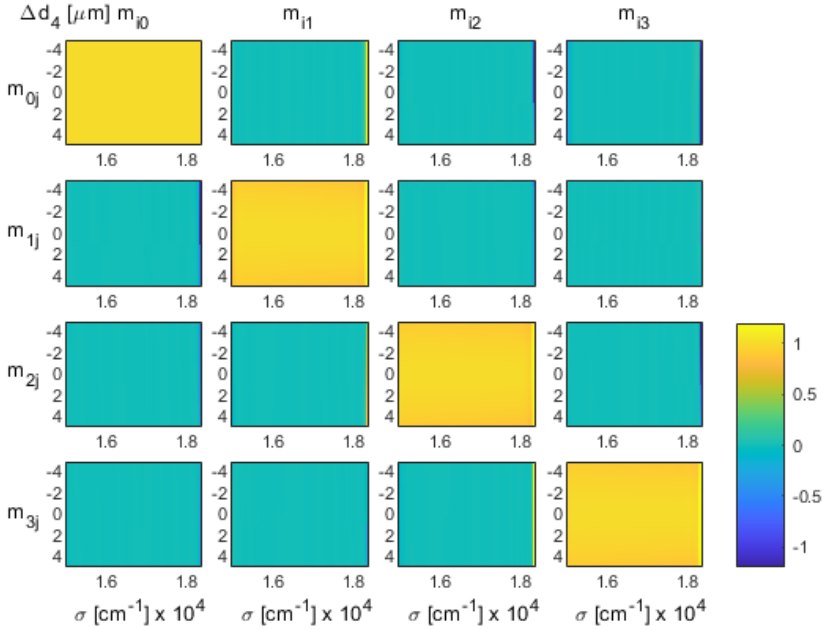

Figure 3.47: Normalized Mueller matrix elements (m_{ij}/m_{00}) of the sample (air) with a configuration $(1, 2, 5, 10)$ against thickness error Δd_4.

In Fig. 3.48 are shown the RMS plots for the extracted Mueller matrix, considering the thickness error from the four retarders. It is observed that the extraction process is sensitive to the thickness error of the first, second and third retarders; it is at least four times less sensitive to the thickness error of the fourth retarder, and immunity is achieved within a fabrication tolerance of $\pm 2[\mu m]$ for the fourth retarder.

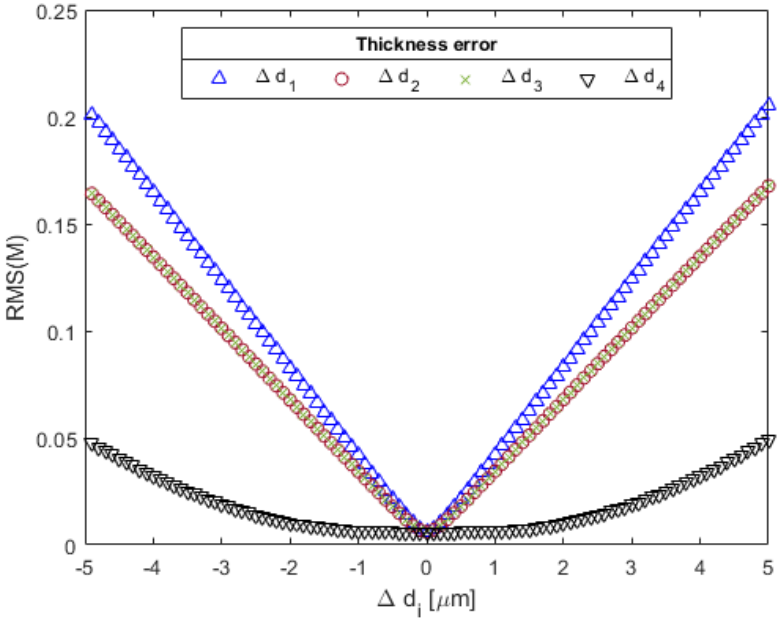

Figure 3.48: $RMS(M)$ against the thickness error Δd_i, for $i = 1, 2, 3, 4$.

3.6.4 Alignment error

The same alignment tolerance was considered for the optical elements. In Fig. 3.49 is shown the extracted Mueller matrix, considering the alignment error ϵ_1 from the first retarder. Most of the matrix elements are immune to the alignment error in the first retarder. The elements $m_{01}, m_{02}, m_{21}, m_{22}$ are sensitive to the error source; $m_{03}, m_{10}, m_{11}, m_{23}, m_{31}, m_{32}, m_{33}$ are acceptably extracted, if not immune.

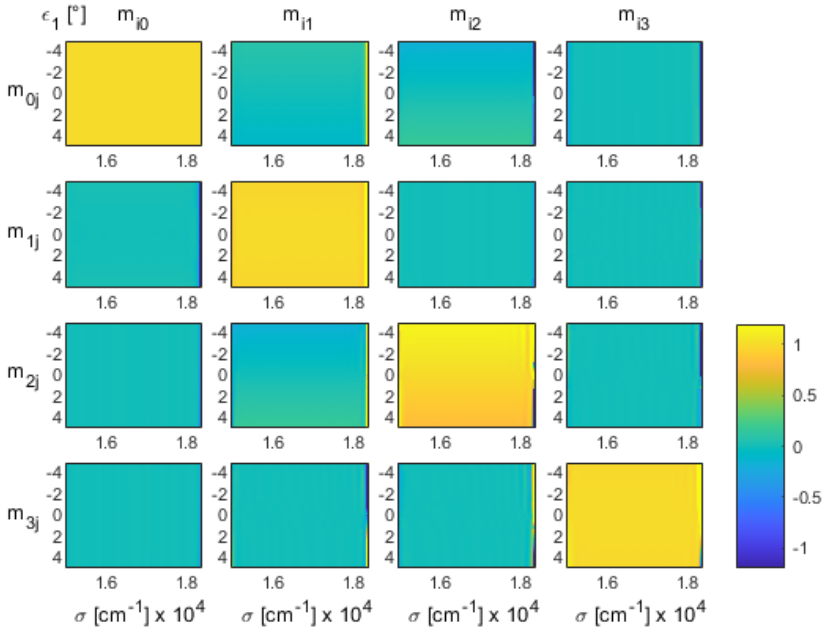

Figure 3.49: Normalized Mueller matrix elements (m_{ij}/m_{00}) of the sample (air) with a configuration $(1, 2, 5, 10)$ against the alignment error ϵ_1.

In Fig. 3.50 is shown the extracted Mueller matrix, considering the alignment error ϵ_2 from the second retarder. Most of the matrix elements are immune to ϵ_2, but m_{12}, m_{22} are sensitive to the error source. Furthermore, m_{01}, m_{03} are not-immune, but acceptably extracted.

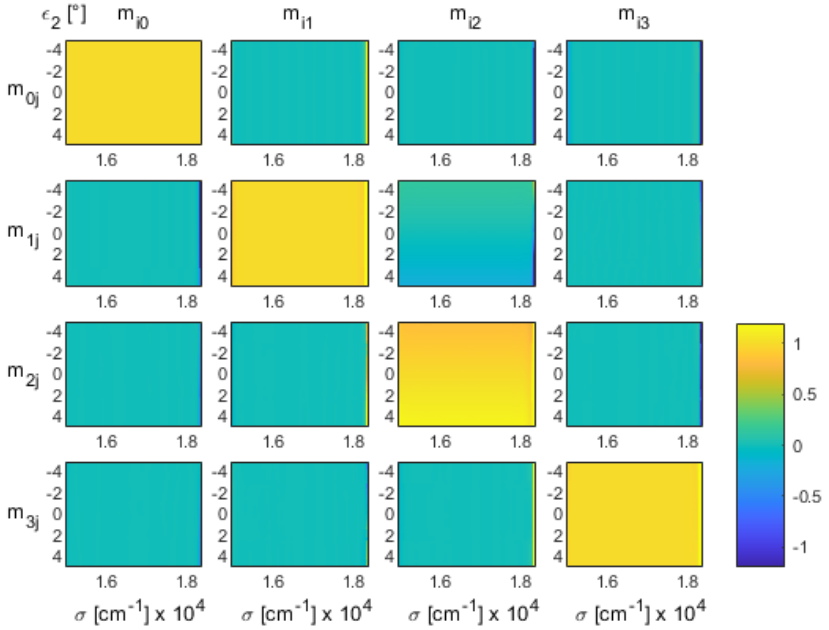

Figure 3.50: Normalized Mueller matrix elements (m_{ij}/m_{00}) of the sample (air) with a configuration $(1, 2, 5, 10)$ against the alignment error ϵ_2.

In Fig. 3.51 is shown the extracted Mueller matrix, considering the alignment error ϵ_3 from the third retarder. Most of the matrix elements are immune to ϵ_3. The elements m_{12}, m_{21} are sensitive to the error source, and $m_{01}, m_{03}, m_{11}, m_{22}$ are mostly immune.

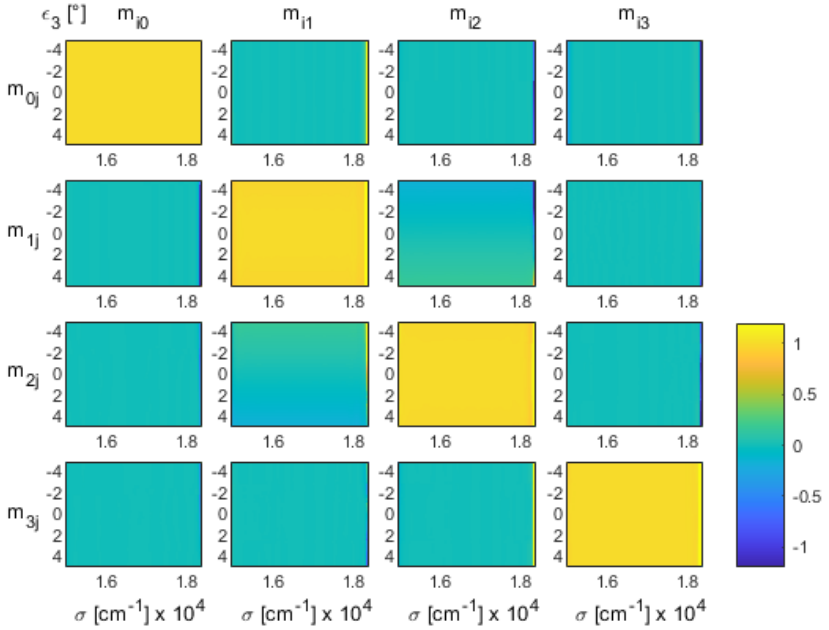

Figure 3.51: Normalized Mueller matrix elements (m_{ij}/m_{00}) of the sample (air) with a configuration $(1, 2, 5, 10)$ against the alignment error ϵ_3.

In Fig. 3.52 is shown the extracted Mueller matrix, considering the alignment error ϵ_4 from the fourth retarder. Most of the matrix elements are immune to ϵ_4. The elements m_{22}, m_{33} are sensitive to the error source, and m_{01}, m_{03}, m_{11} are mostly immune.

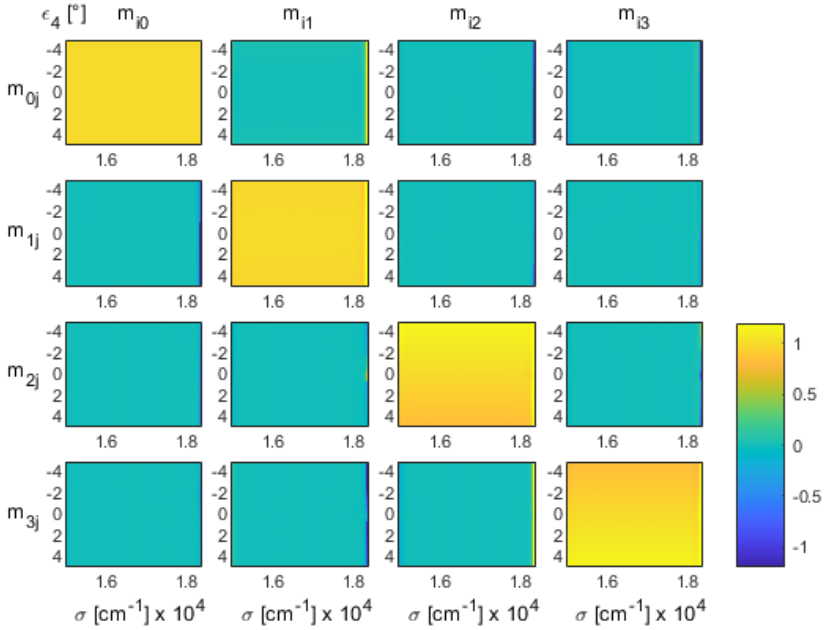

Figure 3.52: Normalized Mueller matrix elements (m_{ij}/m_{00}) of the sample (air) with a configuration $(1, 2, 5, 10)$ against the alignment error ϵ_4.

In Fig. 3.53 is shown the extracted Mueller matrix, considering the alignment error ϵ_5 from the second polarizer. Most of the matrix elements are immune to ϵ_5. The elements m_{22}, m_{33} are sensitive to the error source, and m_{01}, m_{03}, m_{11} are mostly immune.

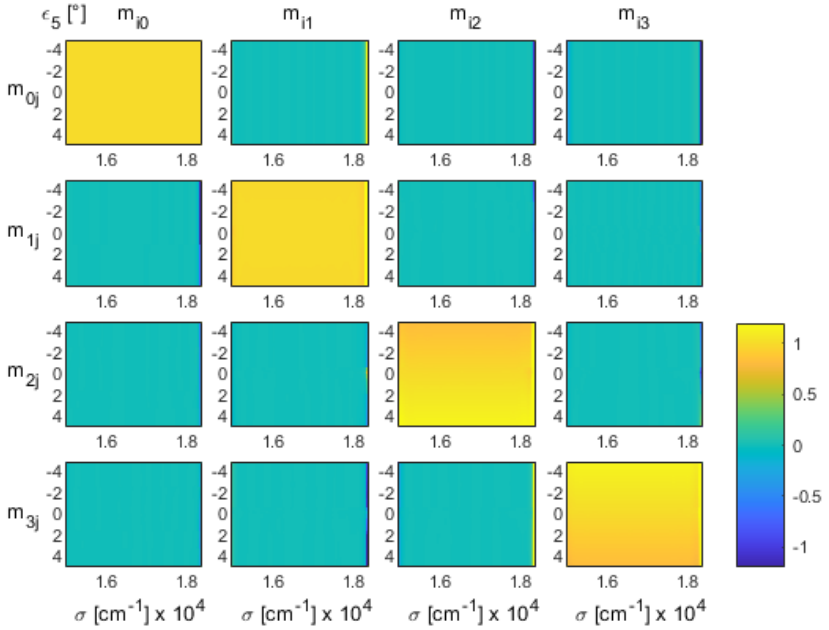

Figure 3.53: Normalized Mueller matrix elements (m_{ij}/m_{00}) of the sample (air) with a configuration $(1, 2, 5, 10)$ against the alignment error ϵ_5.

In Fig. 3.54 are shown the RMS plots for the extracted Mueller matrix, considering the alignment error of the four retarders and the second polarizer. The extraction is acceptable within the tolerance of ± 5 degrees. It is observed that the extraction process is more sensitive to the alignment error on the first retarder, for this retarder immunity is achieved between -0.3 and 0.4 degrees. The performance for the other three retarders and the second polarizer is similar between them, for these elements immunity is achieved within a tolerance of ± 0.6 degrees.

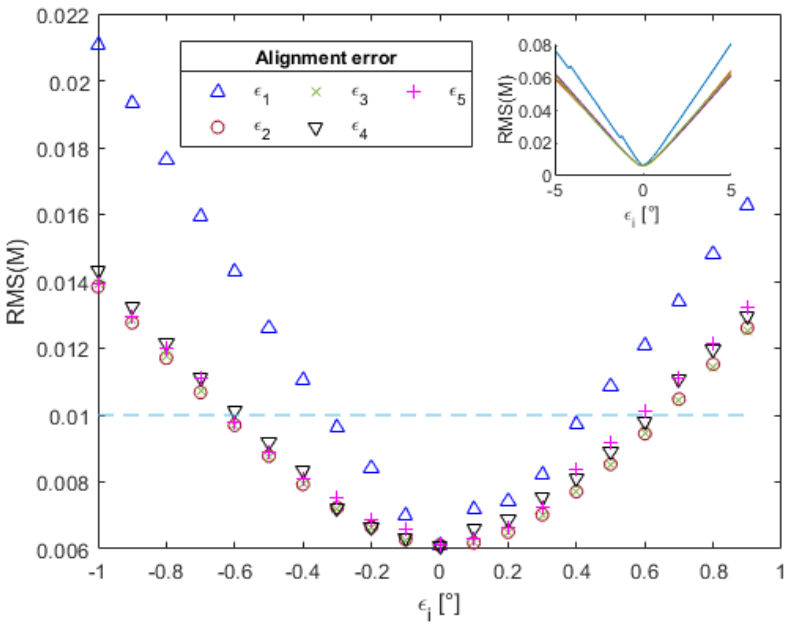

Figure 3.54: $RMS(M)$ against the alignment error ϵ_i for $i = 1, 2, ..., 5$ (first, second, third and fourth retarder, and second polarizer, respectively) within a tolerance of ± 1 degrees.

3.6.5 Gaussian noise

Similar to the SCS performance tests, a random noise distribution was added to the spectrum leaving the MMCS before entering the spectrometer. The amplitudes considered also range from $1E-6[a.u]$ to $1E1[a.u]$, including a reference without noise. In Fig. 3.55 is shown the extracted Mueller matrix, considering additive Gaussian noise. It is easily observed that the MMCS is immune to the noise distribution added, except for SNR higher than $100:1$, see the $RMS(m_{ij})$ plots in Fig. 3.56. In Fig. 3.57 is shown the autocorrelation function for all the Gaussian noise distribution amplitudes considered.

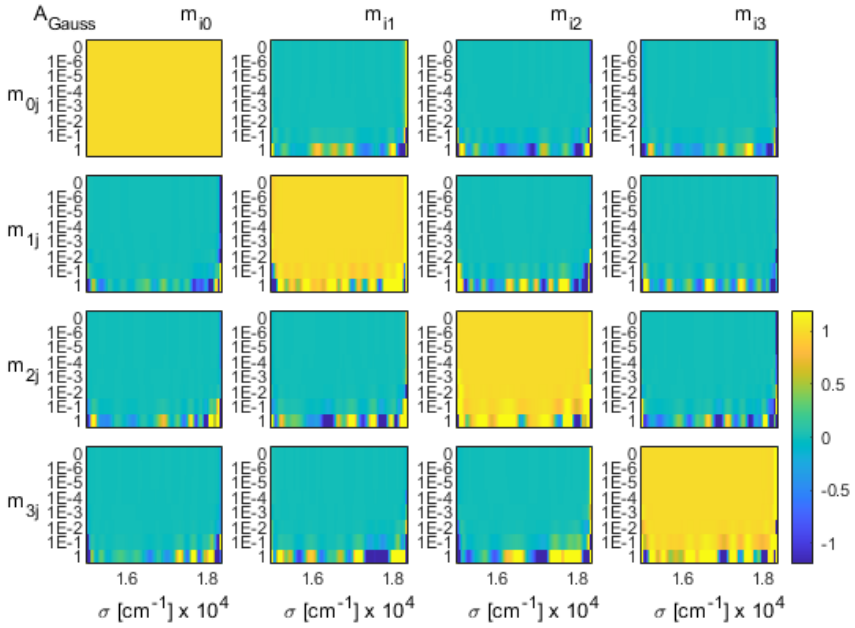

Figure 3.55: Normalized Mueller matrix elements (m_{ij}/m_{00}) of the sample (air) with a configuration $(1, 2, 5, 10)$ against the Gaussian noise distribution amplitude A_{Gauss}.

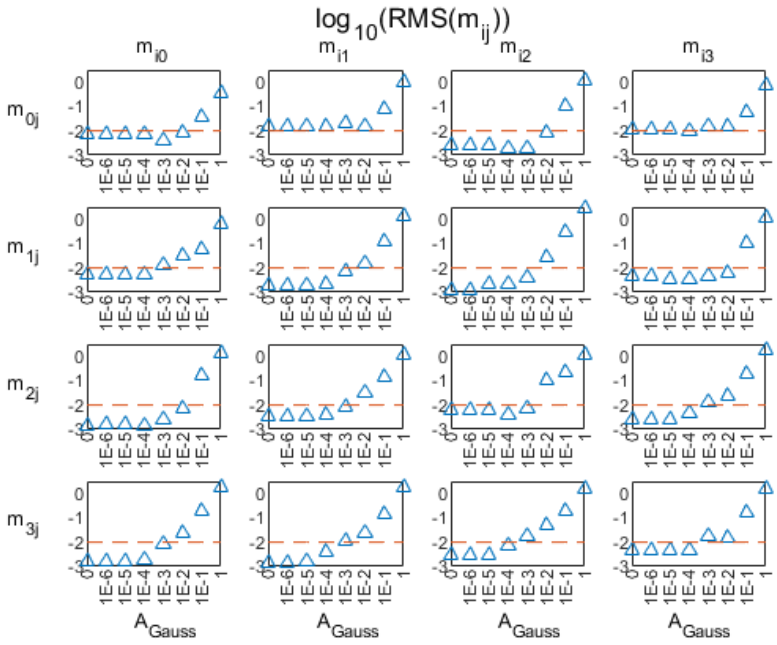

Figure 3.56: $log_{10}(RMS(m_{ij}))$ against the Gaussian noise distribution amplitude A_{Gauss}.

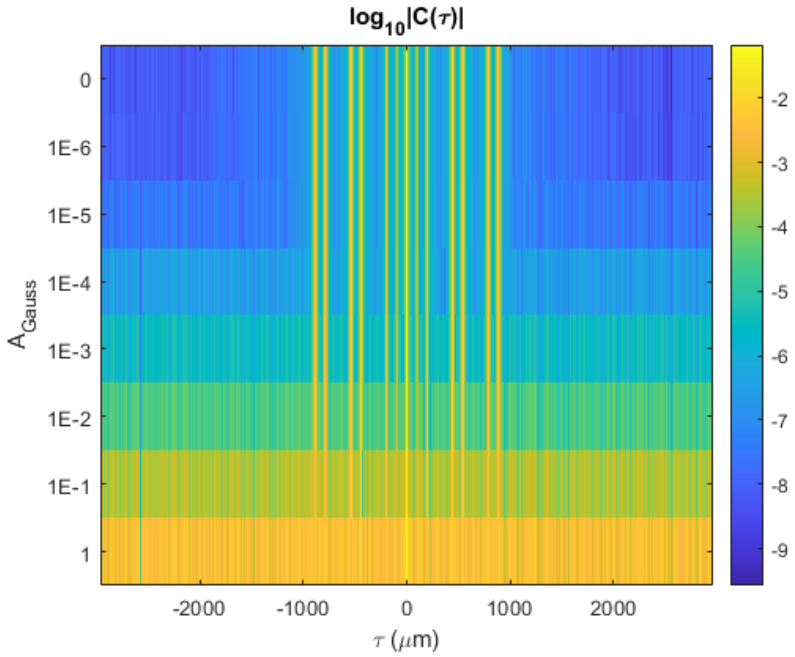

Figure 3.57: Autocorrelation function $|C(\tau)|$ of the MMCS against the Gaussian noise distribution amplitude A_{Gauss}.

Discussion and Conclusions

In this thesis, the results of analysis and simulations regarding passive and active channeled polarimeters, specifically with spectral channeling, were presented. Some extraction methods were also described, analysed and compared. Two figures of merit, the equally weighted variance (EWV) and the condition number (CN), were studied along their influence in the polarimeters performance and noise immunity. Although the main metric to evaluate the performance of the polarimeters was the root mean square error (RMS).

Stokes Channeled Spectropolarimeter

Overall, the parameter S_1 was extracted with better results than S_2 and S_3, with similar results for the two methods used, the Channel Splitting and the Analytical Channel Splitting methods. Although, to achieve an acceptable extraction, S_1 requires a tolerance of $\pm 1[^\circ]$ for the alignment error of the first retarder. The extraction of the parameters S_2 and S_3 is more sensitive to the error sources studied. Interestingly, they tend to present a mirrored behaviour when comparing the results of the channel splitting and the analytical channel splitting methods. For example, for some global retardance factors reviewed, when the channel splitting method had a better performance for S_2, the analytical channel splitting method worked better for S_3. For most of the rest of the factors, the opposite behaviour was observed.

Although, the configuration $(2, 1)$ had the highest EWV and CN values due to the overlapping of two pairs of channels, all six configurations studied allowed the extraction of the Stokes parameters within the immunity condition. Furthermore, the configuration $(2, 1)$ achieved the lowest RMS-values for the parameters S_2 and S_3. This is attributed to the information being packed in fewer channels, leading to a lower probability of crosstalk, and to the analytical development of the specific model of this

configuration. The best configurations to extract the parameters S_1, S_2, S_3 were $(1,3),(2,1),(2,1)$, respectively.

The global retardance factor has to be greater than $5[mm]$, it was observed that the performance of the SCS improved with this condition. This is at least considering the current algorithm implemented for the automatic channel detection and filtering process. Nevertheless, as this factor is directly related to the channel distribution, the number of pixels and the spectrometer spectral range have to be modified in accordance to optimize the distribution of channels in the autocorrelation function, in order to avoid crosstalk around the DC channel (C_0).

When error sources (retardance error, alignment error, and additive Gaussian noise) were introduced, some Stokes parameters showed immunity or acceptable extraction ranges (considering $RMS < 0.01$ or $RMS \approx 0.01$, respectively) for one or both of the methods considered (Channel Splitting and Analytical Channel Splitting). This presents an opportunity to develop a mixed extraction method using both methods to increase the overall immunity of the SCS to certain error sources.

Mueller matrix Channeled Spectropolarimeter

Six configurations were compared, three of them are known to have the minimum EWV scores [6], that is the highest immunity to additive noise. Although all six configurations have RMS scores within the immunity condition, it was observed that configurations $(1,4,2,9),(2,1,4,11),(2,1,5,12)$ offered the lowest RMS-scores, between $1E-4$ and $1E-5$ for most of the sample's Mueller matrix elements.

Similar to the SCS, it was concluded that the MMCS requires a global retardance factor greater than $5[mm]$. This is considering the algorithms implemented.

Overall, the extraction of the Mueller matrix elements was achieved within immunity or acceptable extraction, but further analysis is needed using samples with higher variance between all sixteen elements of the matrix.

Future work

A wider understanding of channeled polarimetry systems was achieved by way of the simulations of SCS and MMCS systems, the next step is the design and assembly of such a system in an experiment under real conditions. In order to confirm the influence of the parameters reviewed on the polarimeters performance.

A research proposal for future projects on the field could focus on the optimization metrics and noise immunity of different configurations with respect to configuration parameters of the polarimeter. Although, this topic has been addressed in the literature [6], a deeper understanding of the methodology is still needed. Other error sources, such as dichroism, should be further studied as well; temperature has already been addressed in the literature, as it is a crucial condition for the system's performance [15, 20, 36, 37].

Another necessary field to develop comprises the calibration methods for such spectral channeling systems, including a review of self-calibration approaches [20, 36] and their limitations.

Other fields that could benefit from the polarimeters reviewed are image polarimetry and snapshot polarimetry, in which parameters such as integration time must be determined, as the literature is not clear on the required range for this parameter.

Bibliography

[1] D. Goldstein, *Polarized Light*. New York: CRC Press, 3rd ed., 2011.

[2] A. S. Alenin and J. S. Tyo, "Task-specific snapshot Mueller matrix channeled spectropolarimeter optimization," in *Polarization: Measurement, Analysis, and Remote Sensing X*, vol. 8364, pp. 836402–836402–13, jun 2012.

[3] R. M. A. Azzam, "Photopolarimetric measurement of the Mueller matrix by Fourier analysis of a single detected signal," *Optics Letters*, vol. 2, no. 6, p. 148, 1978.

[4] D. B. Chenault, J. L. Pezzaniti, and R. A. Chipman, "Mueller matrix algorithms," in *Polarization Analysis and Measurement*, vol. 1746, pp. 231–246, 1992.

[5] D. B. Chenault, "Spectropolarimetric reflectometer," *Optical Engineering*, vol. 41, no. 5, p. 1013, 2002.

[6] A. S. Alenin and J. S. Tyo, "Generalized channeled polarimetry," *Journal of the Optical Society of America A*, vol. 31, no. 5, p. 1013, 2014.

[7] D. E. Aspnes, "Analysis Of Semiconductor Materials And Structures By Spectroellipsometry," *Spectroscopic Characterization Techniques for Semiconductor Technology III*, vol. 0946, no. August 1988, p. 84, 1988.

[8] K. Oka and T. Kato, "Spectroscopic polarimetry with a channeled spectrum," *Optics Letters*, vol. 24, no. 21, p. 1475, 1999.

[9] D. J. Diner, R. A. Chipman, N. A. Beaudry, B. Cairns, L. D. Foo, S. A. Macenka, T. J. Cunningham, S. Seshadri, and C. U. Keller, "An integrated multiangle, multispectral, and polarimetric imaging concept

for aerosol remote sensing from space," in *Enabling Sensor and Platform Technologies for Spaceborne Remote Sensing* (G. J. Komar, J. Wang, and T. Kimura, eds.), vol. 5659, p. 88, jan 2005.

[10] S. H. Jones, F. J. Iannarilli, C. Hostetler, B. Cairns, A. Cook, J. Hair, D. Harper, Y. Hu, and D. Flittner, "Preliminary airborne measurement results from the Hyperspectral Polarimeter for Aerosol Retrievals (HySPAR).," *NASA Earth Science Technology Conference Proceedings*, no. June, pp. 1–6, 2006.

[11] N. Gupta and D. R. Suhre, "Acousto-optic tunable filter imaging spectrometer with full Stokes polarimetric capability," *Appl. Opt.*, vol. 46, pp. 2632–2637, may 2007.

[12] N. Gupta, "Acousto-optic tunable filter based spectropolarimetric imagers," in *Polarization: Measurement, Analysis, and Remote Sensing VIII* (D. B. Chenault and D. H. Goldstein, eds.), vol. 6972, pp. 88–98, International Society for Optics and Photonics, SPIE, 2008.

[13] B. P. Cumming, G. E. Schröder-Turk, S. Debbarma, and M. Gu, "Bragg-mirror-like circular dichroism in bio-inspired quadruple-gyroid 4srs nanostructures," *Light: Science and Applications*, vol. 6, no. 1, pp. 1–8, 2017.

[14] A. Y. Zhu, W. T. Chen, A. Zaidi, Y. W. Huang, M. Khorasaninejad, V. Sanjeev, C. W. Qiu, and F. Capasso, "Giant intrinsic chiro-optical activity in planar dielectric nanostructures," *Light: Science and Applications*, vol. 7, no. 2, p. 17158, 2018.

[15] X. Ju, B. Yang, C. Yan, J. Zhang, and W. Xing, "Easily implemented approach for the calibration of alignment and retardation errors in a channeled spectropolarimeter," *Applied Optics*, vol. 57, p. 8600, oct 2018.

[16] E. Hecht, *Optics*. San Francisco: Addison Wesley, 4th ed., 2002.

[17] J. S. Tyo, D. L. Goldstein, D. B. Chenault, and J. A. Shaw, "Review of passive imaging polarimetry for remote sensing applications," *Appl. Opt.*, vol. 45, no. 22, pp. 5453–5469, 2006.

[18] M. H. Smith, J. B. Woodruff, and J. D. Howe, "Beam wander considerations in imaging polarimetry," in *Polarization: Measurement, Analysis, and Remote Sensing II* (D. H. Goldstein and D. B. Chenault, eds.), vol. 3754, pp. 50–54, International Society for Optics and Photonics, SPIE, 1999.

[19] D. S. Sabatke, A. M. Locke, E. L. Dereniak, and R. W. McMillan, "Linear operator theory of channeled spectropolarimetry," *J. Opt. Soc. Am. A*, vol. 22, no. 8, pp. 1567–1576, 2005.

[20] N. Hagen, "Calibration methods for snapshot Mueller matrix spectropolarimetry," in *Optical Technology and Measurement for Industrial Applications 2020* (T. Hatsuzawa, R. Tutsch, and T. Yoshizawa, eds.), vol. 1152302, (Yokohama), p. 10, SPIE, jun 2020.

[21] R. A. Chipman, "Polarimetric impulse response and polarimetric transfer function for time-sequential polarimeters," in *Polarimetry: Radar, Infrared, Visible, Ultraviolet, and X-Ray*, vol. 1317, pp. 223–241, 1990.

[22] N. Hagen, K. Oka, and E. L. Dereniak, "Snapshot Mueller matrix spectropolarimeter," *Optics Letters*, vol. 32, p. 2100, may 2007.

[23] G. Ghosh, "Dispersion-equation coefficients for the refractive index and birefringence of calcite and quartz crystals," *Optics Communications*, vol. 163, no. 1, pp. 95–102, 1999.

[24] D. S. Sabatke, A. M. Locke, E. L. Dereniak, and R. W. McMillan, "Linear calibration and reconstruction techniques for channeled spectropolarimetry," *Optics Express*, vol. 11, p. 2940, nov 2003.

[25] M. Takeda, H. Ina, and S. Kobayashi, "Fourier-Transform Method of Fringe-Pattern Analysis for Computer-Based Topography and Inteferometry.," *Journal of the Optical Society of America*, vol. 72, no. 1, pp. 156–160, 1982.

[26] F. J. Harris, "On the Use of Windows for Harmonic Analysis with the Discrete Fourier Transform," *Proceedings of the IEEE*, vol. 66, no. 1, pp. 51–83, 1978.

[27] D. J. Lee, C. F. LaCasse, and J. M. Craven, "Compressed channeled spectropolarimetry," *Optics Express*, vol. 25, no. 25, pp. 32041–32063, 2017.

[28] S. S. Ballard, S. E. Brown, and J. S. Browder, "Measurements of the thermal expansion of six optical materials, from room temperature to 250 degrees C," *Applied Optics*, vol. 17, no. 7, p. 1152, 1978.

[29] M. W. Kudenov, L. Pezzaniti, E. L. Dereniak, and G. R. Gerhart, "Prismatic imaging polarimeter calibration for the infrared spectral region," *Optics Express*, vol. 16, no. 18, p. 13720, 2008.

[30] M. W. Kudenov, N. Hagen, E. L. Dereniak, and G. R. Gerhart, "Fourier transform channeled spectropolarimetry in the MWIR," *Optics Express*, vol. 15, no. 20, p. 12792, 2007.

[31] T. Mu, Z. Chen, C. Zhang, and R. Liang, "Optimal configurations of full-Stokes polarimeter with immunity to both Poisson and Gaussian noise," *Journal of Optics (United Kingdom)*, vol. 18, no. 5, pp. 29691–29704, 2016.

[32] G. Anna and F. Goudail, "Optimal Mueller matrix estimation in the presence of Poisson shot noise," *Optics Express*, vol. 20, no. 19, p. 21331, 2012.

[33] Y. Takakura and J. E. Ahmad, "Noise distribution of Mueller matrices retrieved with active rotating polarimeters," *Applied Optics*, vol. 46, no. 30, pp. 7354–7364, 2007.

[34] D. S. Sabatke, M. R. Descour, E. L. Dereniak, W. C. Sweatt, S. A. Kemme, and G. S. Phipps, "Optimization of retardance for a complete Stokes polarimeter," *Optics Letters*, vol. 25, no. 11, p. 802, 2000.

[35] Thorlabs Inc., "Product Raw Data. Stabilized Tungsten Halogen IR Light Source SLS202L."

[36] A. Taniguchi, K. Oka, H. Okabe, and M. Hayakawa, "Stabilization of a channeled spectropolarimeter by self-calibration," *Optics Letters*, vol. 31, no. 22, p. 3279, 2006.

[37] H. Okabe, M. Hayakawa, H. Naito, A. Taniguchi, and K. Oka, "Spectroscopic polarimetry using channeled spectroscopic polarization state generator (CSPSG)," *Optics Express*, vol. 15, no. 6, p. 3093, 2007.